UNIVERSITÀ DEGLI STUDI DI MILANO

PhD degree in Systems Medicine

Dept. Of Oncology and Emato-Oncology

Targeting Type-I PRMTs Restores Platinum Sensitivity in Ovarian Carcinoma through Mitochondrial Metabolism

MEDS-02/A

Student name: Ayusi Mondal

Matriculation number: R13512

ORCID no: 0000-0002-8242-6616

Tutor name and surname: Prof. Tiziana Bonaldi

A.A. 2024-2025

Table of contents

List of abbreviations

2-HG - 2-Hydroxyglutarate
53BP1 - Tumor Protein P53 Binding Protein 1
6PGD - 6-Phospho-Gluconate Dehydrogenase
A - Alanine
ADMA - Asymmetrically Dimethylated Arginine
Akt - Akt Serine/Threonine Kinase
BAD - Bcl2 Associated Agonist Of Cell Death
BAF155 - Swi/Snf Related Baf Chromatin Remodeling Complex Subunit C1
BNIP3 - Bcl2 Interacting Protein 3
CARM1 - Coactivator Associated Arginine Methyltransferase 1
CBP - Carboplatin
CBS - Cystathionine B-Synthase
CCCP - Carbonyl Cyanide M-Chlorophenyl Hydrazone
CCOC - Clear-Cell OC
CDDP - Cisplatin
CDK - Cyclin Dependent Kinase
CDKN - Cyclin Dependent Kinase Inhibitor
CE–MS - Capillary Electrophoresis Mass Spectrometry
COL1A2 - Collagen Type I Alpha 2 Chain
DDA - Data Dependent Acquisition
DDX - Dead-Box Helicase
DIA - Data Independent Acquisition
DNA - Deoxy Ribonucleic Acid
DNA-PK - Dna-Dependent Protein Kinase
DRP1 - Dynamin-Related Protein 1
ECAR - Extracellular Acidification Rate
EMOC - Endometrioid OC
EMT - Epithelial-To-Mesenchymal Transition
ENO1 - Enolase 1
EOC - Epithelial Ovarian Carcinoma
ETC - Electron Transport Chain
EZH2 - Enhancer Of Zeste 2 Polycomb Repressive Complex 2 Subunit
F-2,6-BP - Fructose 2,6-Bisphosphate
FCCP - Carbonyl Cyanide-P-Trifluoromethoxyphenyl Hydrazone
FDR - False Discovery Rate
G6PD - Glucose-6-Phosphate Dehydrogenase
GAPDH - Glyceraldehyde-3-Phosphate Dehydrogenase
GC - Gas Chromatography
GCLM - Glutamate-Cysteine Ligase Modifier Subunit
GNPS - Global Natural Products Social Molecular Networking
GPX - Glutathione Peroxidase
HGSOC - High-Grade Serous OC

HIF1 - Hypoxia Inducible Factor
HMDB - The Human Metabolome Database
JMJD - Jumonji Domain-Containing Protein
K - Lysine
KEAP1 - Kelch Like Ech Associated Protein 1
KRAS - Kirsten Rat Sarcoma Virus
LC - Liquid Chromatography
LDHA - Lactate Dehydrogenase A
LGSOC - Low-Grade Serous OC
MANOVA - Multivariate Variance Analysis Test
MAPK - Mitogen-Activated Protein Kinase
MCOC - Mucinous OC
MDH - Malate Dehydrogenase
METLIN - Metabolite And Chemical Entity Database
MFN1 - Mitofusin
miR - Micro RNA
MMA - Monomethylated Arginine
MPP7 - Maguk P55 Scaffold Protein 7
MRM - Multiple Reaction Monitoring
mRNA - Messenger RNA
MS - Mass Spectrometry
mtDNA - Mitochondrial DNA
NAD - Nicotinamide Adenine Dinucleotide
NADP - Nicotinamide Adenine Dinucleotide Phosphate
NCLX - Na^+/Ca^{2+} Exchanger
NDUF - Nadh:Ubiquinone Oxidoreductase
NF1 - Neurofibromin 1
NSCLC - Non-Small Cell Lung Carcinoma
OC - Ovarian Cancer
OCR - Oxygen Cinsumption Rate
OGT - O-Glcnac Transferase
OPA1 - Optic Atrophy Protein 1
PAD4 - Peptidyl-Arginine Deiminase 4
PARP - Poly(Adp-Ribose) Polymerase
PCA - Principle Component Analysis
PDK2 - Pyruvate Dehydrogenase Kinase 2
PFK-1 - Phosphofructokinase-1
PI3K - Phosphatidylinositol-4,5-Bisphosphate 3-Kinase
PIK3CA - Alpha
PINK1 - Phosphatase And Tensin Homolog-Induced Putative Kinase 1
PKM2 - Pyruvate Kinase M2
PLS-DA - Partial Least Squares Discriminant Analysis
PPP - Pentose Phosphate Pathway
PRMT - Protein R-Methyl Transferase
PTEN - Phosphatase And Tensin Homolog

PTM - Post Translational Modification
Q-TOF - Quadrupole-Time-Of-Flight
R - Arginine
RB1 - Retinoblastoma 1/ Rb Transcriptional Corepressor 1
RHOT1 - Ras Homolog Family Member T1
RNA - Ribonucleic Acid
ROS - Reactive Oxygen Species
RPIA - Ribose-5-Phosphate Isomerase A
RP-nLC - Reversed-Phase Nano-Liquid Chromatography
SAH - S-Adenosyl Homocysteine
SAM - S-Adenosyl Methionine
SASP - Senescence-Associated Secretory Phenotype
SDMA - Symmetrically Dimethylated Arginine
SIRT - Sirtuin
SOD2 - Superoxide Dismutase 2
STAT3 - Signal Transducer And Activator Of Transcription 3
TCA - Tricarboxylic Acid Cycle
TFAM - Transcription Factor A, Mitochondrial
TFB2M - Transcription Factor B, Mitochondrial
TIGIT - T-Cell Immunoreceptor With Ig And ITIM Domains

Figure Index

Table Index

1. Abstract

Adaptive chemoresistance remains a critical barrier to effective ovarian cancer therapy, necessitating a deeper understanding of the cellular and metabolic changes that drive platinum resistance. Here, we dissect the interplay between platinum-induced genotoxic stress, type-I protein arginine methyltransferases–mediated post-translational modifications, and mitochondrial metabolic plasticity underpinning chemoresistance in EOC. We present an integrative multi-omics analysis of carboplatin-resistant A2780 ovarian cancer cells (A2780R) developed via stepwise drug adaptation, revealing pronounced mitochondrial and metabolic rewiring. A2780R cells display an 8.8-fold increase in carboplatin IC50 compared to parental A2780S cells and elevated mitochondrial respiratory capacity, and a hyperfused mitochondrial network, as quantified by 3D-skeleton imaging. Notably, pharmacological inhibition of Type-I protein arginine methyltransferases (PRMTs) with MS023 re-sensitizes A2780R cells to carboplatin, reducing IC50 by up to 56%, and abrogates the enhanced mitochondrial activity. MS023 treatment induces depolarization of the mitochondrial membrane, diminishes mitochondrial volume and network integrity, and triggers mitophagy.

Proteomic and metabolomic analyses at steady state and upon PRMT inhibition revealed that A2780R cells adapt by favouring anabolic pathways, with notable upregulation of nucleotide and glutathione metabolism and increased amino acid catabolism. This metabolic rewiring is associated with elevated NADPH production from the pentose phosphate pathway, supporting enhanced glutathione-mediated redox buffering. MS023 disrupts these adaptations, depleting glutathione pools and precursor amino acids, reducing redox balance, and shifting central carbon metabolism. Isotope tracing confirms that A2780R cells channel serine-derived carbons into glutathione synthesis, a process blunted by Type-I PRMT inhibition.

Mechanistic investigations indicate that R-methylation of mitochondrial proteins modulates biogenesis, metabolic flexibility, and oxidative stress buffering, establishing Type-I PRMTs as essential regulators of chemoresistance-associated metabolic shifts. Our findings position Type-I PRMT inhibition as a promising combinatorial approach to overcome platinum resistance by targeting maladaptive metabolic features in ovarian cancer cells. This study provides a comprehensive blueprint of the mitochondrial and metabolic phenotypes underpinning adaptive chemoresistance, highlighting the translational potential of metabolic vulnerabilities in the therapeutic sensitisation of resistant cancer phenotypes.

2. Introduction

2.1 Ovarian Cancer: General understanding through the lens of 'OMICS'

Ovarian cancer (OC) is a group of diseases that includes at least five distinct histological subtypes, each with different progenitors, genetic and epigenetic signatures that require separate treatment approaches and have varying prognoses (Matulonis *et al.*, 2016). These subtypes can also display extensive molecular, cellular, and anatomical heterogeneity both spatially (across spaces within the tumour mass) and temporally (over time) (Veneziani *et al.*, 2023). The five histological subtypes—high-grade serous OC (HGSOC), low-grade serous OC (LGSOC), clear-cell OC (CCOC), endometrioid OC (EMOC), and mucinous OC (MCOC) (Matulonis *et al.*, 2016)—can originate from epithelial, sex cord-stromal, and germ cell origins (Karnezis *et al.*, 2016). Interestingly, the most common types originate from cells not structurally present in the ovary itself, but primarily from epithelial cells of the fallopian tube, endometrium, as well as granulosa cells and somatic cells of teratomas that occur outside the ovary (Karnezis *et al.*, 2016). Notably, epithelial ovarian carcinoma (EOC) accounts for about 95% of all OC cases across histological subtypes (Arora *et al.*, 2024).

EOCs can be further classified into two types based on their molecular signature. Type-I tumours (e.g., LGSOC, EMOC, CCOC) are less aggressive, can be detected at earlier stages and show a combination of different mutations such as KRAS, BRAF, PTEN, PIK3CA, etc. (**Figure 1**). On the other hand, type II tumours (e.g., HGSOC), which mainly originate from fallopian tube epithelium, are more aggressive, seldom detected early and primarily characterised by mutated TP53 (Rojas *et al.*, 2016). Epigenetic signatures such as DNA methylation status, nucleosome positioning, post-translational modification of histones, chromatin accessibility, and post-transcriptional regulation by microRNAs (miRNAs) are also known to regulate stages, aggressiveness and command prognosis in EOC. For instance, DNA hypomethylation in usually silenced oncogenes is a characteristic feature of all EOC histotypes and correlates directly with increasing stage, grade and mortality (Natanzon, Goode and Cunningham, 2017). Another active area of research in cancer epigenetics is histone modifications, the key proteins that regulate nucleosome packaging and thereby accessibility of DNA during gene transcription. Methylation and acetylation are such well-known modifications on different histone proteins (H1, H3, H4, H2A and H2B) that are orchestrated by methyltransferases/demethylases and acetyltransferase/deacetylases, respectively (Marsh, Shah and Cole, 2014).

The advancements and growing accessibility of various '-omics'-based studies have helped to reshape the complex molecular landscape of this disease, which was once regarded as a single

condition and treated uniformly (Subbannayya *et al.*, 2021). '-Omics' is a suffix that refers to any comprehensive analysis and measurement of biological molecules, such as DNA, RNA, proteins, metabolites, etc., from large-scale datasets to understand their roles in distribution, function, and dynamics within living organisms. Consequently, the suffix 'ome' refers to the objects of the study, such as the genome, transcriptome, proteome, and metabolome. Another benefit of omics-based studies is that different layers of results can be integrated, as well as with clinical data. These combined data can be visualised or understood comprehensively without losing detail or resolution. They can also be used to train algorithms or models that speed up precision medicine by predicting new biomarkers or therapeutic targets, quantifying complex molecular interactions, and revealing novel regulatory nodes or networks.

For example, in 2011, a comprehensive atlas of molecular aberrations was created by assessing and integrating mRNA and miRNA expression, promoter methylation, and DNA copy number data from a cohort of 489 OC patients. This integration highlighted nine other recurring somatic mutations in OC patients, such as NF1, BRCA1, BRCA2, RB1, and CDK12, which are significant but less common compared to the most prominent TP53 mutation (found in 96%, **Figure 1**) (Bell *et al.*, 2011).

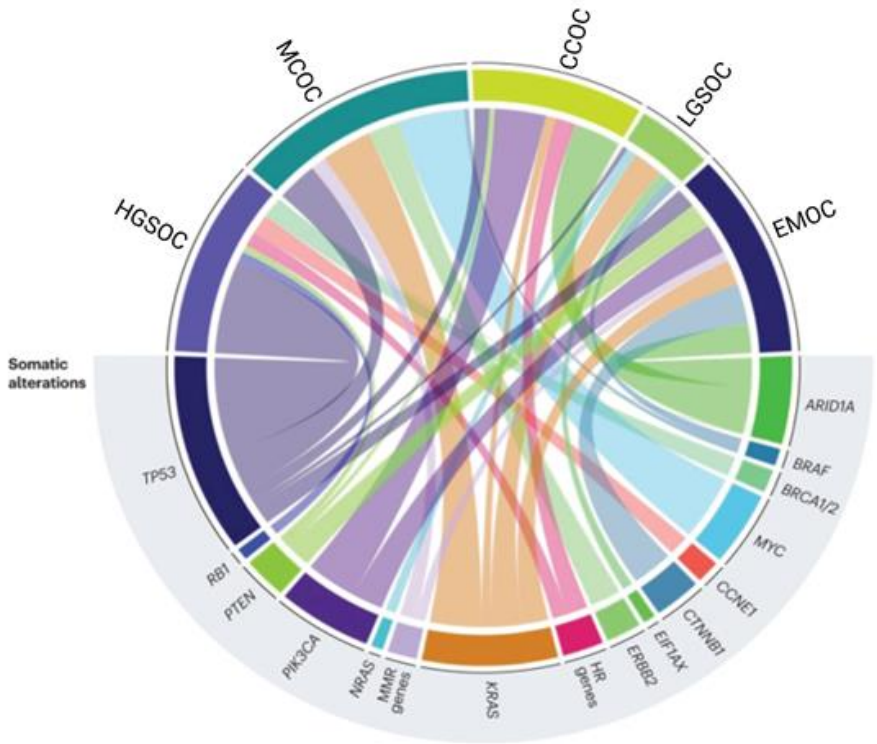

Figure 1: Association between somatic mutation and histological subtypes of OC
Circos plot showing the associations between the most prominent somatic mutations found in the five histological subtypes of ovarian carcinoma. For example, HGSOC is mainly characterised by mutated TP53, while LGSOC is primarily characterised by KRAS mutation. The figure is adapted from (Veneziani *et al.*, 2023)

Single-cell RNA sequencing of malignant ascites (abdominal fluid) in OC revealed considerable inter-patient and intra-tumour variability, describing the differential roles of various immunomodulatory fibroblasts and macrophages subpopulations. This heterogeneity was associated with copy number and/or stemness programme alterations (Izar *et al.*, 2020). Similar analysis of tumour tissues from HGSOC patients pinpointed genes involved in the activated epithelial-to-mesenchymal transition (EMT) programme. It proposed TIGIT (T-cell immunoreceptor with Ig and ITIM domains) as a new therapeutic target for tackling OC (Xu *et al.*, 2022).

Proteomic analysis across various patient cohorts has further reinforced the concept of heterogeneity and the potential for more targeted therapies. Analysis of a large cohort of 1041 ovarian tissue samples from 813 EOC patients revealed distinct differences in proteomic features among five different histological subtypes. For example, HGSOC, which accounts for 70% of all deaths due to OC, showed an apparent variation in inositol compound metabolism between primary and relapsing patients (Qian *et al.*, 2024). Early integrative studies from the Clinical Proteomic Tumour Analysis Consortium (CPTAC) demonstrated that proteomic profiling refines ovarian cancer subtypes and captures tumour microenvironment features, including extracellular matrix remodelling and signalling alterations, often missed at the transcriptomic level (Zhang *et al.*, 2016). Researchers have performed deep proteomic analysis on 239 tumours across CCOC, EMOC, and serous ovarian carcinoma (SOC). Over 8,000 proteins were quantified, highlighting firm inter-tumour heterogeneity. SC, associated with poor prognosis, exhibited enrichment of DNA replication, HIF-1 signalling, and oxidative phosphorylation pathways. Network analysis revealed prognostic biomarkers and therapeutic targets such as CDK4, CDKN1B, and COL1A2, while functional validation identified MPP7 as a potential vulnerability in SC (Gong *et al.*, 2023). More recently, combined bulk proteomics of 154 tumours with single-cell transcriptomics data to classify four robust proteomic subtypes: malignant proliferative (C1), immune infiltrating (C2), Fallopian-like (C3), and differentiated (C4). The C2 subtype showed active CD8+ T cell and macrophage infiltration, with CD40 emerging as a prognostic biomarker and therapeutic target. In contrast, non-immune subtypes displayed proliferative or metabolic programs, where Thymidine Phosphorylase inhibition demonstrated preclinical efficacy (Tan *et al.*, 2024).

In CCOC (clear-cell OC), the characteristic glycogen accumulation suggests involvement of altered metabolic activity. The first comprehensive metabolomic landscape on three major histological subtypes of OC was published in 2024. This study, comprised of 42 CCOC, 20 HGSOC and 21 EMOC patient tissues, highlighted that different subtypes prefer different substrates for energy production and showed perturbations in cysteine metabolism. For example,

CCOC samples were metabolically very distinct from the other two subtypes analysed and relied more on serine biosynthesis for antioxidant production (J. X. Ji *et al.*, 2024).

Even though in the last decade we have gained a much deeper understanding of this disease by leveraging cutting-edge technologies, but still, OC remains the most lethal gynaecological malignancy worldwide (Fiscutean, 2021; Webb and Jordan, 2024). The symptoms of OC are not exclusive to the disease; therefore, it often leads to a late diagnosis (at stage III or IV). In the advanced stage, the treatment involves cytoreductive surgery, which is followed by platinum-based or taxane-based chemotherapy depending on the remaining tumour load (Matulonis *et al.*, 2016). Broadly, the patients respond well to this therapeutic approach, but very often, they develop drug resistance, followed by a major relapse and the molecular mechanism underlying this treatment failure remains poorly understood. Currently, the primary battle against OC is narrowed down to two key aspects: late detection and chemoresistance. This study attempts to unravel a novel mechanism of chemoresistance in EOC from an "omics" perspective – the details of which will be described in the following sections.

2.2 Mass spectrometry (MS) and MS-based proteomics and metabolomics

In this project, we have used mass spectrometry (MS)-based proteomics and metabolomics, among other cell and molecular biology techniques, to understand the molecular mechanism underlying the onset of chemoresistance in OC. MS is a powerful analytical technique used to precisely measure the mass-to-charge ratio (m/z) of molecules. With significant advances in resolution, sensitivity, and instrument performance, MS has become the leading method for analysing complex biological samples unbiasedly.

Here, within proteomic approaches, we have applied global proteomics to analyse protein expression on a cellular level (**see results 5.3**) as well as modification proteomics to understand protein post-translational modifications (PTMs) (**see introduction 2.4 and results 5.6**). In the widely adopted bottom-up approach, proteins are enzymatically digested into small peptides, typically under 30 amino acids, before MS analysis. Peptides are preferred over intact proteins because they are more easily separated, ionised, and fragmented. When this strategy is applied to a mixture of proteins, it is commonly referred to as shotgun proteomics (Yates, 1998) (**Figure 2**). A typical shotgun proteomics workflow begins with extracting proteins from a biological sample, followed by enzymatic digestion using proteases—most often trypsin. Trypsin cleaves proteins at specific amino acid residues, producing peptides around 10–12 amino acids long, which are ideal for MS detection. After digestion, peptides are purified and concentrated using reversed-phase

C18 resin. To reduce sample complexity, peptides are separated by online reversed-phase nano-liquid chromatography (RP-nLC), which is directly connected to the mass spectrometer. RP-nLC separates peptides based on hydrophobicity, while the mobile phase ensures effective ion transfer into the MS (Duong and Lee, 2023; Shuken, 2023). To overcome the sub-stoichiometric (fractional stoichiometric) nature of PTMs for its annotation and quantification, usually an enrichment step (chemical or antibody-based) is added after protein digestion and purification (**see results 5.6**) (Fong *et al.*, 2019; Musiani *et al.*, 2019; Maniaci *et al.*, 2022).

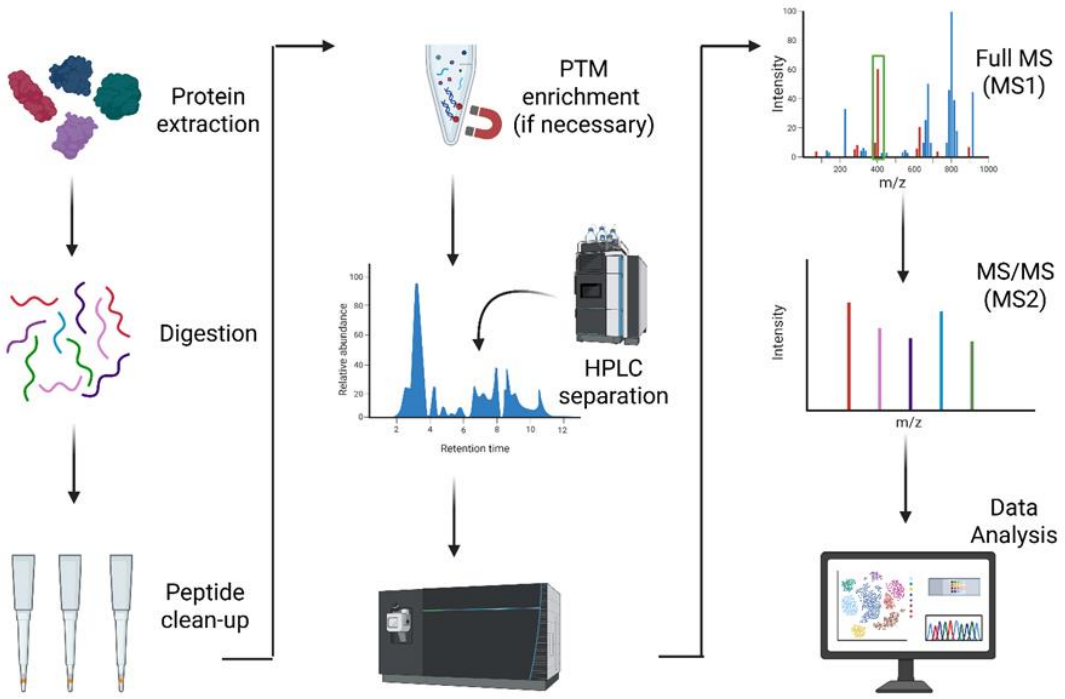

Figure 2: Shotgun proteomics workflow
A standard bottom-up (shotgun) proteomics workflow comprising protein extraction, digestion, peptide clean-up, optional enrichment step for PTM annotation, HPLC separation, MS acquisition and data analysis. Figure made with Biorender.com

Inside the mass spectrometer, precursor peptides are first analysed in a full scan (MS1) to determine their m/z ratios and elemental composition. Selected precursors are then fragmented into smaller ions during tandem MS (MS2), generating spectra that reflect their sequence. These spectra are compared to theoretical spectra derived from computational digestion of protein databases to identify peptide sequences, which are then mapped back to the corresponding proteins. The acquisition is typically done in either data-dependent (DDA) or data-independent (DIA) mode. In DDA, the mass spectrometer first performs MS1 for quantification, then selectively isolates and fragments a limited number of the most abundant precursor ions for MS2 sequencing, resulting in a peptide-specific MS2 spectrum for identification. By prioritising the most

intense ions, DDA mode collects fewer but cleaner MS2 spectra, which is ideal for spectral library generation and novel PTM identification. In contrast, DIA systematically fragments all ions within sequential and overlapping m/z windows across a predefined mass range that is independent of ion abundance. This approach simultaneously generates composite MS2 spectra containing fragment ions from multiple co-isolated precursors (**Figure 3**).

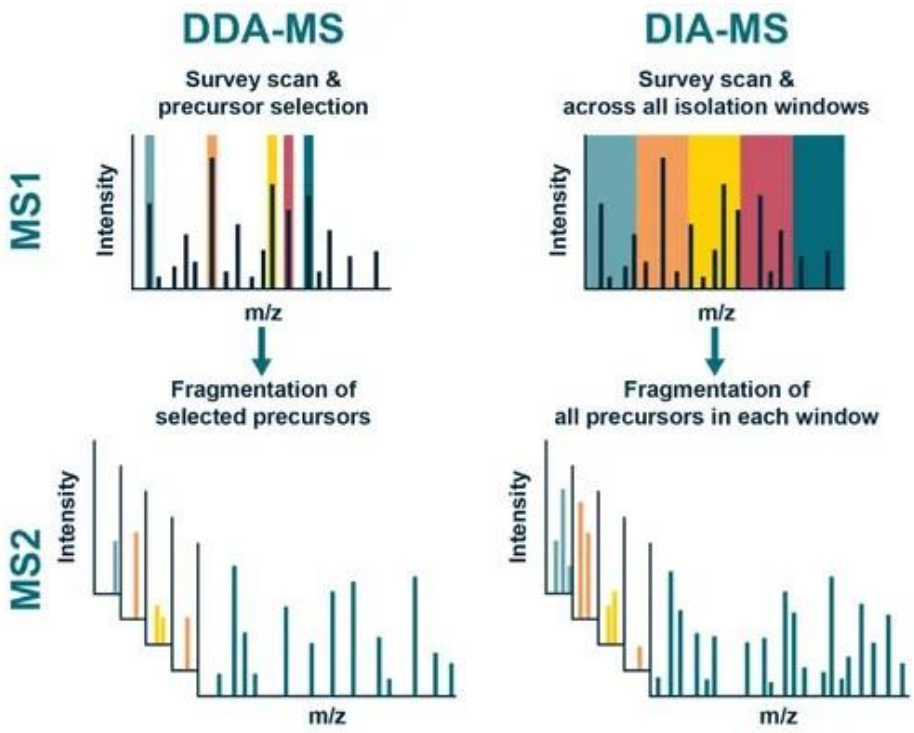

Figure 3: Principal differences between DDA and DIA
In DDA-MS (left), an initial MS1 survey scan is performed, and a subset of precursor ions with the highest intensities is selected for fragmentation. Only these chosen precursors are subjected to MS2, leading to incomplete but targeted coverage. In DIA-MS (right), the MS1 scan is followed by systematic fragmentation of all precursors within predefined m/z isolation windows, ensuring more comprehensive and unbiased sampling. The resulting MS2 spectra contain fragment ions from all precursors in each window, increasing the depth and reproducibility of proteome coverage. Figure adapted from www.crownbio.com.

Theoretically, DIA mode allows comprehensive coverage by acquiring fragmented data on all detectable peptides. Software, such as DIA-NN 2.0, performs deconvolution of the complex MS2 spectra and relies on a spectral library (usually generated from multiple DDA acquisition or in-silico) for both identification and quantification. Thus, DIA is preferred over DDA mode for the total proteome, while DDA is still a method of choice for PTM annotation. On one hand, the stochastic nature of ion selection in DDA can lead to missing data in complex samples, while on the other hand, DIA can miss the discovery of novel PTMs if the corresponding spectral library is incomplete.

To reduce false positives, a False Discovery Rate (FDR) is estimated using a method that compares matches against actual and artificially reversed protein sequences. Once established, the FDR is used to eliminate incorrect identifications. Various software tools and algorithms are employed to interpret MS data and identify peptides and proteins. These include widely used engines capable of processing raw MS output and applying the target-decoy strategy to ensure reliable results.

Metabolomics is the systematic profiling of low-molecular-weight metabolites (<1 kDa) that represent the end products of gene expression and enzymatic activity, thereby reflecting the functional state of cells, tissues, or organisms (Roberts *et al.*, 2012). The workflow begins with careful sample collection and preparation (e.g., rapid quenching to arrest metabolism, extraction using solvent systems like methanol–chloroform–water or methanol–acetonitrile–water, **see results 5.3.3**) to capture both polar and non-polar metabolites (Hajnajafi and Iqbal, 2025). Analytical separation is typically achieved by liquid chromatography (LC), which handles a broad polarity range, or gas chromatography (GC), which requires volatile or derivatised analytes. Mass spectrometry (MS) is the gold standard for detection, owing to its sensitivity and coverage. Common MS platforms include quadrupole-time-of-flight (Q-TOF), Orbitrap, and triple quadrupole instruments; the latter is often used in targeted metabolomics via multiple reaction monitoring (MRM) (Lu, Bennett and Rabinowitz, 2008). LC–MS enables broad metabolome coverage, GC–MS provides robust annotation of primary metabolites such as amino acids, organic acids, and sugars, and capillary electrophoresis–MS (CE–MS) offers high-resolution separation of charged metabolites (Zeki *et al.*, 2020).

Two main approaches dominate the field: untargeted metabolomics is discovery-driven, aiming to measure as many metabolites as possible in an unbiased manner to capture global metabolic changes, though it requires extensive bioinformatics and validation (Schrimpe-Rutledge *et al.*, 2016). In contrast, targeted metabolomics focuses on predefined metabolites or pathways of interest, offering higher quantitative accuracy, reproducibility, and sensitivity, typically using isotope-labelled internal standards and MRM assays (Lu, Bennett and Rabinowitz, 2008; Roberts *et al.*, 2012). These complementary approaches are often integrated—untargeted studies identify candidate biomarkers or pathways, which are then validated with targeted assays (Roberts *et al.*, 2012; Zhang *et al.*, 2024).

Following acquisition, raw data undergo preprocessing—peak picking, deconvolution, alignment, and normalisation—using software pipelines such as XCMS (Tautenhahn *et al.*, 2012), MZmine (Pluskal *et al.*, 2010), or metaboanalyst (Xia and Wishart, 2016). Data are subsequently

analysed with multivariate statistics (e.g., PCA, PLS-DA) to uncover discriminant features (Roberts *et al.*, 2012), followed by annotation/identification against spectral databases such as HMDB (Wishart *et al.*, 2022), METLIN (Guijas *et al.*, 2018), or GNPS (M. Wang *et al.*, 2016). Finally, pathway enrichment and network analysis integrate metabolic alterations into biological context, enabling interpretation of fluxes through glycolysis, the TCA cycle, amino acid, or lipid metabolism (Xia, Wishart and Valencia, 2010; Patti, Yanes and Siuzdak, 2012; Chong and Xia, 2018).

2.3 Molecular Mechanisms underpinning platinum-resistance in EOC

Platinum-based chemotherapy drugs, such as cisplatin, kill cancer cells by forming covalent DNA adducts, mainly intra-strand cross-links that block replication and transcription, triggering DNA damage responses such as cell cycle arrest and apoptosis (Siddik, 2003). It also induces oxidative stress and mitochondrial damage, amplifying cytotoxicity (Galluzzi *et al.*, 2011). Acute exposure activates p53-dependent apoptosis, but cancer cells adapt via enhanced DNA repair, drug efflux, and anti-apoptotic signalling, promoting resistance. In ovarian carcinoma, key resistance mechanisms include reduced drug uptake, increased detoxification by glutathione and metallothionein, enhanced nucleotide excision repair, and inhibition of apoptosis through modulating proteins like Bcl-2 and IAP family members(H. Zhang *et al.*, 2025). Autophagy activation occurs under cisplatin stress –a cellular degradation and recycling process, which serves as a survival mechanism allowing cells to manage stress from drug-induced damage by removing damaged organelles and proteins, thus preventing apoptosis (Wang and Wu, 2014; Yang *et al.*, 2024). These complex molecular changes hinder cisplatin efficacy, highlighting the need for combinational therapies and strategies targeting DNA repair and apoptosis pathways to overcome resistance.

2.3.1 Mitochondrial contribution to chemoresistance

Mitochondria play a pivotal role in developing resistance against platinum-based chemotherapies, such as cisplatin and carboplatin, through multiple intertwined mechanisms (**Figure 4**).

Chemoresistance is a complex process driven also by various metabolic adaptations (Guerra, Arbini and Moro, 2017; Porporato *et al.*, 2017; Belisario *et al.*, 2020; Desbats *et al.*, 2020). Bioenergetic profiling of a panel of chemosensitive and chemoresistant ovarian cancer cells has shown variability in their metabolic phenotypes; notably, chemosensitive cells tend to be more glycolytic, whereas chemoresistant cells display a more metabolically active phenotype with increased oxidative phosphorylation. Platinum ions have been shown to increase metabolic

activity, and under glucose deprivation, chemoresistant cells demonstrate greater plasticity in switching between glycolysis and oxidative phosphorylation (Dar *et al.*, 2017). This shift to mitochondrial oxidative phosphorylation from glycolysis under cisplatin-treatment (Wu *et al.*, 2022) is often facilitated by metabolic enzymes such as pyruvate dehydrogenase kinase 2 (PDK2) (Kitamura *et al.*, 2021). Another key metabolic mechanism involving the rewiring of mitochondrial activity during platinum-mediated chemotherapy is the accumulation of TCA cycle metabolites—2-hydroxyglutarate (2-HG), succinate, and fumarate—collectively termed "mitochondrial oncometabolites." These oncometabolites are known to induce a pseudo-hypoxic effect (a hypoxia-like phenotype under normoxia) (Hayashi *et al.*, 2019), which significantly contributes to drug resistance (Laukka *et al.*, 2016; Pan *et al.*, 2017; Godel *et al.*, 2021).

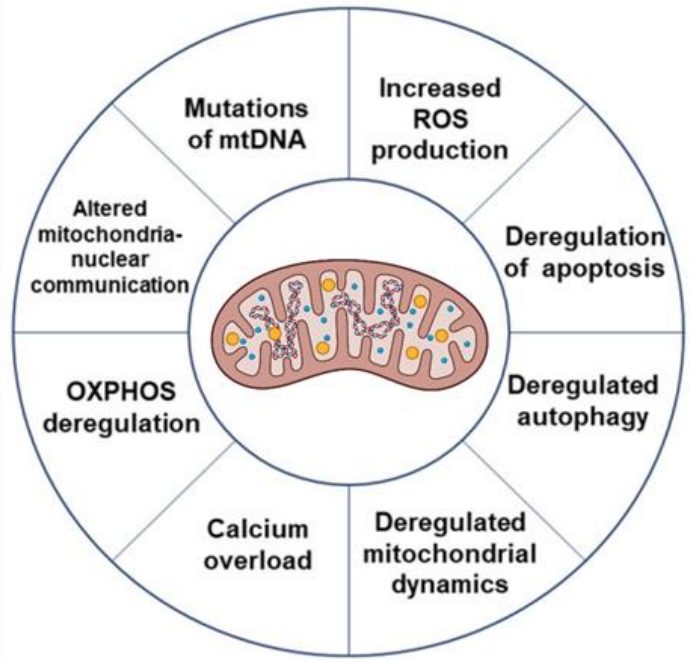

Figure 4: Mitochondrial contribution in driving platinum resistance in OC
Mitochondrial dysfunction arises from multiple interconnected processes, including mutations in mitochondrial DNA (mtDNA), increased reactive oxygen species (ROS) production, deregulation of apoptosis, impaired autophagy, disrupted mitochondrial dynamics, calcium overload, oxidative phosphorylation (OXPHOS) deregulation, and altered mitochondria–nuclear communication. Together, these alterations compromise mitochondrial homeostasis, bioenergetics, and signalling, contributing to the development and progression of diverse pathological conditions. Figure adapted from (De Rasmo *et al.*, 2023)

Reactive oxygen species (ROS), generated predominantly in mitochondria by the electron transport chain (ETC), also contribute substantially to the cytotoxicity of cisplatin and carboplatin. These drugs, in fact, lead to increased ROS levels, inducing oxidative stress and triggering cell death (Kleih *et al.*, 2019). However, chemoresistant cells often adapt by upregulating mitochondrial antioxidant defences, such as increasing pentose phosphate pathway flux for

NADPH production (Catanzaro *et al.*, 2015) and glutathione production (Nunes and Serpa, 2018) or upregulating superoxide dismutase 2 (SOD2) (Amano *et al.*, 2019), reducing mitochondrial ROS accumulation. This decrease in oxidative damage helps cancer cells continue proliferating and metastasising (Nunes and Serpa, 2018; Kim et al., 2022) even in platinum-based drugs.

Mitochondrial quality control mechanisms, including fusion, fission, and mitophagy, are also closely connected to chemoresistance (Cocetta, Ragazzi and Montopoli, 2019; Xie *et al.*, 2021). Platinum-mediated drugs are known to reduce mitochondrial membrane potential, leading to reduced ATP production and increased ROS (Choi *et al.*, 2015). Resistant tumours enhance the removal of damaged or dysfunctional mitochondria through mitophagy, preventing the accumulation of pro-apoptotic mitochondrial fragments (Dong and Zhang, 2024; Huang *et al.*, 2025; Yan *et al.*, 2025). For instance, genetic or pharmacological inhibition of mitophagy receptor, BNIP3, has been shown to improve platinum sensitivity in ovarian and cervical carcinoma (Vianello *et al.*, 2022).

Ovarian cancer cell lines show diversity in mitochondrial dynamics, i.e., fusion-fission levels, and it plays a crucial role in determining the sensitivity to chemotherapy (**Figure 5**). Cisplatin-sensitive cells show mitochondrial fragmentation upon cisplatin treatment, but resistant cells do not (Kong *et al.*, 2014). However, the resistant cells show increased cisplatin-sensitivity if mitochondrial fission is induced by other compounds such as Piceatannol (Farrand *et al.*, 2013). Simultaneously, altered mitochondrial dynamics maintain mitochondrial membrane stability, limiting the release of apoptotic factors such as cytochrome c, and thereby hindering drug-induced cell death pathways (Suen, Norris and Youle, 2008; Bokil and Sancho, 2019a). A recent study has described a mechanistic link between mitochondrial fission and mitophagy in rescuing cisplatin sensitivity in ovarian cancer cells. Suppression of Cullin 4 ubiquitin ligase (a type of E3 ubiquitin ligase) enhances mitochondrial fragmentation and by recruiting Dynamin-related protein 1 (DRP1) to dysfunctional mitochondria, which were further subjected to mitophagic clearance and thereby restored cisplatin sensitivity in resistant OC cells (Meng *et al.*, 2022).

Furthermore, mitochondria regulate intrinsic apoptotic signalling by balancing pro- and anti-apoptotic proteins. Resistant OC cells downregulate pro-apoptotic proteins like MOAP-1, BAX, and BAK, while increasing anti-apoptotic factors such as Bcl-2, stabilising mitochondrial membranes and preventing the initiation of apoptosis (Dai *et al.*, 2016; Yuan *et al.*, 2020). This disruption of apoptotic pathways is essential for the survival of chemotherapy-resistant cancer cells (Cocetta, Ragazzi and Montopoli, 2019).

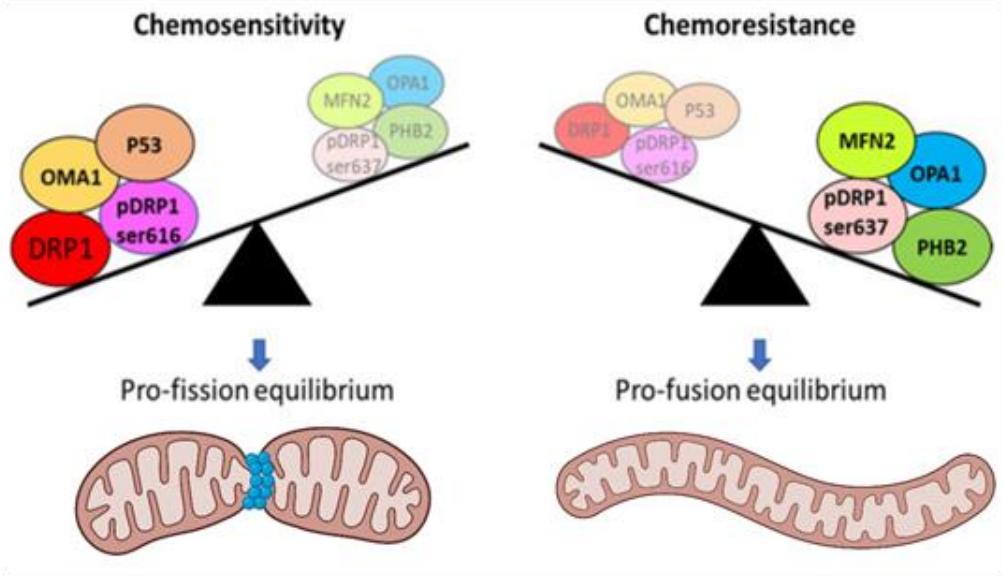

Figure 5: Key players in regulating mitochondrial dynamics in chemoresistance
Mitofusin 2 (MFN2), optic atrophy protein 1 (OPA1), and dephosphorylated dynamin-related protein (DRP1) at S637 promote fusion, which drives chemoresistance. While fragmentation of mitochondria, which is regulated by zinc metallopeptidase OMA1, DRP1 total protein levels and phosphorylation on S616, as well as p53, can restore sensitivity. Figure adapted from (De Rasmo *et al.*, 2023)

Mitochondrial DNA (mtDNA) lacks histones and introns (only 10% of the total mitochondrial genome) and therefore is more susceptible to free radical-induced mutation in the coding regions. Nuclear DNA repair mechanisms efficiently reverse platinum-induced damage; however, mitochondrial DNA lacks comparable repair efficiency (Penta *et al.*, 2001). Targeting mitochondrial genomes offers a potential strategy to overcome resistance. Therapeutics that direct cisplatin or carboplatin to mitochondria can increase mtDNA damage, culminating in elevated mitochondrial dysfunction and apoptosis, circumventing conventional resistance mechanisms (Marrache, Pathak and Dhar, 2014). The mtDNA encodes essential components for mitochondrial respiration and apoptosis regulation, and mtDNA content correlates with mitochondrial ROS production(Kleih *et al.*, 2019). In cancer cells, mtDNA copy numbers are often increased along with the two transcription factors –TFAM and TFB2M. Tissue samples from ovarian cancer patients further show increased mtDNA content as well as TFAM levels compared to controls (Signorile *et al.*, 2019). Studies suggest that this increase in mtDNA copy number is an adaptive strategy against platinum-mediated insults. Subsequently, lowering mtDNA copy number by silencing TFAM was found to sensitise cancer cells against cisplatin (Mei *et al.*, 2015; Kleih *et al.*, 2019).

Calcium homeostasis within mitochondria further influences resistance. Upregulation of mitochondrial stress proteins like Lon protease modulates mitochondrial calcium release through the Na^+/Ca^{2+} exchanger (NCLX) (Tangeda *et al.*, 2022). This finely tuned calcium signalling guides downstream survival pathways, including the activation of the PYK2-SRC-STAT3-IL6 axis, which collectively enhances cellular survival and inflammatory responses, thereby promoting resistance (Pathak *et al.*, 2020; Huang, Lang and Li, 2022). MicroRNAs acting within mitochondria (mitochondrial miRNAs) also contribute to this process (Méndez-García *et al.*, 2025). For instance, the downregulation of mitochondrial miR-5787 in resistant cancer cells impacts mitochondrial protein translation and glucose metabolism, fostering a cellular environment conducive to chemoresistance through optimised mitochondrial function and energy supply (Chen *et al.*, 2019).

In conclusion, mitochondria act as central hubs coordinating resistance to cisplatin and carboplatin through DNA modifications, oxidative stress regulation, quality control, metabolic adjustments, apoptosis regulation, and gene expression changes (Cocetta, Ragazzi and Montopoli, 2019). A thorough understanding of these mechanisms highlights mitochondria as promising targets for innovative therapeutic strategies to increase tumour sensitivity to platinum-based chemotherapy and improve clinical outcomes.

2.4 Protein post-translational modifications sustain cancer cells' chemoresistance

Another key contributor to chemoresistance in ovarian cancer is protein post-translational modifications (PTMs), which are covalent chemical alterations after protein synthesis and represent a significant source of proteomic diversity. Recognising PTMs as key contributors to the so-called "proteoform explosion" has replaced the earlier, oversimplified paradigm of "one gene–one protein"(Zecha *et al.*, 2022). Indeed, despite the shared genetic blueprint across human cells, the combined influence of DNA mutations, alternative mRNA splicing, and PTMs gives rise to a vast repertoire of proteoforms, thereby greatly amplifying the complexity of gene expression outcomes (**Figure 6**) (Zhong *et al.*, 2023a).

Initially, PTMs were studied individually at the level of single residues, but it is clear that proteins often harbour multiple modifications that can act in synergy or antagonistically. Histones provide the most prominent and studied example, where diverse PTMs collectively establish the "histone code," a central mechanism of epigenetic regulation (Lothrop, Torres and Fuchs, 2013). Beyond histones, PTMs on non-histone proteins regulate fundamental aspects of protein biology

– such as stability, protein-protein and protein-nucleic acid interactions, subcellular localisation, and enzymatic activity. While phosphorylation, acetylation, methylation, and ubiquitination remain the most widely studied, more than 650 distinct protein modifications have been described, reflecting the intricacy of this regulatory layer across physiological and pathological contexts (Zhong *et al.*, 2023a). The rapid evolution of mass spectrometry (MS) technologies over the past decade and a half has overcome many barriers to study PTMs while establishing MS as the gold standard for comprehensive PTM mapping and quantification, and providing insights that conventional molecular biology approaches could not achieve (Mü, 2017).

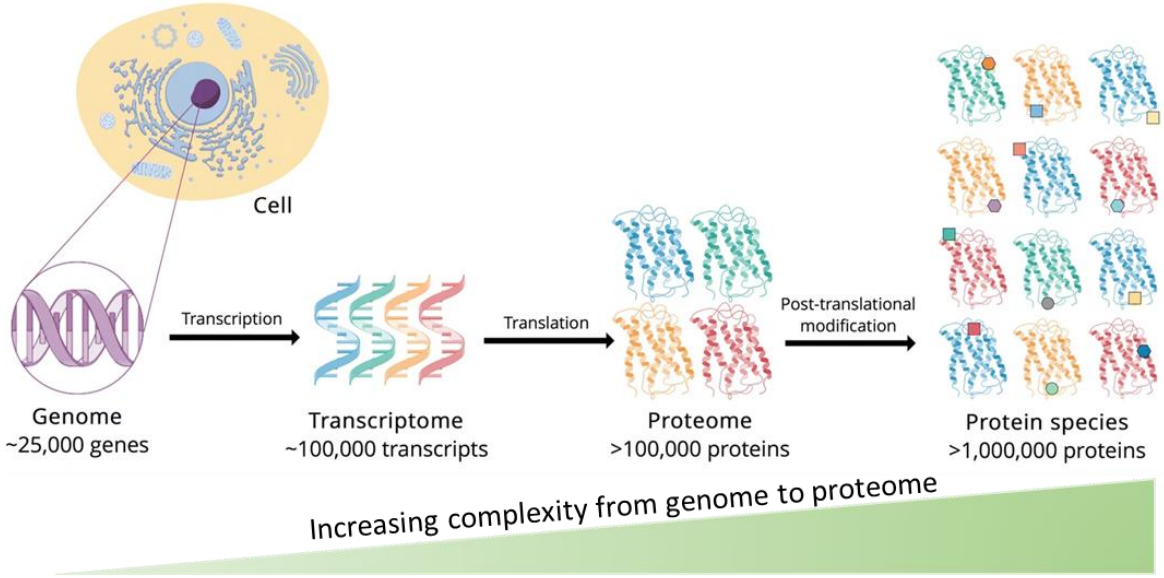

Figure 6: Post-translational modifications confer complexity to the cellular proteome
Figure adapted from (Virág *et al.*, 2020)

Phosphorylation confers chemoresistance in ovarian cancer by activating key signalling pathways such as PI3K/Akt, STAT3, and MAPK, which promote cell survival, proliferation, and DNA repair, while inhibiting apoptosis (Zhang *et al.*, 2019). For example, c-Kit-mediated phosphorylation of prohibitin enhances ovarian cancer stemness and resistance via Notch3—PBX1 signalling (Fang *et al.*, 2020). Similarly, phosphorylation of proteins like BAD at Ser99 contributes to therapy resistance by regulating cancer stem cell-like behaviour (Wang *et al.*, 2020). Acetylation, particularly regulated by sirtuin (SIRT) family proteins, modulates chemoresistance through epigenetic regulation and metabolic reprogramming (Grzeczka *et al.*, 2025). SIRT-mediated deacetylation affects chromatin remodelling, leading to increased DNA repair and an altered transcriptional programs that enhance ovarian cancer cell survival under chemotherapy stress (Qin *et al.*, 2017; Sun *et al.*, 2019). Lactylation, a novel post-translational modification arising from metabolic reprogramming, influences chemoresistance by modifying histone and

nonhistone proteins, thereby regulating gene expression and promoting adaptation to the tumour microenvironment (W. Zhang *et al.*, 2025; Yi *et al.*, 2025). Though primarily studied in other cancers, emerging data suggest that lactylation similarly supports ovarian tumour cell survival and drug resistance via epigenetic changes linked to altered metabolism (Ren *et al.*, 2025).

Together, these post-translational modifications create a complex regulatory network that fine-tunes ovarian cancer cells' response to chemotherapy by promoting survival, stemness, and metabolic flexibility, ultimately driving chemoresistance.

2.4.1 Protein Arginine-(R) methylation and protein R-methyltransferases (PRMTs)

Among 650 different types of PTMs discovered so far, protein arginine-(R) methylation is a widespread post-translational modification (PTM) that occurs on diverse nuclear and cytoplasmic proteins (Larsen *et al.*, 2016). It involves transferring one or more methyl groups (–CH_3) onto the guanidino side chain of arginine (R) residues within polypeptides. This modification plays essential roles in numerous cellular processes, including DNA damage repair (Brobbey *et al.*, 2022; Li *et al.*, 2023), transcriptional activation and repression (Guccione and Richard, 2019), pre-mRNA splicing (Fong *et al.*, 2019), translation (Wei *et al.*, 2021), miRNA biogenesis (Spadotto *et al.*, 2020), immune responses (Dai *et al.*, 2022; Fedoriw *et al.*, 2022), and cell cycle regulation (Kleinschmidt *et al.*, 2012; Raposo and Piller, 2018) (**Figure 7A**).

Like many PTMs, R-methylation is regulated by three groups of proteins: "writers," which deposit the modification, "erasers," which remove it, and "readers," which recognise and bind to methylated residues (Biswas and Rao, 2018; Zhou *et al.*, 2021). The enzymes responsible for catalysing this modification are the protein R-methyltransferases (PRMTs). All PRMTs utilise S-adenosylmethionine (SAM) as the methyl donor, and based on their catalytic activity, PRMTs are divided into three classes: type III enzymes introduce a single methyl group (monomethylarginine/ MMA), type II enzymes catalyse symmetric dimethylation (SDMA), and type I enzymes catalyse asymmetric dimethylation (ADMA) (Tewary, Zheng and Ho, 2019) (**Figure 7B**).

In contrast to lysine methylation, the existence of bona fide arginine demethylases remains poorly characterised. The 2-oxoglutarate-dependent dioxygenase JMJD6 was reported to demethylate H4R3 histones (Chang *et al.*, 2007; Poulard, Corbo and Le Romancer, 2016; Ganesan *et al.*, 2018; Liu *et al.*, 2023). Recently, Mina53 was identified to remove methylation from H4R3 residue and contribute to maintaining neural stem cell identity(Zhou *et al.*, 2024). An alternative mechanism involves peptidyl-arginine deiminase 4 (PAD4), which can convert methylated arginine

residues into citrulline, effectively acting as a regulatory demethylation surrogate (Thompson and Fast, 2006; Jones *et al.*, 2009). Tudor domain-containing proteins, including SMN, SPF30, and members of the TDRD protein family (TDRD1/2/3/6/9/11), primarily mediate recognition of methylated arginine residues. Within these proteins, aromatic residues form a cage stabilising methylated arginine through cation–π interactions, where the added methyl groups enhance hydrophobic contacts (Blanc and Richard, 2017).

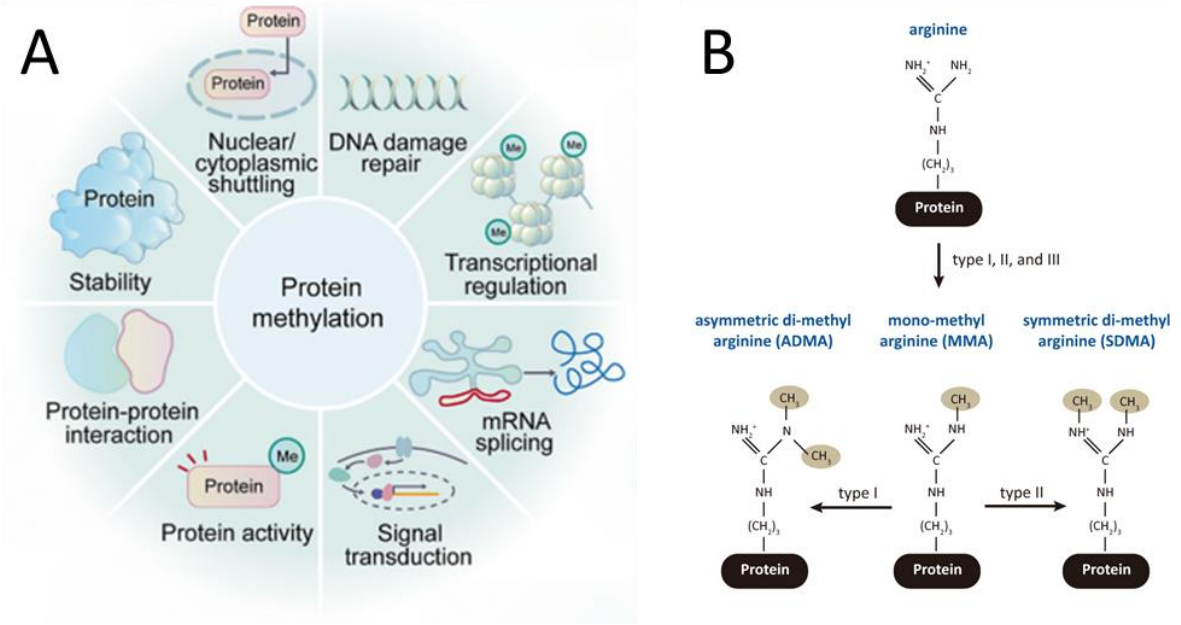

Figure 7: Biological processes regulated and reactions catalysed by R-methylation
A: Different biological processes that are regulated by protein R-methylation in both physiological and pathological conditions. Figure adapted from (Zhong *et al.*, 2023b). **B:** Enzymatic reactions carried out by three different PRMT types. All PRMTs can generate monomethylated arginine (MMA). While Type-III does not modify the R-residue further, Type-I and II add another methyl-group asymmetrically and symmetrically, respectively. Figure adapted from (Hwang *et al.*, 2021a)

There are nine different isoforms of PRMTs (PRMT1-9) that comprise all three types (**Figure 8**) and share a common target motif, the RGG/RG sequence, where glycine residues flank arginine (Bedford and Clarke, 2009). However, PRMTs also exhibit isoform-specific substrate preferences, such as GRG motifs recognised by PRMT5 (Musiani *et al.*, 2019) and PR motifs targeted by PRMT4 (Shishkova *et al.*, 2017). The addition of a methyl group alters the steric and hydrophobic properties of arginine side chains without affecting their net positive charge. Since the guanidino group of arginine provides multiple hydrogen-bond donors, methylation frequently modulates protein–protein, protein–RNA, and protein–DNA interactions by imposing steric hindrance and altering binding affinities (Blanc and Richard, 2017).

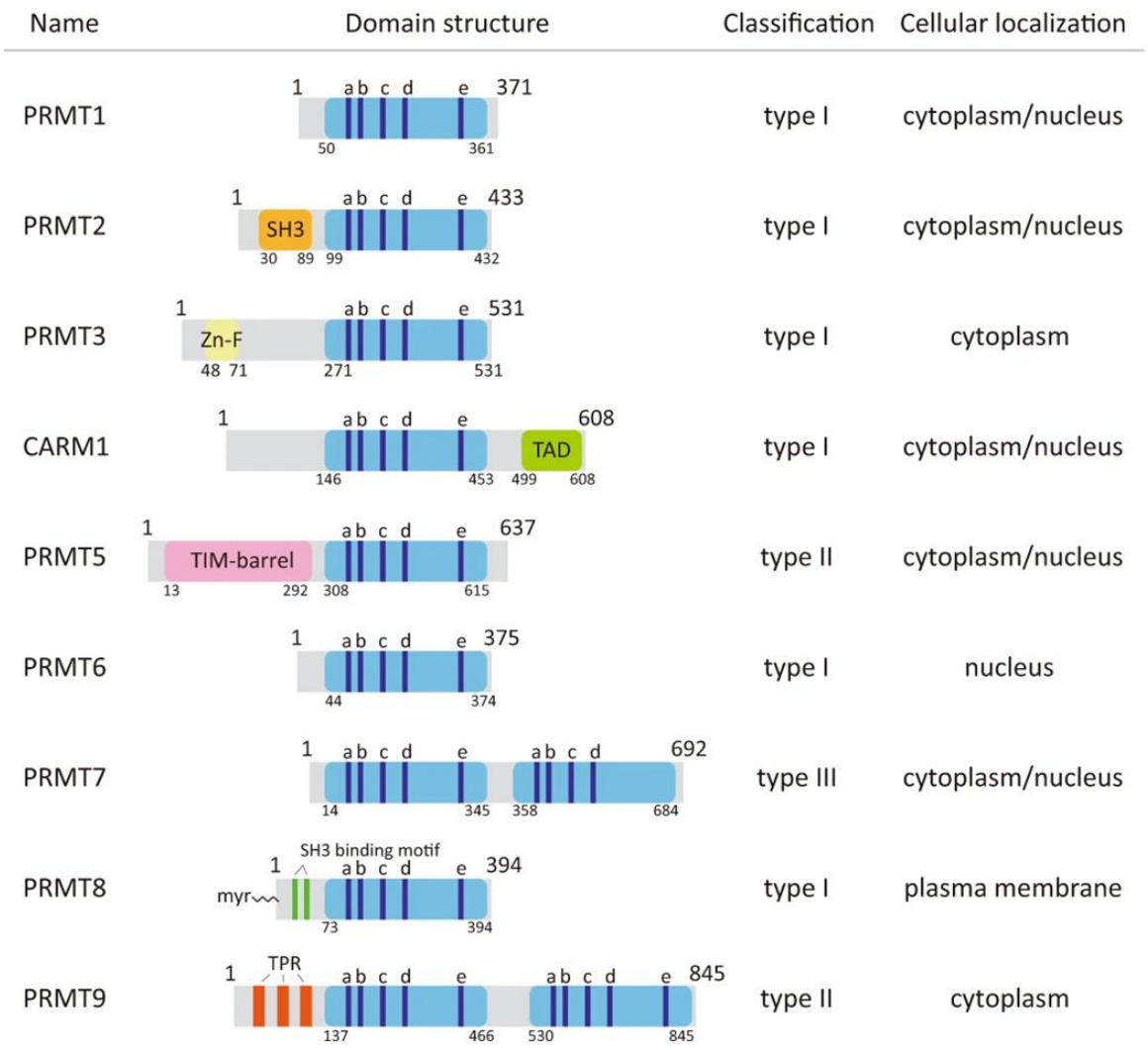

Figure 8: Isoforms of PRMTs
The nine different family members of mammalian PRMTs (PRMT1-9) identified so far and their different structures, where the dark blue lines (a, b, c, d, etc.) depict shared and conserved motifs. They are presented along with their respective classes based on their mode of action, followed by their subcellular localisation. Figure adapted from (Hwang *et al.*, 2021b)

2.4.2 Protein R-methylation and PRMTs in cancer

Dysregulated PRMT expression and function have been linked to multiple cancers, often contributing to tumour progression and poor prognosis (Wu *et al.*, 2021; Li *et al.*, 2024; Kaganovski *et al.*, 2025). In the following paragraphs, I have tried to summarise the role of PRMTs in several cancer types, focusing on ovarian cancer and chemoresistance.

PRMT1: As the predominant type I enzyme, PRMT1 is responsible for a significant portion (about 85%) of cellular arginine methylation (Tewary, Zheng and Ho, 2019). Elevated PRMT1-driven ADMA levels have been observed in lung cancer, and PRMT1 contributes to transcriptional

regulation, telomere stability, DNA repair, and modulation of key proteins like p53, 53BP1, and BRCA1, affecting cancer cell proliferation and survival (Qaddoura *et al.*, 2025). Notably, differential expression of PRMT1 in ovarian cancer predicts sensitivity to platinum-based therapy, suggesting their involvement in the chemoresistant processes (Matsubara *et al.*, 2021). In response to cisplatin, PRMT1 is phosphorylated by the double-strand break repair enzyme –DNA-PK, leading to its recruitment to chromatin where it deposits the H4R3me2a mark. The increase in methylation activates a senescence-associated secretory phenotype (SASP), and inhibition of PRMT1 sensitises ovarian cancer cells to cisplatin by reducing clonogenic survival (Musiani *et al.*, 2020). PRMT1 mediated ADMA at R179/R181/R183 on bromodomain containing protein 4 (BRD4) crosstalks with phosphorylation of this protein and dictates invasiveness in ovarian cancer (Liu *et al.*, 2023).

PRMT4/CARM1: PRMT4, initially identified as a co-activator associated with PRMT1, functions as a transcriptional co-activator, placing ADMA marks (H3R17me2a, H3R26me2a) associated with gene activation (Suresh, Huard and Dubois, 2021). CARM1 is frequently overexpressed in ovarian cancer and increases the methylation of chromatin remodellers such as BAF155 and promotes EZH2-mediated silencing of tumour suppressor genes (Wang *et al.*, 2014; Kim *et al.*, 2021). Furthermore, pharmacological inhibition of EZH2 alone or in combination with PARP inhibitors has been shown to increase the survival of CARM1-expressing ovarian cancer xenograft models (Karakashev *et al.*, 2018; Karakashev and Zhang, 2020).

PRMT5: PRMT5, the most predominant Type-II PRMT, directly correlates with aggressive phenotypes in EOC, with an expression level negatively correlating with patient survival (Bao *et al.*, 2013). PRMT5 was also found to methylate glycolytic enzyme enolase 1 symmetrically, contributing to increased glycolytic flux in ovarian cancer progression(Xie *et al.*, 2023). It also methylates H4R3 residue at the promoter of DNA damage repair genes, such as BRCA1/2, ATM, and RAD51 and plays a significant role in conferring chemoresistance. Furthermore, inhibition of PRMT5 has shown a synergistic effect with PARP inhibition (Carter *et al.*, 2023). In high-grade serous ovarian cancer, PRMT5 sustains chemoresistance by both escaping KEAP1 degradation (Ozturk *et al.*, 2025) and methylating METTL3 at R36 (Xia *et al.*, 2025), thereby enhancing stress-response transcription and RAD51-mediated DNA repair. Inhibiting PRMT5 disrupts these pathways, sensitizing tumours to platinum therapy.

PRMT6: Similar to platinum-based drugs, ovarian cancer patients are also treated with paclitaxel and develop resistance, which leads to major relapse. Expression of PRMT6, a Type-I PRMT, was

found to be higher in paclitaxel-resistant EOC cells compared to paclitaxel-sensitive cells. PRMT6 increases the asymmetric dimethylation mark on H3R2 residue and promotes transcriptional activation of glucose-6-phosphate dehydrogenase (G6PD), which is a crucial enzyme in the oxidative pentose phosphate pathway. G6PD regulates the expression of glutathione S-transferase P1 downstream and helps EOC cells to combat the oxidative stress induced by paclitaxel, thereby conferring resistance (Feng *et al.*, 2020). Additionally, increased expression and enzymatic activity of G6PD have also been linked with cisplatin resistance in EOC, and inhibition of G6PD could restore drug sensitivity in cisplatin-resistant cells (Catanzaro *et al.*, 2015). Even though a clear mechanistic link between PRMT6 and G6PD is missing in the context of cisplatin resistance, it could be worth investigating.

2.5 Protein R-methylation and metabolic reprogramming in cancer

The central focus of this work was to elucidate a novel mechanism to explain the onset of chemoresistance driven by mitochondrial metabolic rewiring mediated by R-methylation catalysed by PRMTs. Even though the link between metabolic reprogramming and R-methylation in contributing to the onset of chemoresistance remains a large gap in the knowledge, in recent years, some studies have been published establishing links between R-methylation (on both histone and non-histone proteins) and metabolic reprogramming in the context of several cancers. In the following paragraph, I have tried to summarise evidence from the literature on R-methylation, especially on non-histone proteins driving metabolic reprogramming in several cancer types.

PRMT4/CARM1 is possibly so far the most studied PRMT in the context of metabolic reprogramming. CARM1 negatively regulates glycolysis and the TCA cycle, and is found to be suppressed in patient samples derived from hepatocellular carcinoma and pancreatic ductal adenocarcinoma, respectively. In liver cancer, CARM1 acts as a glucose sensor and fine-tunes the balance between glucose availability and metabolism by regulating glycolytic flux. Upon glucose deprivation, CARM1 gets upregulated, increases ADMA mark on R234 residue of glyceraldehyde-3-phosphate dehydrogenase (GAPDH), inhibits its catalytic activity, and thus reduces the glycolytic flux (Zhong *et al.*, 2018). Similarly, CARM1 inhibits the dimerisation of the cytosolic form of malate dehydrogenase (MDH1) by promoting methylation at R248, and thereby reduces the flux of glutamine metabolism and antioxidant response in pancreatic cancer cells (Y. P. Wang *et al.*, 2016). Hypomethylation of MDH1 at R248 and GAPDH at R234 was reported in patient samples of pancreatic and liver cancer, respectively (Y. P. Wang *et al.*, 2016; Zhong *et al.*, 2018). In

contrast, in non-small cell lung carcinoma (NSCLC), CARM1 positively regulates glucose metabolism by hypermethylating O-GlcNAc transferase (OGT) at R348 and upregulating c-Myc expression. In NSCLC patient tissues, CARM1 levels were found to be elevated compared to healthy controls (Lin *et al.*, 2024). In breast cancer cells, CARM1 regulates the balance between glycolysis and mitochondrial oxidative phosphorylation by modulating methylation on R445/337/455 on pyruvate kinase M2 (PKM2). The interaction of methylated PKM2 with inositol-1,4,5-triphosphate receptors inhibits its activity and suppresses the influx of calcium ions into mitochondria from the endoplasmic reticulum. The reduction of calcium ions inside mitochondria impairs their activity, therefore reducing oxidative phosphorylation and increasing glycolysis, which in turn promotes tumour progression and migration (Liu *et al.*, 2017). This increase in glycolytic capacity further supports *de novo* serine synthesis and promotes survival when extracellular serine is limited (Abeywardana *et al.*, 2018). Pentose phosphate pathway (PPP) enzyme ribose-5-phosphate isomerase A (RPIA) is also a reported target of CARM1. Increased methylation on the R42 residue on RPIA increases oxidative PPP flux and increases NADPH production. This hypermethylation helps colorectal cancer cells produce antioxidants and nucleotides and reinforces their survival even under glucose deprivation (Guo *et al.*, 2020).

PRMT3 is the only PRMT that is exclusively cytosolic, and its role in regulating metabolic pathways is slowly emerging (Hsu and Hung, 2023). GAPDH was also reported as a PRMT3 substrate, but on a different site, namely R248. Hypermethylation on this site was found to increase the catalytic activity of GAPDH and increase both glycolysis and oxidative phosphorylation in pancreatic cancer cells (Hsu *et al.*, 2019). PRMT3 is often found to be upregulated in hepatocellular carcinoma. The E338 residue of PRMT3 interacts with lactate dehydrogenase A (LDHA) and increases ADMA mark on R112 residue. Overall, this modification increases the activity of the enzyme, resulting in enhanced glycolysis and lactate production, which in turn increases tumour progression (Lei *et al.*, 2022). PRMT3 methylates and stabilises HIF1α at R282 and promotes oncogenic functions by increasing glycolysis in colorectal cancer and glioblastoma (Zhang *et al.*, 2021; Liao *et al.*, 2022). C-Myc is known to transcriptionally modulate mitochondrial glutamolysis (Wise *et al.*, 2008), resulting in 'glutamine addiction'(Wise and Thompson, 2010), a classic hallmark of many cancer types. Stabilisation of Myc by PRMT3 contributes to this mechanism, which is reported in the context of colorectal cancer (Hu *et al.*, 2021).

PRMT6 is another type-I R-methyltransferase that regulates the oxidative pathway of PPP, antioxidant production and glycolysis in lung cancer cells, promoting tumour growth and conferring chemoresistance. PRMT6 methylates 6-phospho-gluconate dehydrogenase (6PGD) at R234, enhancing its activity. Simultaneously, it methylates glycolytic enzyme, α-enolase (ENO1) at

R9 and R372, increasing its dimer formation and thus increasing glycolytic flux. Targeting PRMT6 showed enhanced cisplatin sensitivity in lung cancer cells (Sun *et al.*, 2023).

Interestingly, even though PRMT1 is the most active PRMT and catalyzes the majority of the cellular methylation, its role in metabolism has not been investigated systematically. However, studies have shown that PRMT1 is responsible for the site-specific methylation of PFKFB3 at arginine residues R131 and R134. This methylation stabilises PFKFB3 and supports glycolytic flux by promoting the production of fructose 2,6-bisphosphate (F-2,6-BP), which activates phosphofructokinase-1 (PFK-1). Under conditions where this methylation is reduced—such as during CO-mediated inhibition of cystathionine β-synthase (CBS)—PFKFB3 becomes polyubiquitinated and degraded, leading to suppressed glycolysis and a preferential shunt of glucose towards PPP. This shift enhances NADPH production, supporting redox balance and cancer cell resistance to oxidative stress and chemotherapy. Thus, PRMT1-catalysed arginine methylation acts as a molecular switch in cancer metabolism, determining whether glucose is used for energy production or redirected for antioxidant defense via the PPP (Yamamoto *et al.*, 2014). Another study shows PRMT1 methylates DDX3 at R88 and R93, stabilising it by preventing its ubiquitin-mediated degradation. Stabilised DDX3 translocates to mitochondria, where it enhances the translation of PINK1, a kinase involved in mitochondrial quality control. By regulating both mitochondrial biogenesis and mitophagy, PRMT1 ensures mitochondrial health in cancer cells—crucial for stemness and metastatic potential. Inhibition of the PRMT1-DDX3 axis impairs these mitochondrial processes, diminishing metastatic capability and increasing sensitivity to therapeutic interventions (Hsu *et al.*, 2024).

3. Aim of the project

3.1 Preliminary evidence: cisplatin treatment activates mitochondrial genes post-transcriptionally in SkOV3 cells

Overexpression of PRMTs and the linked aberrant methylation pattern of target proteins have been mechanistically correlated with cancer regulation, progression, poor prognosis and drug resistance (Wu *et al.*, 2021; Li *et al.*, 2024; Kaganovski *et al.*, 2025). In 2020, our group discovered that, in chemoresistant EOC (SkOV3) cells, PRMT1 is recruited at platinum-mediated double-strand breaks (DSBs) by the DSB repair enzyme DNA-PK. In this context, we observed that, as an acute response to cisplatin, PRMT1 catalyses asymmetric dimethylation of Arginine 3 of histone H4 (H4R3), triggering transcriptional induction of the senescence-associated secretory pathway (SASP) and thus contributing to activation of the protective process leading to chemoresistance (Musiani *et al.*, 2020).

We acquired in-house the proteomic and transcriptomic profiles of untreated and cisplatin-treated SkOV3 cells and performed an integrative analysis of these two molecular layers. We carried out a 2D annotation enrichment analysis test to understand whether the fold changes of different pathways are enriched in respect to the global distribution of all proteins or transcripts. We ranked genes/proteins from transcriptomic/proteomic datasets separately, based on the adjusted p-value that was derived from a multivariate variance analysis test (MANOVA test). The significantly deviating terms were scored based on their magnitude of gene expression, significance and direction of gene expression change and plotted on a graph. Thus, we obtained four groups that were concordantly modulated (up/down both at protein and transcript level) and discordantly modulated (protein up/transcript down and protein down/transcript up). Interestingly, among these four groups, we observed post-transcriptional regulation of several metabolic and mitochondrial genes (right quadrants, top and bottom, highlighted in orange and red). In fact, these genes were involved in glutathione metabolism (e.g., GPX1, GCLM), mitochondrial transcription factor (TFAM), electron transport chain (NDUFA9) and mitochondrial distribution and dynamics regulation (RHOT1) (**Figure 9**).

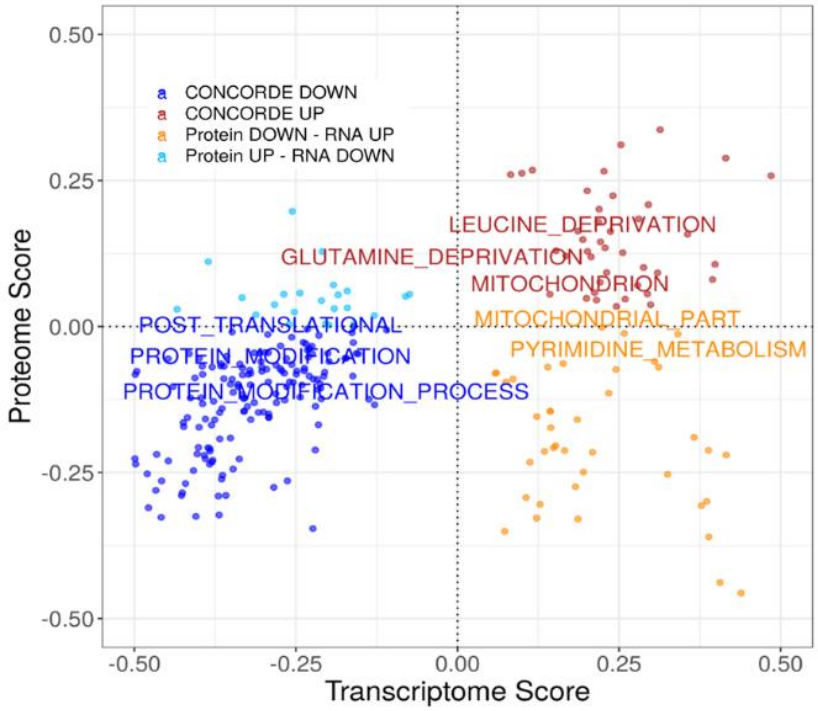

Figure 9: 2D annotation enrichment based on protein and mRNA fold changes (CDDP over untreated)
Proteomic and transcriptomic datasets were derived from SkOV3 cells treated with 20μM cisplatin for 24h. The 2D annotation enrichment analysis tests whether the fold changes of each annotation term (e.g., pathways) tend to be systematically larger or smaller than the global distribution of values across all proteins or transcripts. Fold changes are ranked separately for proteins and transcripts. A MANOVA test is then performed on the ranked data, with the resulting p-value representing the 2D annotation enrichment significance. This p-value is adjusted for multiple comparisons using the Benjamini-Hochberg correction. A score is calculated after identifying annotation terms with significantly deviating protein/mRNA level distributions. The score is represented as a pair of coordinates (sx, sy), which are used for plotting. The plot is subdivided into four quadrants, with the lower-left and upper-right quadrants corresponding to concordant down- and up-regulation, respectively, while the lower-right and upper-left quadrants indicate anti-correlating down- or up-regulation.

3.2 Hypothesis

Platinum-based chemotherapeutics exert their cytotoxic effects primarily through the induction of genotoxic stress, leading to DNA damage and activation of cellular stress response pathways (Siddik, 2003; Kitamura *et al.*, 2021). In cancer cells, however, this stress can trigger adaptive mechanisms that promote survival and contribute to the development of chemoresistance (Raaphorst, Li and Yang, 2006; Wang *et al.*, 2021). Two apparently unrelated, yet potentially interconnected, processes—mitochondrial metabolism and protein arginine methylation—may play central roles in this adaptation.

Mitochondria are key regulators of cellular energy production, redox balance, and apoptotic signalling (Galluzzi *et al.*, 2011; Pan *et al.*, 2017). Alterations in mitochondrial metabolism under genotoxic stress can support survival by shifting bioenergetic profiles, enhancing antioxidant capacity, or reprogramming metabolic pathways to meet the demands of damaged yet proliferating cells (Porporato *et al.*, 2017; Bokil and Sancho, 2019b). In parallel, protein arginine methyltransferases (PRMTs) catalyse the methylation of arginine residues on target proteins, modulating their activity, subcellular localisation, or protein-protein/nucleic acid interactions (Yang and Bedford, 2012; Li *et al.*, 2024). This post-translational modification can influence various processes relevant to stress adaptation, including transcriptional regulation, RNA processing and splicing, translation, DNA repair, and signal transduction (Guccione and Richard, 2019; Hwang *et al.*, 2021c).

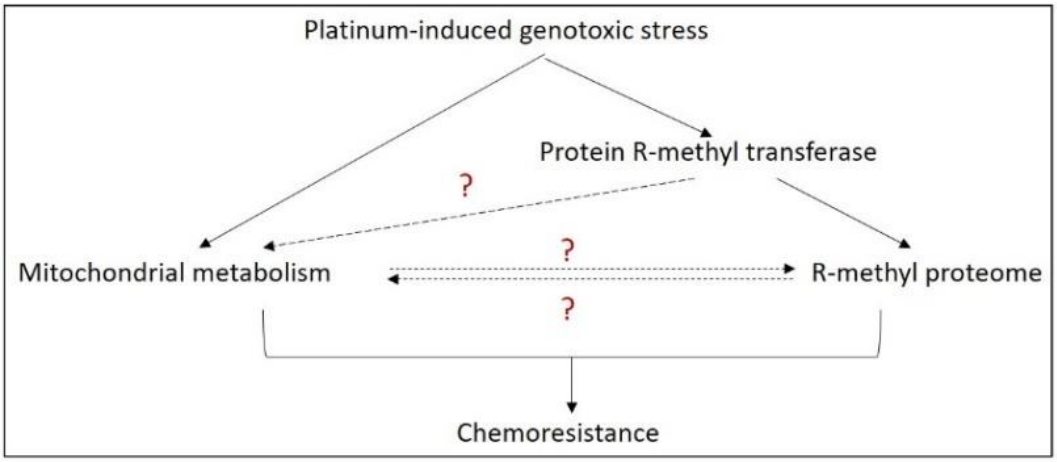

Figure 10: Working model
Schematic representation of the working model underlying the hypothesis. The dotted lines address areas where we attempted to provide experimental evidence

Based on all this evidence, we formulated our hypothesis – that platinum-induced genotoxic stress influences PRMT activity and the R-methyl proteome, which may in turn, affect mitochondrial metabolism/function. Conversely, mitochondrial metabolism may regulate the R-methyl proteome through changes in metabolite availability (e.g., S-adenosylmethionine levels) or redox state, thereby influencing methyltransferase activity. The directionality and mechanistic details of these interactions remain largely unclear, as indicated by the question marks in the diagram (**Figure 10**). Ultimately, both mitochondrial remodelling and alterations in the R-methyl proteome could converge to promote chemoresistance by enhancing DNA repair, preventing apoptosis, or facilitating metabolic plasticity. Understanding whether these two processes act independently or in a coordinated manner could be critical for defining their role in resistance to

platinum-based therapy. Elucidating these links may also reveal novel therapeutic vulnerabilities—such as targeting PRMT activity or specific metabolic pathways—that could be exploited to tackle the onset of chemoresistance in ovarian cancer. Within the scope of the PhD project, so far we have majorly focused on the regulation of mitochondrial metabolism by type-I PRMTs.

3.3 Objectives and tasks of the study

To test our model and understand how R-methylation and mitochondrial function and/or metabolism are linked in acute (short-term) and adaptive (long-term) responses to chemotherapy, we focused on protein ADMA catalysed by type-I PRMTs since these enzymes account for most R-methylation in the cell. Overall, this broad aim was addressed by undertaking the following specific tasks.

1. We initially characterised our *in-house* adaptive chemoresistance model of ovarian cancer cells by assessing mitochondrial dynamics and oxygen consumption rate, to verify whether this system recapitulates the established traits of resistance-induced cell models (**See results 5.1**).

2. In this model, we assessed the role of Type-I PRMTs in mitochondrial function, such as oxygen consumption, dynamics and membrane potential (**See results 5.2**).
3. With proteomic and metabolomic analysis, we explored and characterised changes at the proteome and metabolome levels in this adaptive EOC model of chemoresistance and integrated these complementary datasets to identify a key axis of adaptation. Furthermore, the potential role of type-I PRMTs in both acute and adaptive models of chemoresistance was assessed through pharmacological inhibition of type-I PRMTs. (**See results 5.3**).
4. To investigate metabolic adaptations underlying chemoresistance, we compared nutrient uptake and utilisation between chemosensitive and chemoresistant cells of the adaptive resistance model using stable isotope tracing. The choice of tracers was informed by steady-state metabolomics, which revealed specific metabolic impact nodes upon type-I PRMT inhibition. These nodes highlighted pathways of altered nutrient flux, thereby guiding the design of *ad hoc* isotope tracing experiments to directly quantify differences in substrate preference and utilisation between the two isogenic cell lines (**See results 5.4**).
5. We also analysed mitochondrial function upon Type-I PRMT inhibition in our model of acute chemoresistance. We integrated proteomic and metabolomic datasets to identify the node(s) regulated by Type-I PRMTs. Building on observations from the adaptive model, we additionally measured fuel dependency and capacity to determine how individual

substrates contribute to mitochondrial metabolism. This approach enabled us to evaluate whether resistant cells display a reprogrammed reliance on specific fuels to sustain energy production (**See results 5.4**).

6. Finally, we attempted to investigate the extent of R-methylation within the mitochondrial compartment by setting up a mitochondrial-focused methyl-proteomics workflow and MS-annotated high confidence R-methylation sites on mitochondrial proteins to mechanistically elucidate the connection between R-methylation and mitochondrial function/metabolism (**See results 5.5**).

4. Materials and Methods

4.1 Cell lines and culture conditions

A2780S and HeLaS3 are stored as frozen aliquots in liquid nitrogen in the DEO department. A2780R was generated by treating the parental A2780 line (A2780S) with gradually increasing doses of CBP over approximately 18 months within the TB group. The cell lines were maintained at 37°C with 5% CO2 and tested free of mycoplasma contamination. The lines A2780S, A2780R, and HeLaS3 were cultured in DMEM medium supplemented with 1% stable glutamine, 10% South American foetal bovine serum (FBS_SA, Microtech Srl S1860-500), and 1% penicillin-streptomycin. SkOV3 cells, previously used in the TB group, were kept in RPMI medium with 1% stable glutamine, 10% North American FBS (FBS_NA, Fisher Scientific, 12389802), and 1% penicillin-streptomycin.

For heavy methyl SILAC labelling, methionine-free SILAC medium (Thermo Fisher Scientific - ME22713L1) containing stable glutamine was supplemented with 10% dialysed FBS, 1% penicillin-streptomycin, 86 g/l arginine (Arg0, R0, Sigma-Aldrich), 146 g/l lysine (Lys0, K0, Sigma-Aldrich), and 30 g/l heavy (methyl-13C, d3/Met4, Sigma-Aldrich - 299154) or light methionine (Met0).

MS023 was purchased from Cayman Chemical (CAY-18361-10). MS094 was purchased from Merck (SML2548). These inhibitors were used at a final concentration of 10μM for 48h.

4.2 IC50 curve and proliferation assay

A2780S and A2780R cells were plated at a density of 2000 cells/well in a white-bottom 96-well plate. The cells were treated with DMSO, MS094 and MS023 for 48h. For the IC50, they were treated for 24h with increasing Carboplatin (hospital pharmacy of IEO) doses. The plates were taken from the incubator on the assay day and calibrated at room temperature. Cell Titer Glo solution (Promega- G7572) was added at a final dilution of 1:8 and incubated for 10minutes while protected from light. The luminescence was measured in a Glomax Discoverer luminometer.

For the proliferation assay, cells were plated at a density of 2000 cells/well in a white-bottom 96-well plate. Measurements were taken every from 0h to 96h in every 24h. All the luminescence values were normalised over 0h reading.

4.3 Western Blot analysis

Cell pellets were lysed with urea buffer (9M urea, 20mM HEPES, 1mM DTT) or RIPA buffer (50 mM Tris-HCl pH 8, 150 mM NaCl, 1% NP-40, 0.5% Sodium Deoxycholate), freshly supplemented with 1X protease inhibitor (Roche- 11697498001) and phosphatase inhibitor cocktails (Roche- 04906837001). The DNA was sheared by sonication with an ultrasonic cell disruptor (Brandson) for three cycles (each cycle 30sec ON and 30sec OFF). Then the lysates were centrifuged at 13000rpm, and the supernatant was collected in a fresh tube, while the cell debris in the pellet was discarded. The protein amount was estimated by BCA quantification using a Pierce BCA kit (Thermo Scientific- 23225), and absorbance was read at 562nm on a Glomax spectrophotometer. About 30-35µg protein for ADMA and MMA and 15µg protein for all other proteins were mixed with 1X LDS buffer (Invitrogen- NP0007), heated for 5 minutes at 95°c and loaded in an 8-12% gradient SDS-PAGE gel (Invitrogen-NP0323). The proteins were then transferred to a methanol-activated PVDF membrane (Merck Milipore - IPVH00010) for 1.5h at a steady voltage of 90-110mV. The membrane was blocked with 10% BSA for 1h and probed with primary antibodies with appropriate dilutions overnight at 4°C. The primary antibodies used in this project were the following, as summarised in **Table 1**:

Table 1: List of primary antibodies

Primary antibody	Product code	Dilution	Secondary antibody
anti-ADMA	Milipore (ASYM24-07-414)	1:1000	Rabbit (1:10,000)
anti-MMA	Cell Signaling Technologies (D5A12-(711S)	1:1000	Rabbit (1:10,000)
anti-H3	Abcam (ab1791)	1:5000	Rabbit (1:10,000)
anti-H4	Abcam (ab7311)	1:1000	Rabbit (1:10,000)
anti-vinculin	Sigma (V9131)	1:5000	Mouse (1:10,000)
anti-LC3B	Sigma (L7543)	1:1000	Rabbit (1:10,000)
anti-p62	Novus (H00008878-M01)	1:1000	Mouse (1:10,000)

anti-HSP60	Cell Signalling Technologies (BK12165S)	1:1000	Rabbit (1:10,000)
anti-TOM20	ProteinTech (11802-1-AP)	1:1000	Mouse (1:10,000)
anti-OXPHOS cocktail	Abcam (ab110413)	1:2000	Mouse (1:10,000)

Upon primary antibody incubation, the membrane was washed with 1X TBST and incubated with the appropriate secondary antibody for 1h at room temperature. After three washes with 1X TBST, the membrane was developed using Clarity western ECL solution (BioRad – 170-5061). The images were captured with an iBright Western Blot Imager from Thermo-Fisher. The iBright software provided by Thermo Fisher Scientific was used for the quantification.

4.4 Seahorse Mitostress test, Glycolytic stress test, and Fuel Flex test

A2780S, A2780R, and SkOV3 cells were seeded in 96-well plates at densities of 4000, 10,000, and 5000 cells per well, respectively and left overnight for them to attach. The next day, they were treated with 10 μM MS023/MS094 for 48 hours before the assay. The washes and the final assay were performed in Seahorse XF phenol-red-free DMEM (Agilent - 103680/RPMI medium (Agilent – 103681) supplemented with 1 mm pyruvate, 2 mm glutamine, and 10 mm glucose. For the Mitostress test (Agilent – 103793-100), oligomycin, FCCP, and rotenone/antimycin A were used at final concentrations of 1.5 μm, 1 μm, and 0.5 μm, respectively, in the injection ports. The wash and assay media were prepared without glucose for the glycolysis stress test. For this assay, glucose, oligomycin, and 2-DG were used at final concentrations of 10mM, 1μm, and 50mM, respectively (Agilent – 103020-100), in the injection ports. For the Fuel Flex test, BPTES, etomoxir, and UK5099 (Agilent – 103260-100) were used at final concentrations of 3μm, 4μm, and 2μm, respectively, in the injection ports. OCR measurements were taken using a Seahorse XF analyser following the Mitostress/glycolytic stress/ fuel flex test protocol. After the assay, cells were lysed directly on the plate with 1X RIPA buffer. The lysate was then transferred to another 96-well plate to estimate the total protein content by BCA. Raw OCR levels were normalised to the estimated total protein content using Wave software by Agilent Technologies.

4.5 DNA isolation and Quantitative Real-Time PCR

DNA was isolated with a Qiagen kit (QiaAmp DNA mini kit) suitable for both genomic DNA and mitochondrial DNA. The concentration was measured in a nanodrop. 10ng DNA was amplified for 36B4 and COXII genes using primer pairs and TaqMan probes as described below in **Table 2**:

Table 2: List of primers

36B4 (human)	Forward (10μM)	CCACGCTGCTGAACATGC
	Reverse (10μM)	TCGAACACCTGCTGGATGAC
	Probe (Texas Red, 100μM)	AACATCTCCCCCTTCTCCTTTGGGCT
COXII (human)	Forward (10μM, 100μM)	CAAACCACTTTCACCGCTACAC
	Reverse (10μM)	GGACGATGGGCATGAAACTGT
	Probe (FAM, 100μM)	AAATCTGTGGAGCAAACC

4.6 GFP-labelling of mitochondria and confocal microscopy

HEK293T cells (80% confluent) were transfected with pMXs-3XHA-EGFP-OMP25 (addgene plasmid number- 83356) using the $CaCl_2/PO_4$ precipitation method, while using a viral packaging (6μg of pUMVC) and a viral envelope (4μg of VSV-G). The media was changed 24h after transfection. Viral particles were collected 48h and 72h after transfection and filtered through a 0.45-micron filter. Each cell line was infected in two rounds, using the two separate collections. After splitting, they were kept in 10μg/ml blasticidin for antibiotic selection for 10 days. The selection procedure was repeated twice, and then the cells were expanded for further experiments.

GFP-labelled cells were plated in glass-bottom Petri dishes. Cells were fixed with 4% PFA for 10 minutes at room temperature. Then they were washed three times with PBS and incubated for 1h in the dark in a solution containing 0.1% Triton, DAPI (1:5000) and Phalloidin (1:1000). They were washed again 3x with PBS before visualisation under a Yokogawa Spinning disk confocal microscope. A 100x oil objective was used, and images were acquired in a z-stack while manually defining the top and bottom. A further systematic analysis was carried out using Fiji and Python algorithms (in collaboration with the IEO Imaging Unit) to 3D-skeletonise and quantify several morphological features while considering a quantifiable mitochondrial network which had more than one contact site (i.e., only voxels which extended beyond two points).

4.7 Mitochondrial membrane potential

A2780S, A2780R and SkOV3 cells were plated in 10cm dishes to reach 80-90% confluence after 48h of treatment with 10μM MS094 or MS023. Cells (1 million/ml) were stained with JC1 dye (Thermo Fisher Scientific- M34152) at 2μM final concentration for 15mins (A2780S) and 30 minutes (A2780R and SkOV3) at 37°c while rotating on a wheel in the dark. After loading the dye, cells were washed in 1X warm (at 37°c) PBS to remove excess dye and resuspended in 500μl of PBS. A 3-laser flow cytometer (BD FACS Celesta) was set to read absorbance. A 488nm excitation laser was used for JC1, and emission was measured at 530/30nm for green fluorescence and 576/26nm for red fluorescence. An excitation laser was used at 405nm for DAPI staining, and emission was captured at 450/50nm. A total of 100,000 events were recorded per sample on a medium flow rate (500-600 events/second).

4.8 Mitophagy analysis with mt-mKEIMA

HEK293T cells (80% confluent) were transfected with pCHAC-mt-mKEIMA (addgene plasmid number- 72342) using the $CaCl_2/PO_4$ precipitation method, and viral particles were generated as described before. The medium was changed after 24h of transfection. Viral particles were collected 48h and 72h after transfection and filtered through a 0.45-micron filter. Each cell line (SkOV3 and A2780R) was infected twice, using the two separate viral collections. The cells were sorted using a 488nm laser with a 610/620nm filter in a suitable sorting medium (PBS+2% FBS+3% penicillin and streptomycin+0.3% gentamycin) and collected in a collection medium containing (Medium+33%FBS+3% penicillin and streptomycin+0.3% gentamycin). The sorted cells were grown, treated with 10μM MS023/MS094 for 48h. 10μM CCCP treatment for 24h was used as a positive control, and 100nM Bafilomycin treatment for 6h was used for autophagosome inhibition. The measurements were taken using a 488nm and 561nm laser with a 610/20nm filter at BD FACS Celesta.

4.9 Time-lapse imaging of mitochondria

SkOV3 cells were incubated for 30 minutes at 37°C in the incubator with Mitotracker dye (pk-mito orange, Spirochorme-251SC053) diluted in cell culture medium at a 1:1000 dilution. Afterwards, the cells were washed twice in 1X HBSS, and the same solution was used for imaging. Time-lapse videos were taken in a single z-stack over a period of 2 minutes while capturing images at every 0.05s in a Yokogawa spinning-disk confocal microscope (Nikon). The videos were

denoised using the denoising software in the NIS-element application provided by Nikon.

4.10 Steady-state metabolomics analysis

Pellets of 1 million cells were collected on ice and washed 2x with ice-cold PBS. Metabolites were extracted for 10s in a tissue-lyzer with an extraction buffer composed of methanol: water: acetonitrile (55:25:20 v/v) with a spike-in of internal standards of 13-C glucose (1ng/µl), 13-C glutamine (1ng/µl) and 13-C GSH (0.2ng/µl). The lysate was centrifuged at 15,000g for 15mins at 4°c and the supernatant was dried fully under a continuous flow of N2 at 40°c in a deep 96-well plate. Dried metabolites were carefully resuspended in cold methanol: water (70:30 v/v) solution and were used to quantify energetic metabolites, carnitines, GSH and GSSG as well as SAM and SAH. 10µl of the samples were further derivatised with a derivatisation solution composed of water: ethanol: pyridine (1:1:1 v/v) and 5% PITC using a glass tube. The plate was closed, vortexed and left at room temperature for 20 minutes. Derivatised samples were dried under N2 for at least 1.5h. The samples were resuspended in 50µl of a buffer composed of 5mM diammonium acetate in methanol and water (1:1 v/v).

To quantify the metabolites of the transsulfuration pathway, the metabolites were extracted with an extraction buffer composed of 90% methanol with 0.03% (v/v) trifluoroacetic acid, 1.3mM DTT and 13C methionine as an internal standard at a final concentration of 0.1ng/µl.

Table 3: Acquisition methods of metabolomics

Metabolite/Lipid Class	Energetic metabolites (Glycolysis, TCA cycle, Pentose Phosphate Pathway), Cofactors (NAD+, NADPH), Nucleotides (ATP, ADP, AMP)	Amino Acids and Biogenic Amines	Acyl-Carnitine, SAM, SAH and GSH, GSSG
MS Instrument	Triple Quad 3500 (Sciex)	Triple Quad 3500 (Sciex)	Triple Quad 3500 (Sciex)
Ionization Mode	ESI neg	ESI pos	ESI pos
Column/Separation	Luna CN, 5µm, 100Å, LC Column, 50 x 4.6mm	C18 column	ZORBAX Stable Bond CN, 5µm, LC Column, 2.1 x 150mm
Mobile Phase	A: H_2O , B: 2mM $NH_4CH_3CO_2$ in MeOH	A: 0.2% HCOOH in H_2O, B: 0.2%	A: 0.2% HCOOH in H_2O, B: 0.2% HCOOH in ACN

		HCOOH in ACN	
HPLC Methods	Isocratic (50%)	Gradient: T0min 100%A, T5.5min 5%A, T7min 100%A	Gradient: T0min 100%A, T5.5min 5%A, T7min 100%A
Flow Rate	0.6mL/min	0.5mL/min	0.3mL/min
Detection Mode	MRM	MRM	MRM
Derivatization	No	Yes, 5% PITC in EtOH, Pyridine, H_2O (1:1:1, v/v)	No
Quantification Method	Metaboanalyst	Metaboanalyst	Metaboanalyst

The data was normalised over median values of all metabolites within each sample, log-transformed, and Pareto scaled by Metaboanalyst software.

4.11 ^{13}C tracing analysis

A2780S and A2780R cells were plated in 10cm dishes in 5 biological replicates per condition. After they were adhered, only the A2780R cells were treated with 10μM MS094 and/or MS023. After 24h of the treatment, cells were incubated with 1mM U-$^{13}C_5$]-Glutamine (cat.no. 605166, Sigma-Aldrich) or 0.4mM [U-$^{13}C_4$]-Serine (cat.no. TRC-S270999, Lgc Standards) for another 24h together with the inhibitor. One plate per condition was left without tracer, and the other plates were supplemented with ^{12}C-Glutamine or ^{12}C-Serine. Both media contained the rest of the components such as 10% FBS, 25mM glucose and 1mM pyruvate. Following incubation, metabolites were extracted and processed in the same manner as described in section 4.9.

For isotope tracing analysis, we used the same LC-MS setup and chromatographic conditions as described in the table. The only adjustment was at the MRM level, where transitions were adapted to include the expected mass shifts corresponding to ^{13}C-labeled isotopologues. Data were expressed as Mass Isotopomer Distribution (MID).

4.12 Enrichment of mitochondrial fraction and methyl-proteomics workflow

Heavy and light methionine-labelled HeLaS3 or SkOV3 cells were counted and mixed in a 1:1 ratio to reach 60 million cells. The pellet was washed once in ice-cold PBS and resuspended gently in cold hypotonic buffer (sucrose 100mM, MOPS 10mM, EGTA 1mM, NaCl 10mM, $MgCl_2$ 1.5mM and Tris-Cl (pH 7.4) 10mM) with freshly added EDTA-free protease inhibitor and 0.05% Triton-X and allowed to undergo osmotic swelling for 5 minutes on ice. Cells were homogenised manually

with a Potter Elvehjem homogeniser with 20 and 30 strokes for SkOV3 and HeLaS3 cells, respectively. 0.173xV of hypotonic buffer and 0.16xV of hypertonic buffer (sucrose 1.25M, MOPS 10mM, EGTA 1mM, Tris-Cl (pH 7.4) 5mM) were added to the homogenate to reach a final osmolarity of 250mOsm approximately. The homogenate was then centrifuged at 2000g twice (15min and 5min) to pellet the nuclei. The pellet was discarded after each centrifugation round. The supernatant after the second centrifugation was centrifuged again at 8000g for 10 minutes, and the supernatant (corresponding to the cytosolic fraction) was discarded. The pellet (corresponding to the mitochondrial fraction) was resuspended in ice-cold isolation buffer (mannitol 210mM, sucrose 70mM, EGTA 1mM, MOPS 10mM) and centrifuged at 12000g for 10 minutes. The pellet was washed again with isolation buffer, and one tenth (or 10%) was used for western blot analysis probing against mitochondrial, nuclear and cytosolic marker proteins. The remaining nine-tenths (or 90%) was used for the MS proteomics analysis to evaluate the relative abundance of mitochondrial proteins in the mitochondrial fraction compared to the whole cell extract.

4.13 Sample preparation for whole proteomic MS analysis

Label-free cell pellets were collected to quantify the total proteome in a minimum of 3 biological replicates, and samples were prepared using the iST kit (PreOmics – P.O.00027) using the manufacturer's protocol. The peptides were dried in a SpeedVac at 45°C, and the dried peptides were resuspended in LC-Load, which is also provided by the kit. A maximum of 500ng sample was injected per sample into the mass spectrometer. The same kit was used for the incorporation test.

4.14 Sample preparation for methylproteomics analysis

Mitochondrial fraction obtained from HeLaS3 or SkOV3 cells was lysed in a lysis buffer (9M urea, 20mM HEPES (pH 8) with 1X protease and phosphatase inhibitor) at room temperature. For the double SILAC experiment, heavy and light cells were mixed in a 1:1 ratio to yield 1mg of extract and processed without any kind of subcellular fractionation. Under the keratin-free hood, the lysed solution was reduced with $1/278^{th}$ volume of 1.25M DTT, 1h at room temperature while shaking and alkylated with $1/10^{th}$ volume of freshly prepared 1M iodoacetamide, 15mins in the dark at room temperature. Thereafter, the reduced and alkylated lysate was digested with 1/100 (w/w) MS-grade porcine trypsin overnight at 37°c on shaking. The next day, the digestion was stopped by adding $1/20^{th}$ volume of 20% TFA and pH was measured with a pH strip (pH<3) and allowed to form

precipitation (if any) by cooling for 15mins on ice. The digested peptides were cleared by centrifuging for 15 minutes at 4000g at room temperature, and the cleared supernatant (containing peptides) was purified using a C18 column. The purified peptides were snap-frozen with dry ice and lyophilised overnight in a lyophilzator at -50°c and ~15-20mBar. Antibodies conjugated with magnetic beads against symmetrically (PTMScan by CST, BK35985S) and/or asymmetrically dimethylated peptides (PTMScan by CST, BK13474S) were used in sequence to immunoprecipitate (IP, 3h at 4°C at a slow rotation) the methylated peptides from the lyophilised mitochondrial fractions using the manufacturer's protocol. The flow-through after the IP was used again as an input to IP mono-methylated peptides (PTMScan by CST, BK98567S). The beads were washed, eluted with 0.15% TFA in water and loaded onto stage tips containing C18 membrane pads for peptide desalting, concentration and (if needed) long-term storage. Prior to MS analysis, peptides were eluted in 0.1% formic acid in water and injected into a nano-LC-MS/MS instrument.

4.15 LC-MS/MS instrument method for proteomic analysis

The details of the methods used for different LC-MS/MS analyses are summarised below in Table 4.

Table 4: Acquisition methods for proteomics

Experiment	Instrument/ column	LC method	MS method
Total proteome (label-free)	Orbitrap Astral/ EasySpray pepmap column 15cm x 150µM (No FAIMS)	23 minutes with an increasing acetonitrile gradient (4%, 8%, 22.5%, 35%, 55% and 99%) at a flow rate ranging between 800nl-2µl/min	MS1 acquisition: Orbitrap resolution= 240000, Scan range (m/z) = 380-980, Injection time = 5ms, normalized AGC target = 500% MS2 acquisition = DIA, Isolation window (m/z) = 2Th, m/z window overlap = 0, HCD collision energy = 27%, scan range (m/z) = 100-1000, injection time = 3ms

Incorporation Of heavy Methionine for hmSILAC	Q-Exactive HF	60 minutes with an increasing acetonitrile gradient (5%, 20%, 30%, 65% and 95%) at a flow rate of 300nl/min	MS1 acquisition: Orbitrap resolution= 60,000, Scan range (m/z) = 375-1650, Injection time = 20ms MS2 acquisition = DDA, TopN = 12, HCD collision energy = 27%, AGC target = 1e5, scan range (m/z) = 200-2000, injection time = 90ms
hmSILAC	Q-Exactive HF	60 minutes with an increasing acetonitrile gradient (5%, 20%, 30%, 65% and 95%) at a flow rate of 300nl/min	MS1 acquisition: Orbitrap resolution= 60,000, Scan range (m/z) = 375-1550, Injection time = 20ms MS2 acquisition = DDA, TopN = 15, HCD collision energy = 27%, AGC target = 1e5, scan range (m/z) = 200-2000, injection time = 100ms

4.16 MS data analysis for hmSILAC samples for high confidence methyl-peptide identification

A. MaxQuant-hmSEEKER pipeline

In MaxQuant, peptide identifications were filtered to ensure a maximum false discovery rate (FDR) of 1%. The main search utilised a mass tolerance of 4.5 ppm, with enzyme specificity set to Trypsin/P. Up to three missed cleavages were allowed, and the minimum peptide length was set at six amino acids. Carbamidomethylation of cysteine was designated as a fixed modification. Peptide identification was conducted using the UniProt sequence database version from June 2020. To assign hmSILAC peptide sequences, new modifications were defined in MaxQuant for heavy mono-methylation (mono-methyl4-K/R) and di-methylation (di-methyl4-K/R), as well as heavy methionine (Met4) and oxidised heavy methionine (OxMet4). To simplify the analysis, raw data were processed in two separate runs with the following variable modifications: (1) N-terminal acetylation,

Met4, OxMet4, oxidation, mono-methyl-K/R, mono-methyl4-K/R; (2) N-terminal acetylation, Met4, OxMet4, oxidation, di-methyl-K/R, di-methyl4-K/R. High-confidence methylation sites were identified using the Python-based pipeline hmSEEKER. To enhance reliability, peptides with an Andromeda score below 25, an Andromeda delta score under 12, or a localisation probability below 0.75 were automatically excluded.

B. Fragpipe-MethylQuant pipeline:

First, the .raw files were converted to .mzml format using Proteowizard software, making them compatible with Fragpipe software. Two different searches were carried out with the same file, once with heavy modifications and once with light modifications. The variable modifications in heavy were set to the same as MaxQuant. To enhance the identification at 1% FDR, we used the percolator tool with default settings and the PTM localisation probabilities were computed using the PTMProphet tool, which is embedded inside Fragpipe. The raw output obtained from Fragpipe (for both heavy and light) was formatted with an in-house Python script to make it compatible with MethylQuant. Finally, the MethylQuant run was used to annotate high-confidence methylation sites that had a MethylQuant confidence of 'high' and 'very high'.

4.17 Statistical analysis

Independent experiments were considered biological replicates. For Mitostress tests, one experiment was shown as a representative with technical replicates, while the biological replicates (not shown) defined the same conclusion. Statistical analysis was performed with GraphPad Prism version 10.3.1 or with Microsoft Excel. Statistical significance was evaluated using Student's two-tailed t-test or One-way ANOVA, followed by Tukey's correction. The cut-off to define significance was set at p-value < 0.05. Asterisks correspond to the p-value calculated by a two-tailed unpaired t-test or by One-way ANOVA (*p-value < 0.05; **p-value < 0.01; ***p-value < 0.001; ****p-value < 0.0001). The type of statistical analysis performed and the significance values are reported in the Figure legends in the Results section.

5. Results

5.1 Validation of an *in-house* generated adaptive EOC model of chemoresistance

5.1.1 Generation of platinum-resistant cell lines to study adaptive chemoresistance

Building on the mechanism illustrated on a chemoresistant ovarian cancer cell line (SkOV3 cells), which captures the immediate cellular responses to platinum exposure (an acute response) (Musiani *et al.*, 2020), we next sought to establish an adaptive model to reflect the long-term, clinically relevant evolution of resistance. The preliminary data (**see figure 9**) provided insights into early stress signalling by cisplatin and potentially a short-term metabolic rewiring. We reasoned that a model of adaptive chemoresistance would enable us to study the progressive remodelling that occurs under sustained drug pressure. These complementary approaches would allow us to dissect both the rapid and gradual mechanisms by which ovarian cancer cells acquire chemoresistance. Hence, a colleague of mine in the Bonaldi's group (Michele Carminati, PhD student) generated an *in vitro* cell model of induced resistance.

Carboplatin (CBP) was chosen to induce chemoresistance because it is preferred to cisplatin for the treatment of gynaecological cancers, due to its similar anti-cancer efficacy but lower renal and gastrointestinal toxicity (Mansoor *et al.*, 2023). To generate resistant sub-lines, we adapted protocols commonly used in the literature for several cancer types (Sales Amaral *et al.*, 2019), including studies on OC cell lines (Sonego *et al.*, 2017; Kralj *et al.*, 2023). Following a workflow reported for other EOC cell lines (Bahar *et al.*, 2020), we treated parental A2780 cells with gradually increasing CBP concentrations over multiple cycles. Cells were first exposed to 5μM CBP in 72-hour treatments, each followed by 72 hours of recovery, repeated for 20 cycles. The dose was then raised to 10μM for another 20 cycles under the same schedule. Subsequent increases to 20μM and 40 μM yielded the first resistant sub-line (A2780-CBP1). At 40 μM, recovery periods were no longer required due to improved drug tolerance, and continuous 72-hour CBP treatments were applied. Further stepwise increases to 60μM and 80μM, without recovery intervals, generated a second, more resistant sub-line (A2780-CBP2). For this study, we used A2780-CBP2 clones, which are hereafter referred to as A2780R (**Figure 11A**).

A2780R cells displayed a distinct morphology characterised by a smaller size, a rounded shape, and a tendency to grow in clusters. Phalloidin staining of β-actin showed a reorganisation of the cytoskeleton (**Figure 11B**). In addition to their altered appearance, the resistant clones proliferated more slowly (**Figure 11C**) and, most notably, exhibited an 8.8-fold higher resistance to carboplatin than their sensitive counterparts, the A2780S cells (**Figure 11D**).

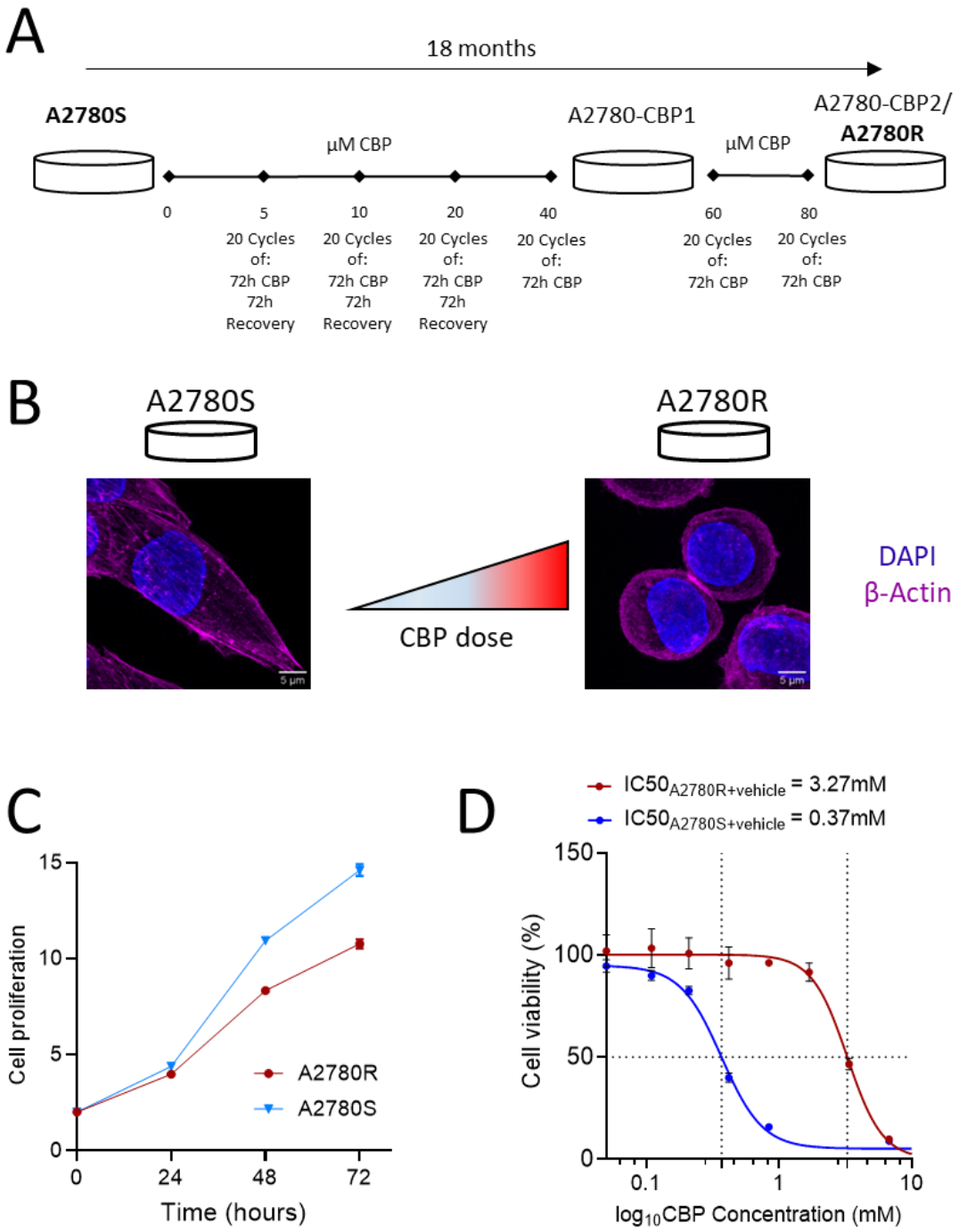

Figure 11: Generation of A2780R from A2780S and primary characterisation
(**A**) Scheme representing the protocol for the generation of CBP-resistant A2780R clones from A2780S cells. (**B**) Representative confocal microscopy images of A2780S and A2780R cells stained with DAPI (nuclei, blue) and β-actin (cytoskeleton, magenta). A2780R cells show a more rounded morphology compared to the elongated A2780S cells. Scale bar: 5µm. (**C**) Growth curve of A2780S and A2780R cells measured over 96 hours. A2780R cells proliferate more slowly compared to A2780S. (**D**) Dose–response curves of A2780S and A2780R cells treated with Carboplatin. A2780R cells demonstrate higher resistance, indicated by the rightward shift in IC50 values. Data are presented as mean ± SD from at least three independent biological replicates (n=3).

5.1.2 A2780R shows a higher oxygen consumption rate than A2780S

As discussed in the introduction, bioenergetic studies of ovarian cancer cells reveal distinct metabolic profiles between chemosensitive and chemoresistant phenotypes. While chemosensitive cells (e.g., A2780) showed a greater dependence on glycolysis, their chemoresistant counterparts (C200) exhibited higher oxidative phosphorylation (OXPHOS) activity (Dar *et al.*, 2017). In light of these published results, we questioned whether our in-house-generated A2780-resistant cell line (A2780R) also displays a phenotype similar to the C200 cells and could serve as a suitable model to test our hypothesis for this study.

To test whether mitochondrial activity was affected during the development of resistance in A2780S cells, we performed a Mitostress stress assay. This assay measures oxygen consumption rate (OCR) and extracellular acidification rate (ECAR) using optical-fluorescent oxygen probes and pH-sensitive fluorescent probes, respectively. A sensor cartridge creates an approximately 2µl micro-chamber when placed onto the live-cell monolayer during the assay. The fluorescent probes inside the chamber change their signals based on O_2 and H^+ concentrations. The micro-chamber's small volume and sealed environment enhance the signals, enabling precise real-time measurement of metabolic changes. OCR directly indicates oxidative phosphorylation, while ECAR indirectly reflects glycolytic activity, measured from the proton concentration derived from lactic acid. OCR and ECAR together depict the overall metabolic/energetic state of the cell. The first parameter measured in the Mitostress test is basal respiration. In the first injection port, oligomycin—an ATP synthase inhibitor—is used, which causes a sharp decline in the OCR level and indicates ATP synthase-linked respiration (ATP production). Next, FCCP, a well-known mitochondrial membrane uncoupler, is applied, allowing the cells to respire at their maximum capacity. In the final injection, a complete shutdown of the electron transport chain is achieved by combining Rotenone and Antimycin A, which are complex I and III inhibitors. The parameter spare respiratory capacity indicates the difference between maximal and basal respiration (**Figure 12A**).

First, we compared the overall energy states between A2780S and A2780R cells by comparing ECAR and OCR values. A2780S cells were located in the bottom right quadrant of the energy map, depicting a more substantial reliance on glycolysis. In contrast, the A2780R cells shift to the top right quadrant, highlighting a higher dependence on oxidative phosphorylation along with glycolysis (**Figure 12B**). In the Mitostress test plot, we could appreciate that the overall mitochondrial respiration was much higher in the resistance-induced A2780 cells compared to their sensitive counterparts (**Figure 12C**). This observation aligned with the findings highlighted by Dar *et al.*, 2017 earlier. Further quantification of individual parameters, such as basal respiration, ATP production, and maximal respiration and spare respiratory capacity, indicated that A2780R

cells have adapted to exhibit significantly higher mitochondrial activity (**Figure 12D**) and rely more on oxidative phosphorylation compared to A2780S cells for energy production.

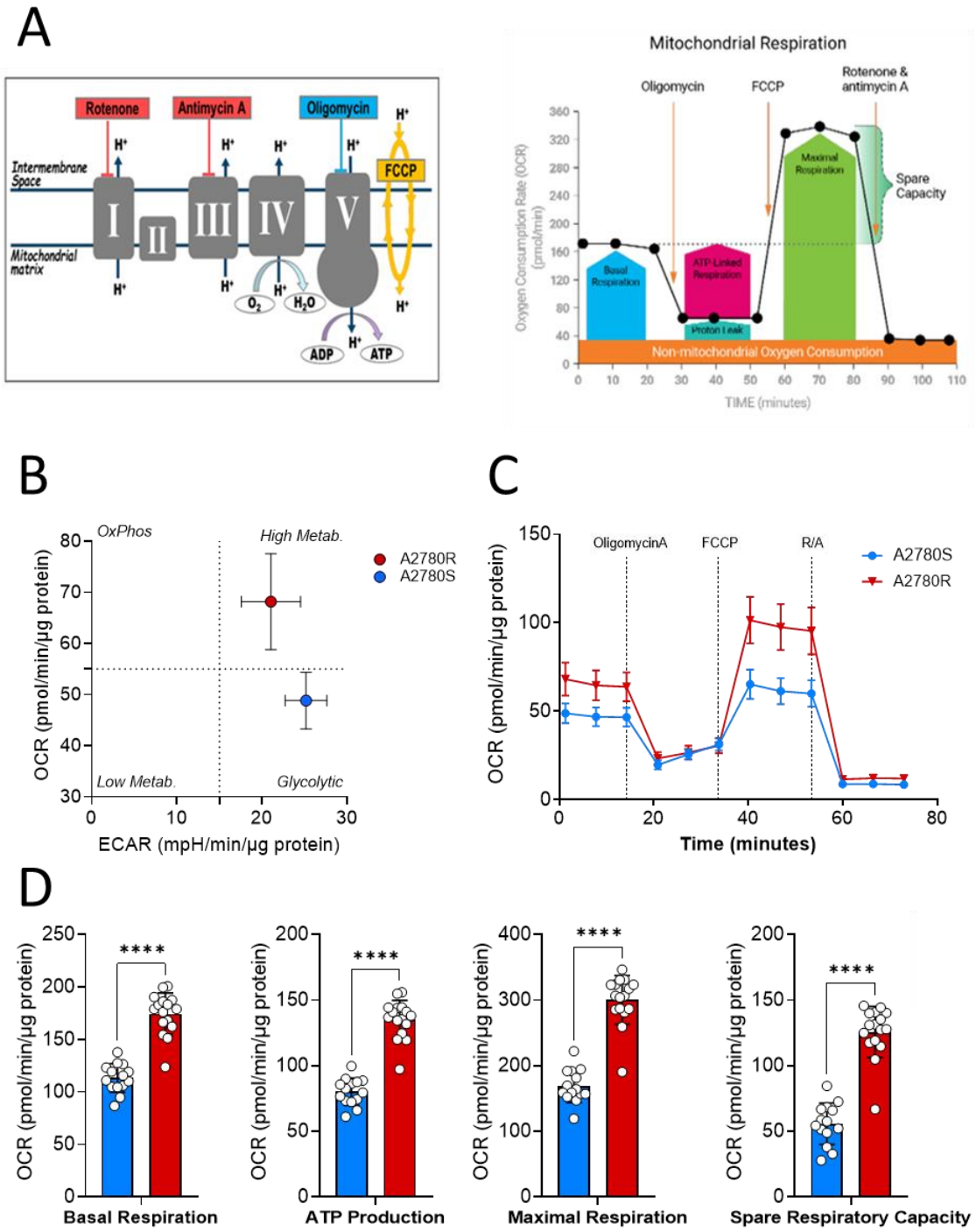

Figure 12: Mitrostress test principle and profile of A2780S and A2780R
A: Mitostress test principle and test profile (taken from Agilent website). **B-D:** Measurement of mitochondrial oxygen consumption rate (OCR) with Seahorse mitostress test in A2780S and A2780R cells. Oligomycin, FCCP, and rotenone/antimycin A were sequentially injected, and oxygen consumption rate (OCR) values were normalised to total protein content. Bar graphs show a representative experiment from three independent biological replicates; individual points indicate technical replicates. Data are presented as mean ± SD, with significance determined by Student's *t*-test (**** < 0.0001, *** < 0.001, ** < 0.01, * < 0.05).

5.1.3 A2780R cells display mitochondrial fusion and enhanced mitochondrial volume

Mitochondria are dynamic organelles that undergo fusion and fission processes to cope with cellular demands against stressed conditions (Kingnate *et al.*, 2018). Fission generates fragmented mitochondria, which can undergo mitophagy to maintain a healthy pool of mitochondria inside the cells, support cell proliferation under nutrient excess and generate ROS. : In contrast, fusion generates an elongated, tubular, hyperfused mitochondrial network that facilitates the sharing of matrix proteins among interconnected mitochondria, thereby reducing the local burden of mtDNA mutations and oxidized proteins (Archer, 2013; Wai and Langer, 2016). Indeed, increased fusion of mitochondria has been previously reported in chemoresistant ovarian cancer (A2780cp-resistant to cisplatin) cells compared to their sensitive counterparts (A2780-sensitive to cisplatin) (Kong *et al.*, 2022).

We examined mitochondrial fusion and fission dynamics and tagged the mitochondrial outer membrane protein 25 (OMP25) with GFP in our A2780S and A2780R cells, following a previously described method (Chen *et al.*, 2016). The GFP-labelled mitochondria were visualised using a confocal microscope under basal conditions. Skeleton analysis revealed that mitochondrial volume is significantly larger in A2780R than in A2780S cells, and the organelles within the network appeared more elongated (reduced sphericity). They also exhibited greater branch length and a higher number of branches and junctions in A2780R cells (**Figure 13**), indicating a more fused mitochondrial network, in line with the findings of Kong *et al.*, 2022. As demonstrated by this analysis, A2780 cells acquire resistance to CBP through continuous and dynamic remodelling of their mitochondrial network, as part of an adaptive process to cope with therapeutic pressure.

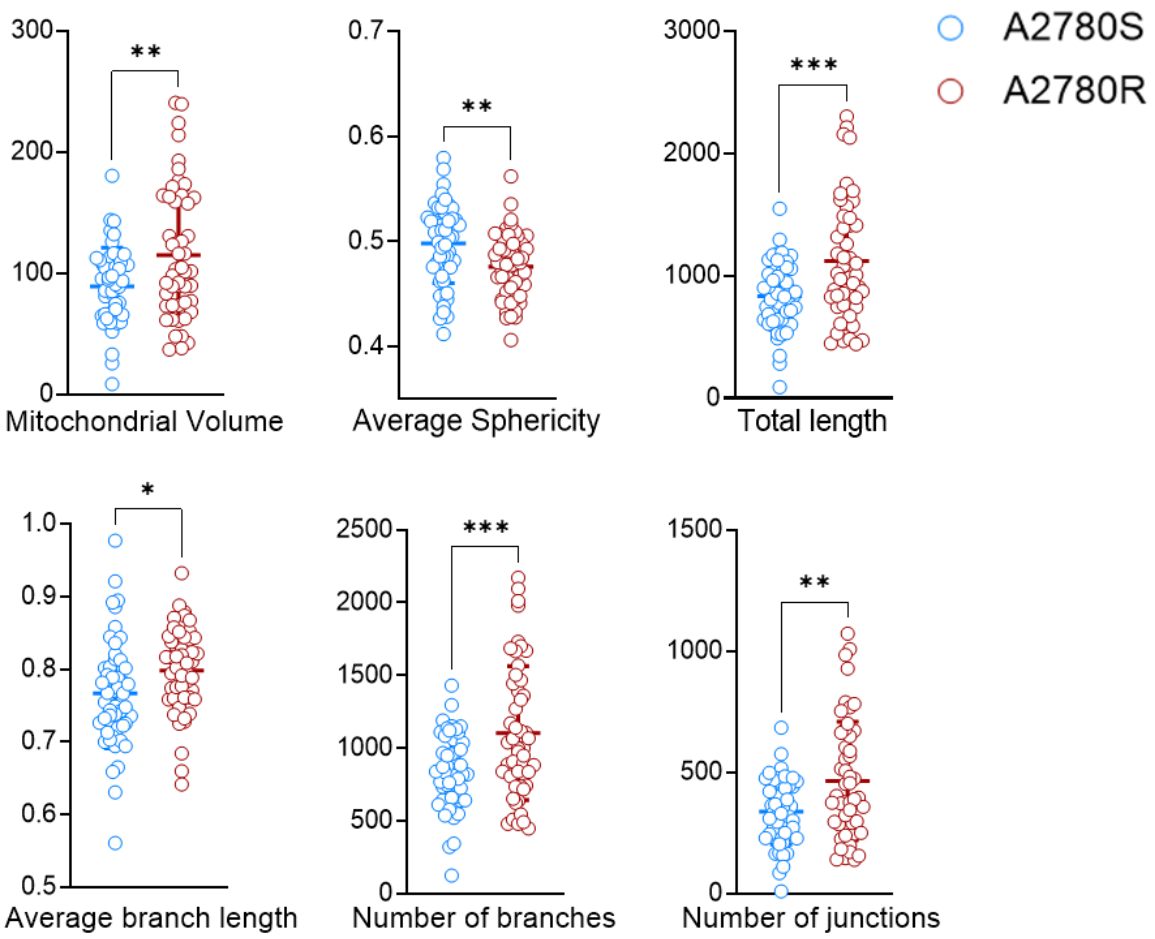

Figure 13: Quantitative analysis of mitochondrial architecture in A2780S and A2780R cells using skeleton-based image analysis

Parameters analysed include mitochondrial volume, sphericity, total branch length, average branch length, number of branches, and junctions in A2780S and A2780R cells in basal conditions. Graphs represent mean ± SD, and statistical significance obtained by paired t-test is indicated as *p<0.05, **p<0.01, ***p<0.001, and ns = not significant (n=50).

5.1.4 Pharmacological inhibition of Type-I PRMTs sensitises A2780R cells against CBP

Having established a model of acquired chemoresistance in ovarian cancer cells, we sought to determine whether pharmacological inhibition of PRMTs could also re-sensitise the resistance-induced A2780R cells, similar to what was shown by Musiani *et al.*, 2020 in SkOV3 cells. Hence, we decided to pharmacologically modulate global protein ADMA levels with the chemical compound MS023, a broad PRMT Type-I inhibitor (Eram *et al.*, 2015), using MS094, its inactive analogue, as a negative control, using the same experimental protocol described in (Musiani *et al.*, 2020). Indeed, MS023 pre-treatment significantly reduced the CBP IC_{50} of cisplatin in A2780R cells, indicating increased sensitivity to the drug, also when the resistance phenotype results from a long-term adaptation. A 48h pre-treatment with MS023 alone, followed by 24h CBP treatment,

could decrease the IC50 of these cells from 3.27mM to 1.44mM, marking a drop by 56% (**Figure 14A**). While a pre-treatment of 24h MS023 alone, followed by a co-treatment of CBP and MS023 for 24h, decreased the IC50 of A2780R cells to 2.48mM, marking a drop by 24% (**Figure 14B**). This data led us to conclude that inhibition of type-I PRMTs alone for 48h primes the cells to respond better to CBP treatment. Therefore, we set out to focus on the mitochondrial metabolic and functional rewiring at this time point.

We investigated whether the CBP-sensitive A2780S and CBP-resistant A2780R ovarian cancer cell lines show differences in overall protein R-methylation at basal conditions. Western blot analyses were carried out using pan-specific antibodies against asymmetrically dimethylated arginine (ADMA) and monomethylated arginine (MMA). At baseline, both cell lines displayed similar protein ADMA and MMA profiles, with no pronounced differences in overall signal intensity. Treatment with the type I PRMT inhibitor MS023 led to a marked reduction in global ADMA levels in both A2780S and A2780R cells. Conversely, the structurally similar but inactive analogue MS094 had no noticeable effect. Interestingly, treatment with MS023 resulted in a concomitant increase in MMA levels in both sensitive and resistant cell lines, although the patterns of MMA accumulation varied between them, indicating that the drug affects the methylation state of the proteome of the two cell lines slightly differently, possibly with the modulation of different substrates (**Figure 14C**).

Consistent with previously reported MS023-induced phenotypes (Eram *et al.*, 2015), 48h of exposure to MS023 did not change the cellular morphology (**Figure 14D).** Until 24h, we did not observe any changes, but at 48h, MS023 slightly but significantly reduced cell proliferation in A2780R cultures (**Figure 14E-F)**. Nevertheless, the effect of MS094 was similar to that of the vehicle in cell proliferation.

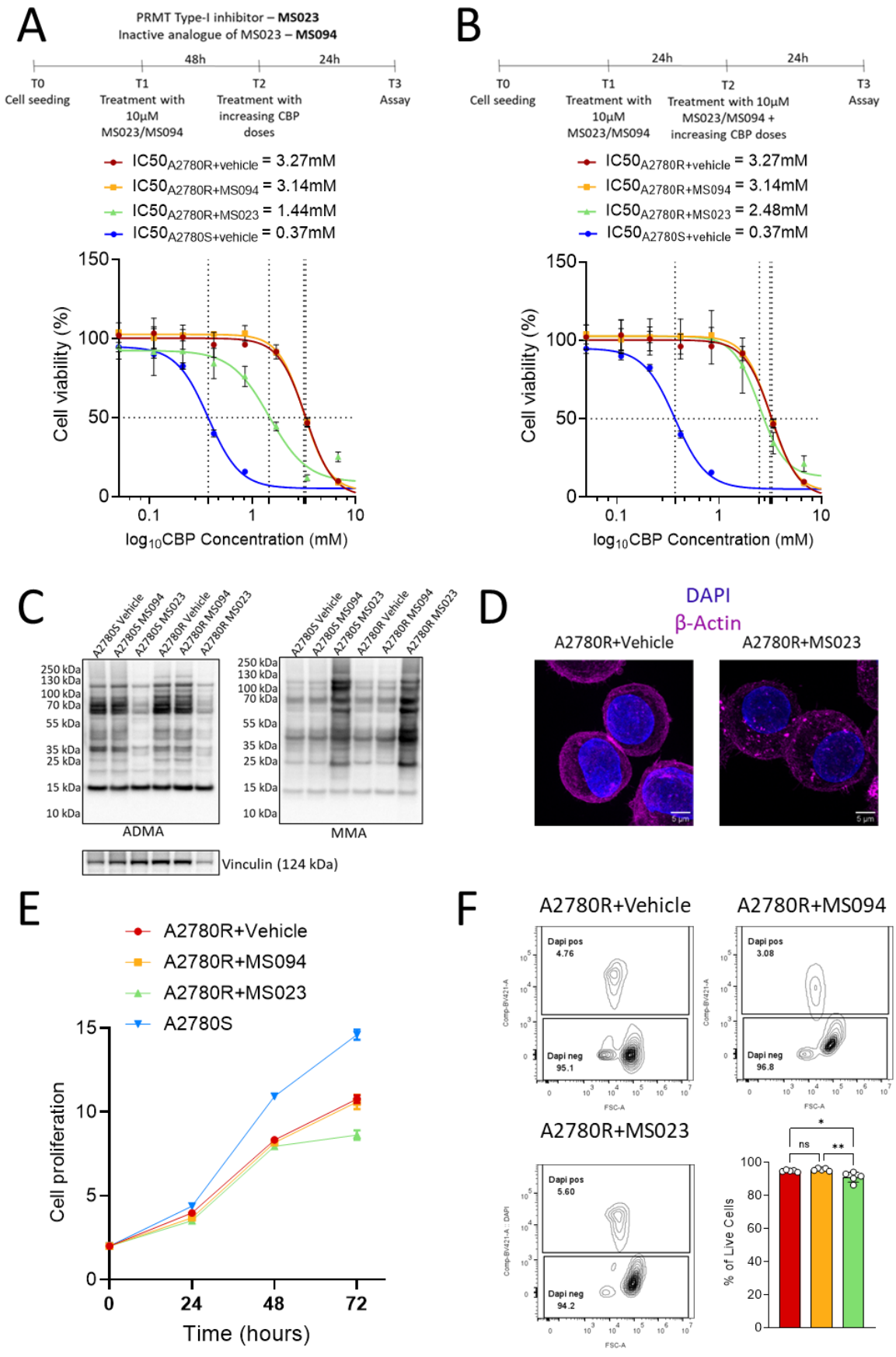
A
PRMT Type-I inhibitor – MS023
Inactive analogue of MS023 – MS094
48h
24h
T0
Cell seeding
T1
Treatment with 10µM MS023/MS094
T2
Treatment with increasing CBP doses
T3
Assay
IC50A2780R+vehicle = 3.27mM
IC50A2780R+MS094 = 3.14mM
IC50A2780R+MS023 = 1.44mM
IC50A2780S+vehicle = 0.37mM
Cell viability (%)
log10CBP Concentration (mM)
B
24h
24h
T0
Cell seeding
T1
Treatment with 10µM MS023/MS094
T2
Treatment with 10µM MS023/MS094 + increasing CBP doses
T3
Assay
IC50A2780R+vehicle = 3.27mM
IC50A2780R+MS094 = 3.14mM
IC50A2780R+MS023 = 2.48mM
IC50A2780S+vehicle = 0.37mM
Cell viability (%)
log10CBP Concentration (mM)
C
A2780S Vehicle
A2780S MS094
A2780S MS023
A2780R Vehicle
A2780R MS094
A2780R MS023
250 kDa
130 kDa
100 kDa
70 kDa
55 kDa
35 kDa
25 kDa
15 kDa
10 kDa
ADMA
MMA
Vinculin (124 kDa)
D
DAPI
β-Actin
A2780R+Vehicle
A2780R+MS023
E
A2780R+Vehicle
A2780R+MS094
A2780R+MS023
A2780S
Cell proliferation
Time (hours)
F
A2780R+Vehicle
A2780R+MS094
A2780R+MS023
Dapi pos
4.76
Dapi neg
95.1
Dapi pos
3.08
Dapi neg
96.8
Dapi pos
5.60
Dapi neg
94.2
FSC-A
ns
**
% of Live Cells

Figure 14: Effect of MS023, a Type-I PRMT inhibitor, on IC50, morphology, cell growth of A2780R cells

(**A-B**) Treatment scheme of MS023 and dose–response curves of A2780R cells against CBP pre-treated with vehicle, MS094 and MS023. MS023-treated A2780R cells demonstrate lower resistance, indicated by the leftward shift in IC50 values. Data are presented as mean ± SD from three independent biological replicates. (**C**) 48h of treatment with 10μM of MS023 reduces global ADMA and increases MMA levels (after stripping) on a whole protein extract, whereas MS094 does not impact global R-methylation levels. Vinculin was used as a loading control for both (**D**) Representative confocal microscopy images of A2780R and MS023-treated A2780R cells stained with DAPI (nuclei, blue) and β-actin (cytoskeleton, magenta). MS023-treated A2780R cells show disorganisation of the cytoskeleton compared to vehicle-treated ones. Scale bar: 5μm. (**E**) Growth curve of A2780S and vehicle, MS094 and MS023-treated A2780R cells measured over 96 hours. MS023-treated A2780R cells proliferate more slowly compared to vehicle/MS094-treated cells. (**F**) flow cytometry analysis of DAPI-staining in vehicle, MS094 and MS023-treated cells. MS023 treatment shows a mild yet significant reduction in live-cell population. Bar graphs represent mean ± SD, and one-way ANOVA was used to perform statistics where **=<0.01 and *=<0.05 (n=5).

5.2 Mechanistic investigation of the effect of Type-I PRMT inhibition on mitochondrial function in A2780 cells

In the adaptive resistance model A2780R, we have also observed an elevated mitochondrial activity (**see Figure 12**) and a fused mitochondrial network (**see Figure 13**) at the basal level. Therefore, we asked if the reduction of IC50 value we observed in A2780R upon MS023 pretreatment (**see Figure 14A**) could be due to loss of mitochondrial functions. Hence, we set out to undertake assays designed to verify the existence of a link between the enzymatic activity of Type-I PRMTs and mitochondrial functionality, an aspect not yet addressed systematically.

5.2.1 Pharmacological inhibition of Type-I PRMTs lowers mitochondrial respiration significantly

First, we evaluated the impact of inhibiting PRMT Type-I on mitochondrial respiration in A2780R cells and performed the Seahorse Mitostress test (**described in Results 5.1.2**) upon pharmacological intervention with MS023. This experiment showed that the treatment with MS023-treated A2780R cells had comparable energy states to A2780S cells, while the inactive compound MS094 did not alter OCR levels (**Figure 15A**). In all the measured parameters of mitochondrial respiration, except for ATP production, we observed a restoration of mitochondrial activity with MS023 treatment (**Figure 15A**). This data seems to strengthen our hypothesis that MS023 sensitises A2780R cells to CBP by blunting their enhanced mitochondrial activity. Interestingly, MS023 also lowered OCR levels in A2780S cells, suggesting that R-methylation is

essential for mitochondrial activity in EOC cells overall (**Figure 15B**), and this effect is not limited to chemoresistant cell types.

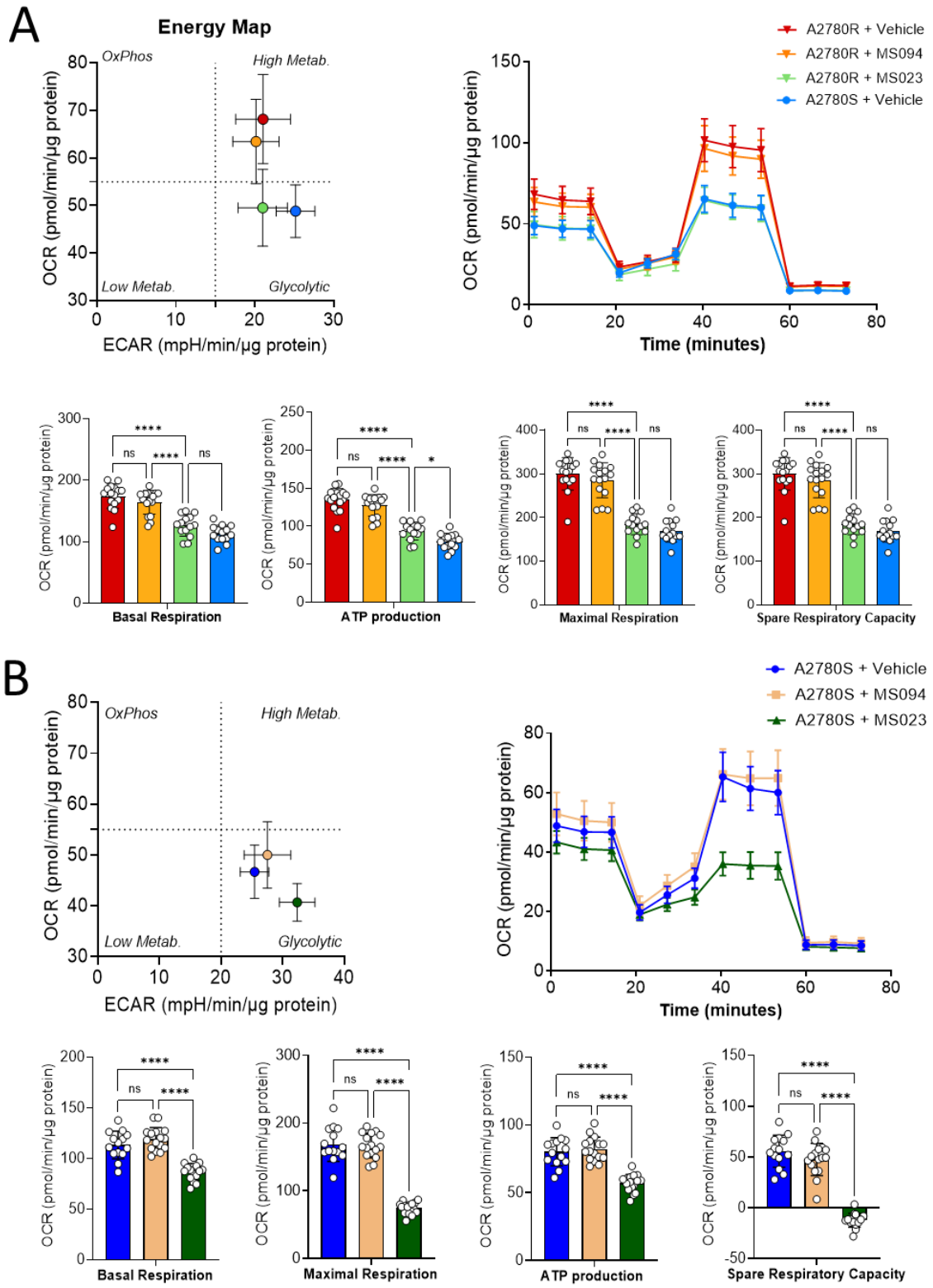

Figure 15: Measurement of mitochondrial OCR by mitostress test at basal state and upon type I PRMT inhibition in A2780R (A) and A2780S (B) cells

Seahorse Mitostress test performed using oligomycin, FCCP and rotenone/antimycin A, respectively, in injection ports and the raw OCR levels were normalised over the total protein amount estimated (n=3). Bar graphs represent mean ± SD and one-way ANOVA was used to perform statistics where ****=<0.0001, ***=<0.001, **=<0.01 and *=<0.05.

5.2.2 MS023 reduces mitochondrial volume and disrupts the mitochondrial network in A2780R cells

The reduction of mitochondrial respiration could be explained by either a reduction in mitochondrial number or a disruption of the mitochondrial network. To determine whether MS023-mediated dampening of the heightened mitochondrial activity observed in A2780R was due to a reduction in mitochondrial number, we measured the total mitochondrial DNA (mtDNA) content using real-time qPCR. Despite an overall variability across replicates, no differences were observed between A2780S and A2780R at the basal level. Additionally, MS023 did not seem to alter the copy number of mtDNA in A2780R (**Figure 16**).

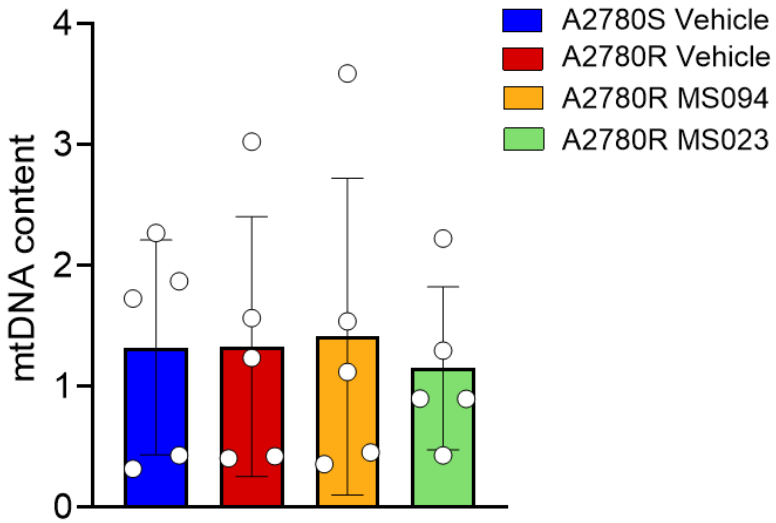

Figure 16: Quantitative analysis of mitochondrial DNA content by quantitative real-time PCR
10ng DNA per sample was amplified by qPCR using Taqman probes and primer pairs for COXII (mtDNA). The raw values normalised over 36B4 (nuclear) genes. The expression levels were calculated using the following formula: expression = $2^{(-\Delta\Delta Ct)}$. Data are presented as mean ± SD. (n=5)

Next, we assessed whether MS023 dampens mitochondrial OCR by impacting the fused network of A2780R cells. To examine the fusion-fission dynamics and the overall arrangement of the mitochondrial network upon Type-I PRMT inhibition, we again used GFP-OMP25-tagged A2780S and A2780R cells (**Figure 17**) in both basal and MS023-treated conditions. The GFP-labelled mitochondria in A2780R cells under vehicle and MS023-treated conditions and vehicle-

treated A2780S were visualised using a confocal microscope. Images were acquired in z-stacks while manually defining the top and bottom for each cell, and the mitochondrial 3D-skeleton was constructed using Fiji algorithms and in-house scripts.

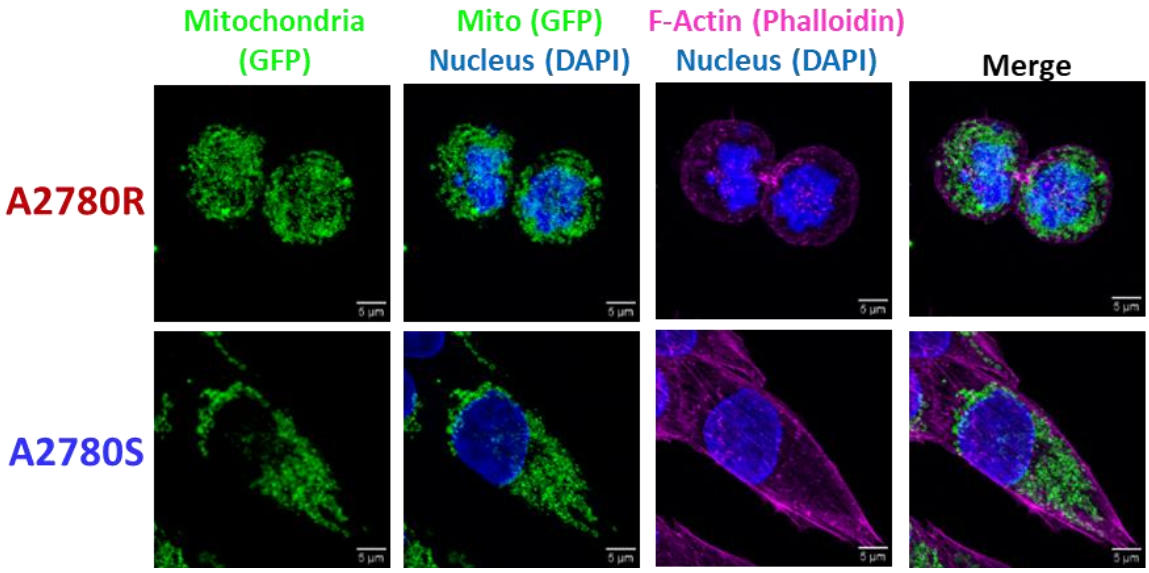

Figure 17: Representative images of GFP-tagged mitochondria
Mitochondria of A2780R (top panel) and A2780S (bottom panel) were visualised with a 100X oil objective in a spinning disk confocal microscope using GFP (green), nuclei were stained with DAPI (blue), and F-actin was labelled with Phalloidin (magenta). Scale bar = 5µm

The skeleton analysis revealed that mitochondrial volume is significantly larger in A2780R than in A2780S cells, and that the organelles within the network display a more elongated morphology, with decreased sphericity. The total length of the network was also found to be increased in A2780R cells, consistent with the higher volume. MS023 reduced mitochondrial volume and the network's total length to levels typical of A2780S cells **(Figure 18)**. Although MS023 did not influence the sphericity of individual mitochondria, it markedly decreased the mitochondrial branch diameters. Furthermore, increased branch length and the number of junctions that were observed in A2780R cells compared to A2780S cells, indicating a more fused mitochondrial network, were reversed by MS023 treatment **(Figure 18)**. This analysis suggests that CBP-sensitivity observed following MS023 treatment results from reduced mitochondrial volume and disrupted mitochondrial network integrity.

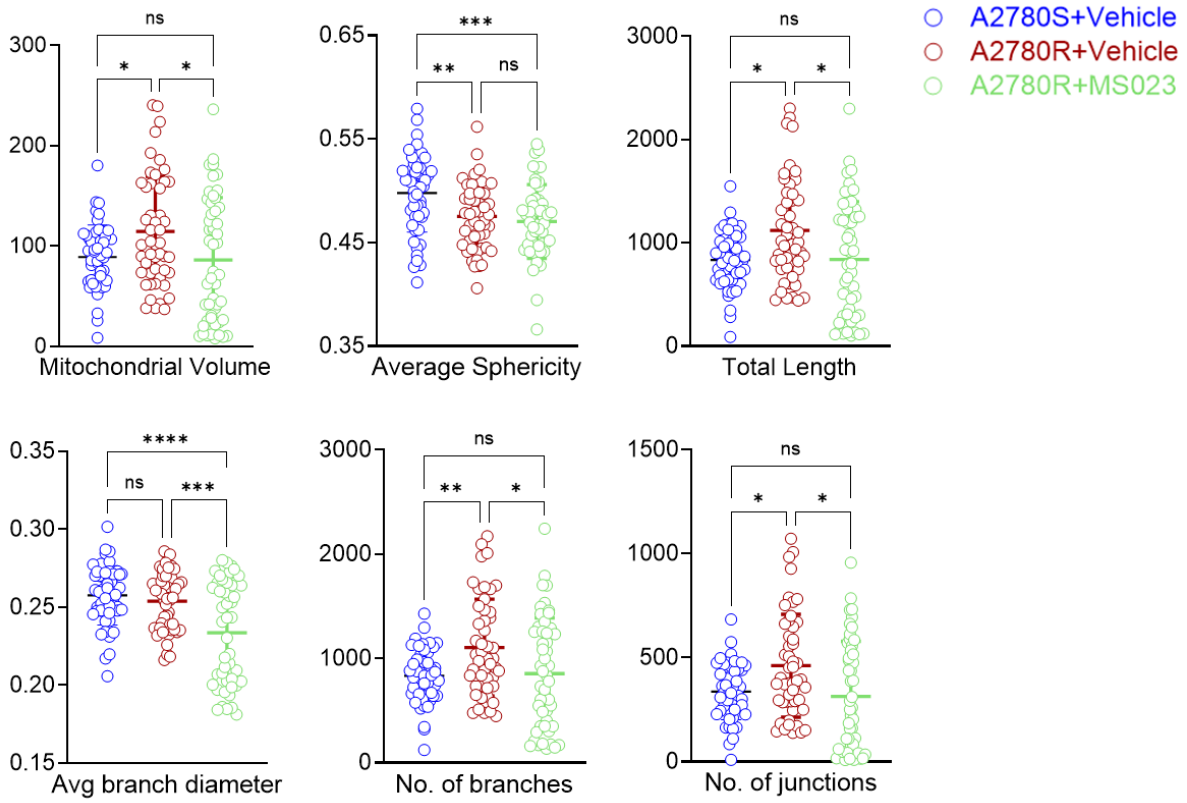

Figure 18: Quantitative analysis of mitochondrial architecture using skeleton-based image analysis

Parameters analysed included mitochondrial volume, sphericity, total branch length, branch diameter, number of branches, and junctions in A2780S and A2780R cells in untreated and MS023-treated conditions. Graphs represent mean ± SD, and statistical significance obtained by one-way ANOVA test is indicated as *p<0.05, **p<0.01, ***p<0.001, and ns = not significant (n=50).

5.2.3 Pharmacological inhibition of Type-I PRMTs lowers mitochondrial membrane potential in A2780R cells

Chemoresistant cancer cells often show hyperpolarisation of the mitochondrial membrane by maintaining a higher proton gradient across the inner and outer membranes (membrane potential; ΔΨ). An increased membrane potential helps to preserve mitochondrial integrity against reactive oxygen species (ROS) –mediated damage and boosts antioxidant and ATP production.

Therefore, we assess the membrane potential in A2780R cells, using JC1 dye via flow cytometry analysis at basal conditions and upon MS023. This mitochondrial membrane-specific lipophilic dye shifts fluorescence from green (~529 nm) to red (~590 nm) as it forms J-aggregates in a voltage-dependent manner. A decrease in the red/green ratio indicates mitochondrial membrane depolarisation [26]. For instance, classical mitochondrial uncouplers such as FCCP or CCCP decrease the membrane potential and were used as positive controls in the experiment.

At the basal level, A2780R exhibited a higher JC1 red/green ratio than A2780S cells, indicating a hyperpolarised mitochondrial membrane, consistent with the OCR levels and fused mitochondrial network. MS023 treatment significantly decreased the membrane potential compared to both MS094 and vehicle conditions. In fact, the reduction in membrane potential was found to be slightly but significantly lower than that of A2780S cells (**Figure 19A**). This result corroborates our hypothesis that the sensitising effect of MS023 is because Type-I PRMTs regulate mitochondrial function. Interestingly, depolarisation was also observed in A2780S (**Figure 19B**), supporting the idea that protein-R-methylation might be a biological process more generally essential for mitochondrial activity in EOC cells (**Figure 19**).

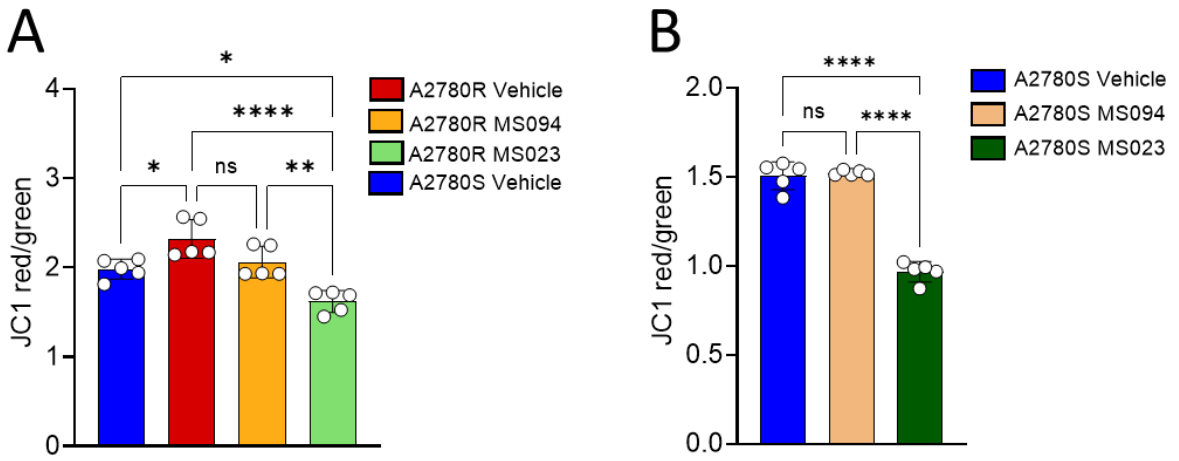

Figure 19: Quantifying mitochondrial membrane potential using JC-1 dye in A2780S and A2780R cells at both the basal state and upon MS023 treatment
The ratio of JC-1 aggregates to monomers (red/green) indicates mitochondrial polarisation. Statistical significance from paired t-test is denoted as **p<0.01 and ****p<0.0001. Data are presented as mean ± SD. (n=5)

5.2.4 Inhibition of PRMT Type-I induces mitophagy in A2780R cells

The integrative analysis of proteomics and metabolomics indicated that MS023 affects the central carbon metabolism and potentially induces mitochondrial dysfunction (**see results 5.2.5**). MS023 has also been shown to reduce mitochondrial respiration in A2780R cells by impairing functional adaptations, specifically decreasing the mitochondrial membrane potential and disrupting the network of these organelles. We hypothesised that the fate of these dysfunctional mitochondria is being removed through mitophagic clearance.

To assess this hypothesis, we used a commercially available construct from Addgene called mt-mKEIMA (*see Materials and Methods*). This construct is designed to label the mitochondrial Cytochrome Oxidase C subunit 8 (COX8) of the electron transport chain with a coral-derived

fluorescent protein named KEIMA. KEIMA is a pH-stable protein that appears green at neutral pH, but at lower pH levels- such as when fused with a lysosome- it undergoes a significant Stokes shift and emits red fluorescence, which can be quantified by flow cytometry analysis. The red to green fluorescence ratio indicates the proportion (if any) of the mitochondrial population undergoing mitophagy. A2780R cells stably expressing mt-mkeima were established and then treated with vehicle, MS094, and MS023 as previously described. In the assay, CCCP was used as a positive control. Additionally, Bafilomycin A, an autophagosome inhibitor, was utilised to confirm whether the observed changes in the red-to-green ratio are due to autophagosome formation. With flow cytometry analysis, we observed the expected green to red fluorescence shift of mt-mKEIMA in CCCP-treated A2780R, and noted a decrease in this ratio following Bafilomycin A treatment. These controls validated the system's proper function. Additionally, consistent with our hypothesis, a significant Stokes shift in mt-mKEIMA was detected in MS023-treated cells, whereas MS094 and vehicle-treated cells showed no change. Bafilomycin A treatment again reduced the mitophagic cell population in MS023-treated A2780R, further validating that the colour shift detected was due to autophagosome formation during mitophagy (**Figure 20A**).

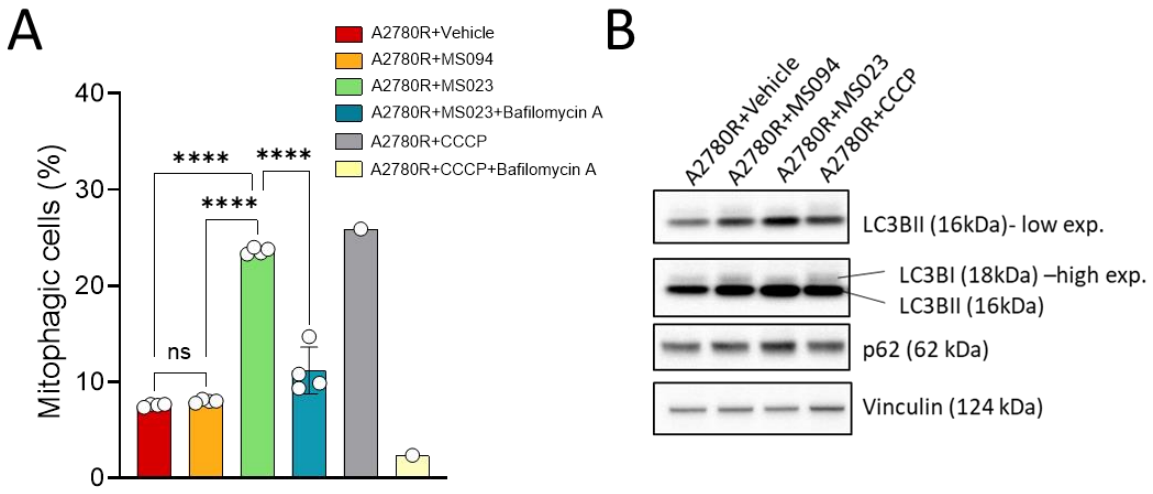

Figure 20: Quantification of mitophagy with MS023 treatment in A2780R cells
(**A**)**:** Flow cytometry analysis of mitophagic cell population. The red-to-green fluorescence ratio of mt-mKEIMA depicting the mitophagic cell population in vehicle, MS094 and MS023-treated A2780R cells, respectively (n=4), with CCCP (n=1) used as a positive control. As an autophagosome inhibitor, the Bafilomycin A treatment was applied in MS023 (n=4) and CCCP-treated (n=1) cells. Data are presented as mean ± SD. One-way ANOVA was used for statistical analysis, where **** <0.0001. (**B**)**:** Western blot analysis of autophagy markers LC3BI (18kDa), LCBII (16kDa), and p62 (62kDa) in A2780R cells. Vinculin (124kDa) served as a housekeeping protein (n=1)

To validate the molecular basis of this observation, we also examined LC3BI, LC3BII, and p62 levels under these conditions. To form a phagophore, cytosolic LC3BI is converted into its lipidated form, LC3BII. Autophagosomes coated with LC3II are recognised by p62, an autophagy receptor, and targeted for lysosomal degradation. Once properly fused with the lysosome, p62 is degraded along with its cargo inside. We observed an increase in LC3BII in CCCP-treated positive controls. Notably, LC3BI was absent in A2780R cells, but LCBII levels were increased upon MS023 treatment. The levels of p62 were contrasting to our expectation in A2780R cells – marking an increase in A2780R (**Figure 20B**), suggesting a lysosomal defect or autophagic bottleneck. Overall, the flow cytometry analysis and Western blots suggested that MS023 induces mitophagy in A2780R cells (**Figure 20**). The absence of LC3BI, along with an observable basal level mitophagy flux in A2780R cells, indicates that these cells are possibly using mitophagy to eliminate ROS-damaged mitochondria as a survival strategy. We could therefore conclude that MS023 lowers mitochondrial function, topples the delicate balance of biogenesis and degradation of the mitochondrial population, and this might contribute to the sensitisation of A2780R cells against CBP.

5.3. Proteomic and metabolomic characterisation of EOC cells highlights that Type-I PRMTs modulate the 1C metabolism

So far, we elucidated that pharmacological inhibition of Type-I PRMTs sensitises A2780R cells by blunting the enhanced mitochondrial function they acquired while withstanding CBP doses. Next, we wanted to understand the molecular basis of this acquired resistance in the A2780R cell line and whether MS023 impacts any adaptation nodes in these model systems. Therefore, we conducted an integrative proteomic and metabolomic analysis of the A2780R and A2780S ovarian cancer cell lines at the basal level and upon pharmacological inhibition of Type-I PRMTs. On one hand, untargeted proteomic profiling enabled the identification of differentially expressed proteins that played a role as A2780S acquired resistance against carboplatin, while on the other, targeted metabolomics detected altered metabolic pathways that were key to driving this process. In particular, integrating these complementary datasets allowed us to understand how protein-level alterations lead to metabolic rewiring associated with adaptive resistance. The multi-omic approach was designed to test the hypothesis that the role of PRMTs is mechanistically linked to the plasticity of mitochondrial metabolism in driving platinum-resistance in EOC. Through this set of experiments, we sought to determine whether PRMT-mediated post-translational

modifications drive mitochondrial metabolic reprogramming and thus support the chemoresistant phenotype.

5.3.1 Proteomic characterisation of A2780R cells highlights adaptation involving mitochondria

We first acquired the total proteome of A2780R and A2780S cells: whole cell extracts from label-free cells were digested with trypsin (in-solution), and purified peptides were subjected to LC-MS/MS analysis. The raw data were acquired using data-independent acquisition (DIA, see introduction) with an m/z isolation window of 2Da. On average, across biological replicates, we identified a depth of 8000 proteins on average with DIANN 2.0 (Demichev *et al.*, 2020) analysis employing an *in-silico* spectral library (**Figure 21A**).

Proteomic analysis identified 2502 differentially regulated proteins between A2780R and A2780S cells (>30%), of which 1363 (~17%) were upregulated and 1139 (~14%) were downregulated. Notably, among the differentially expressed proteins, we observed that 420 mitochondrial proteins were significantly modulated (FDR<0.05). Among the upregulated proteins, subunits of the electron transport chain, glutamine metabolism (GLS), mtDNA transcription factor (TFAM), mitochondrial fusion protein (MFN1) and ROS-scavenging enzyme (SOD1) appeared. Among the downregulated ones, we found the rate-limiting enzyme of fatty acid β-oxidation (CPT1A), enzymes involved in the fatty acid synthesis (ACAD11, FASN, MCAT) (**Figure 21B**). Specifically, upregulation of ETC complexes and of MFN1 corroborated our previous observation that A2780R has adapted to higher mitochondrial respiration/activity and a hyperfused mitochondrial network compared to A2780S (**Results 5.1.2 and 5.1.3**).

Interestingly, a gene ontology analysis of the differentially expressed proteins in A2780R compared to the sensitive cells prominently highlighted nucleotide metabolism and ribose phosphate metabolism among regulated biological processes (**Figure 21C**). Simultaneously, among cellular components, we observed terms majorly related to the mitochondrial electron transport chain and mitochondrial matrix (**Figure 21D**). This analysis further confirmed that mitochondria and metabolic reprogramming have played a significant role in sustaining CBP resistance in A2780R cells.

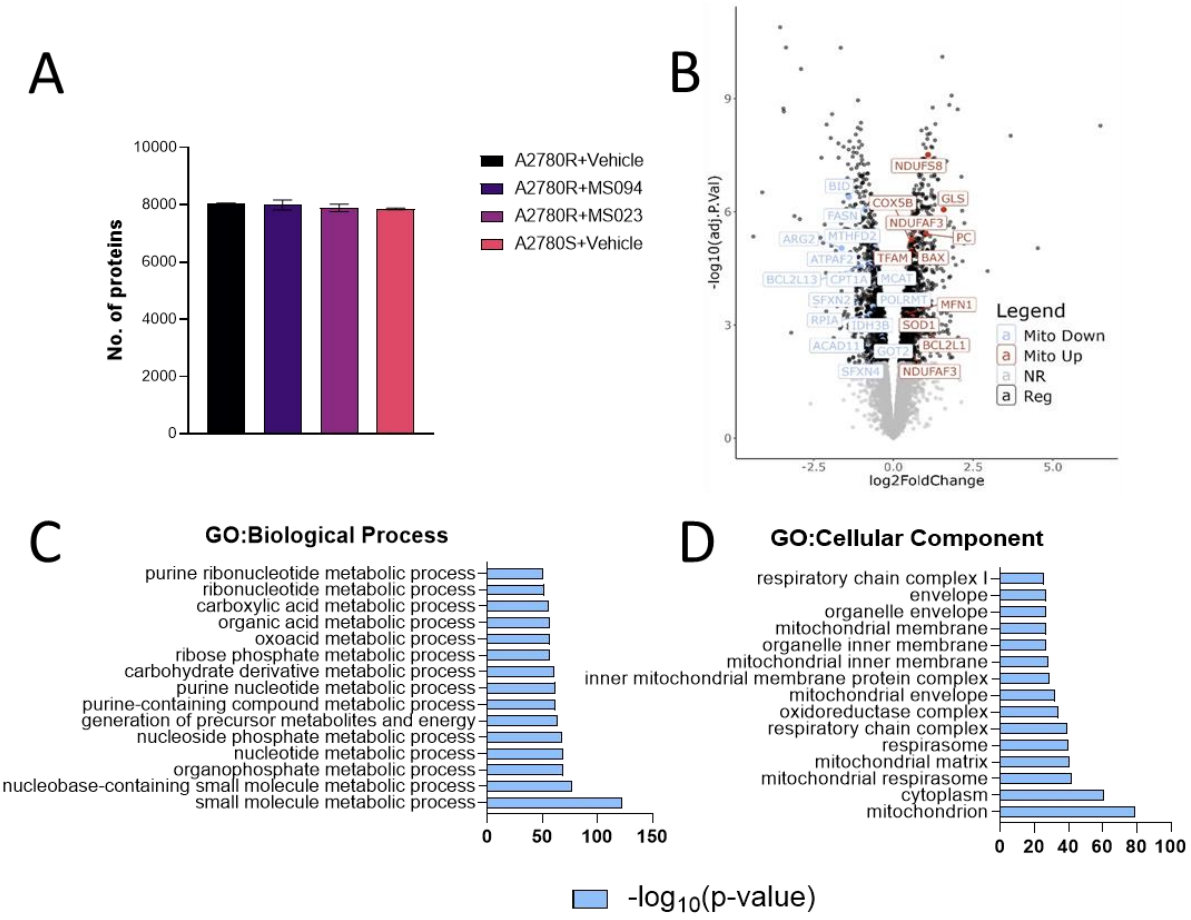

Figure 21: MS-based DIA proteomic analysis of label-free A2780R and A2780S cells
(A): Number of proteins identified in A2780S and vehicle/MS094/MS023-treated A2780R cells. The error bars (n=3) represent the standard deviation between replicates. **(B)** Volcano plot depicting differentially expressed proteins (black dots) between A2780R and A2780S. A total of 1363 proteins were significantly upregulated and 1139 were downregulated in A2780R compared to A2780S (FDR < 0.01). Mitochondrial genes are highlighted in red (upregulated) and blue (downregulated). **(C-D)** Top 15 regulated pathways emerging from a functional analysis by gene ontology (GO) of biological processes and cellular components, respectively. Differentially expressed proteins between A2780R versus A2780S were used as the analysis set (FDR <0.05).

5.3.2 Gene Ontology analysis shows that inhibition of Type-I PRMTs induces lipid synthesis and autophagosome formation

To investigate the effects of MS023 on global protein expression of A2780R, we performed their proteomic profiling following a 48h treatment with MS023, with MS094, which was included as a negative control. It has already been shown that PRMT1 inhibition exerts limited gene expression changes in short time windows (Kleinschmidt *et al.*, 2008; Cao *et al.*, 2025). Substantial changes in overall protein abundance were not expected, and indeed, we found 363 upregulated and 748 downregulated proteins. However, proteome-wide analysis was conducted to delineate the cellular processes and components impacted by MS023. As previously described,

sample preparation, acquisition, and identification and quantification of raw intensities were performed.

The results acquired are summarised in the plot in **Figure 22** for MS023-treated versus MS094-treated A2780R. Genes from left to right were ranked from high to low based on their fold change, and the plot was further organised into two parts: the lower grey section shows the ranked list metrics (fold change values) used to order all proteins. Here, we observed that the majority of protein fold changes remain close to zero, except for a small proportion at the extreme left (positive fold change) and extreme right (negative fold change). This result suggested that MS023 does not significantly influence protein synthesis and/or degradation enough to alter protein expression levels at the 48-hour time point. The upper part of the plot displays normalised enrichment scores calculated where peaks indicate the maximum enrichment of the top 5 upregulated (towards the left, marked with warmer colours) and downregulated (towards the right, marked with cooler colours) cellular component terms (**Figure 22A**) and biological processes (**Figure 22B**). Overall, in this cell line, we observed the downregulation of nuclear processes and the upregulation of cytosolic processes. In the nucleus, terms related to DNA replication, cell division, and chromosomal maintenance are downregulated. In contrast, in the cytosol, terms associated with lipid and cholesterol synthesis, autophagy and endosome formation are upregulated.

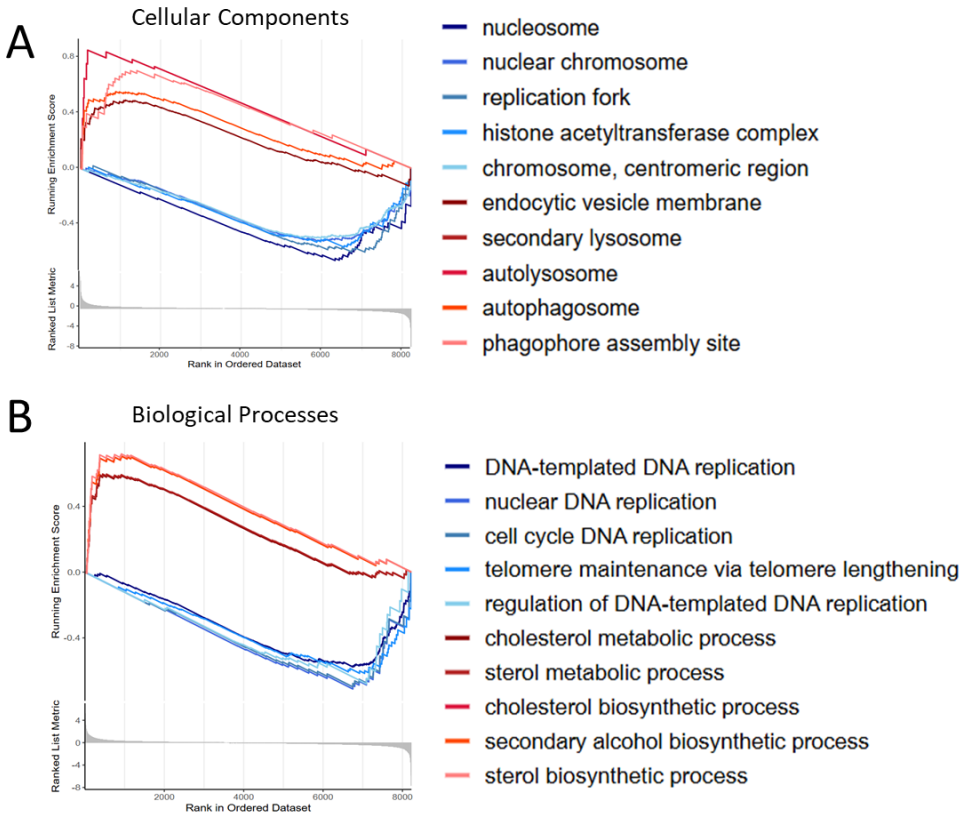

Figure 22: Gene set enrichment analysis of MS023-treated A2780R cells compared to MS094-treated cells
Plots representing the significant terms (FDR<0.05) obtained through gene set enrichment analysis (GSEA), ranked by the normalised enrichment score (NES) for **(A)** cellular components and **(B)** biological processes in A2780R. The fold change (MS023-treated A2780R over MS094-treated A2780R) was used to rank the list of genes corresponding to the terms from the Gene Ontology (GO) database.

5.3.3 Steady-state metabolomic analysis reveals that A2780R cells show a metabolic shift towards anabolism and rewiring of redox balance

We then performed a steady-state metabolomics analysis to explore the molecular basis of metabolic adaptation in A2780R cells and whether MS023 could influence metabolic pathways. Metabolites were extracted with an ice-cold extraction buffer of methanol, acetonitrile, and water to facilitate the extraction of polar and non-polar metabolites while inducing rapid metabolic quenching and protein precipitation.

In a triple-quadrupole mass spectrometer, by LC-MS/MS analysis, we profiled 110 metabolites that were involved in various pathways, including glycolysis, the tricarboxylic acid (TCA) cycle, the pentose phosphate pathway, fatty acid β-oxidation, and amino acid metabolism. Principal component analysis (PCA) showed that the A2780R cluster was distinctly separated from A2780S, indicating a significantly different overall metabolic profile (**Figure 23A**). We identified 42

metabolites that were upregulated and 40 that were downregulated in A2780R cells compared to A2780S (**Figure 23B**). A pathway analysis of these differentially regulated metabolites highlighted the involvement of nucleotide and glutathione metabolism, which we will discuss further in depth (**Figure 23C**). The TCA cycle and glycine, serine and threonine metabolism were also significantly modulated among other pathways.

Overall, A2780R cells showed more extensive usage of essential and non-essential amino acids and increased amino acid catabolism (**Figure 23D**). Among all the non-essential amino acids, we also observed a remarkable utilisation of serine in A2780R cells and a concomitant increase in inosine monophosphate (IMP). Serine is either taken up or produced *de novo* from 3-phosphoglycerate, a glycolytic intermediate, which can be converted to glycine and subsequently to IMP, a vital intermediate for nucleotide synthesis. As expected, a rising trend in ribonucleotide production and an elevated purine-pyrimidine ratio (**Figure 23E**) were observed. Furthermore, the long-chain to free carnitine ratio (C18+C16/C0) was calculated as a measure of carnitine palmitoyl transferase 1 (CPT1) activity, the rate-limiting enzyme of mitochondrial β-oxidation, and the acetylcarnitine-to-free carnitine (C2/C0) ratio was used as an overall indicator of fatty acid β-oxidation. A significant reduction was observed in CPT1 activity, and β-oxidation levels followed this trend in A2780R cells, suggesting that mitochondrial β-oxidation is downregulated in A2780R cells (**Figure 23F**).

In summary, this data indicated that A2780R cells have adapted by utilising amino acids to produce nucleotides, reflecting the upregulation of anabolic pathways to support cell proliferation under genotoxic stress conditions.

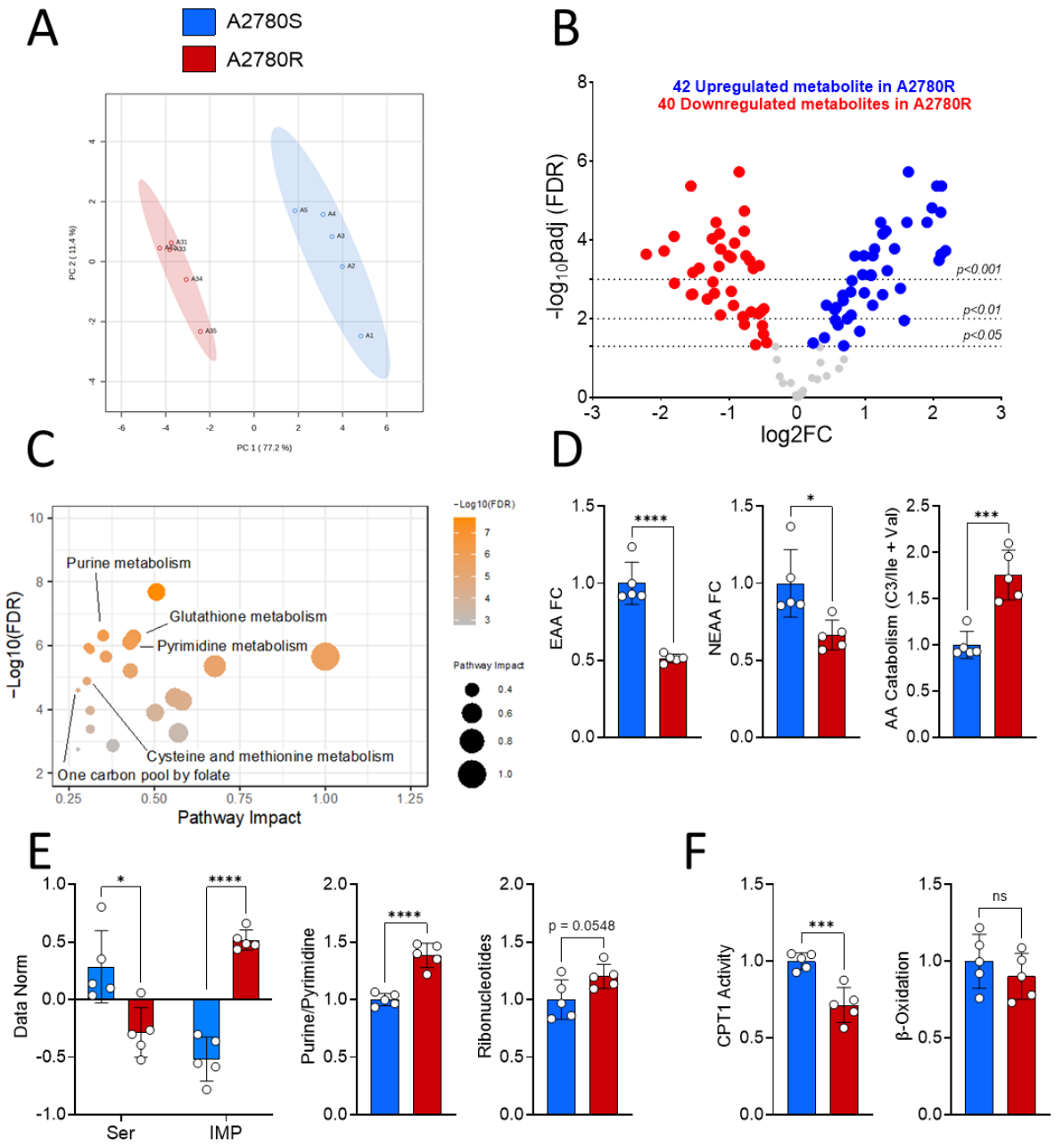

Figure 23: Steady-state metabolomic analysis of A2780R and A2780S cells in basal conditions

(A) Principal Component Analysis (PCA) of metabolite profiles shows separation between A2780R (red) and A2780S (blue) cell lines, indicating distinct metabolic states. **(B)** Volcano plot depicting differentially abundant metabolites between A2780R and A2780S. 42 metabolites were significantly upregulated and 40 were downregulated in A2780R compared to A2780S (FDR < 0.05). **(C)** Pathway enrichment and topology analysis using MetaboAnalyst software highlights significantly altered metabolic pathways in A2780R cells, including purine metabolism, glutathione metabolism, pyrimidine metabolism, cysteine and methionine metabolism, and the one-carbon pool by folate pathway. Circle size represents pathway impact; colour indicates –log10(FDR). **(D–F)** The relative abundance of metabolites (values normalised over median) or metabolite ratios (normalised over A2780S) involved in anabolism was significantly altered in A2780R versus A2780S cells, where EAA = Essential Amino Acids, NEAA = Non-Essential Amino Acids, AA = Amino acids, Ser = Serine, IMP = Inosine monophosphate, CPT1 = Carnitine Palmitoyl Transferase. Bar graphs represent mean ± SD, with individual biological replicates shown as circles

(n=5). Statistical analysis was performed using Student's *t*-test, where ****=p<0.0001, ***=p<0.001, **=p<0.01 and *=p<0.05

Anabolic processes, including cholesterol synthesis and nucleotide production, require NADPH (reduced nicotinamide adenine dinucleotide phosphate) as an electron donor. NADPH can be obtained from the pentose phosphate pathway, TCA, and folate cycles. NADPH is also essential for regenerating glutathione (GSH), the primary scavenger of reactive oxygen species (ROS), from its oxidised form (GSSG). Therefore, NADP+/NADPH and GSH/GSSG ratios can influence the cellular redox state. Indeed, A2780R cells showed an altered redox metabolism, distinct from A2780S cells. Higher levels of intermediates of the pentose phosphate pathway (PPP) indicated increased NADPH production (**Figure 24A**), while simultaneously, the increased NADP+/NADPH ratio suggested rapid NADPH consumption (**Figure 24B**). A rising trend in several TCA cycle metabolites was also observed in A2780R cells, except for Acetyl-CoA and α-ketoglutarate (**Figure 24C**). A2780R cells did not show differences in the GSH-to-GSSG ratio, but overall levels of GSH, its precursor cysteine, and of GSSG were significantly higher, suggesting enhanced antioxidant response (**Figure 24D**). Another parameter reflecting the redox status is the NAD+/NADH ratio. NAD+ is the oxidised form that accepts electrons during catabolism, whereas NADH is the reduced form that donates electrons to the electron transport chain. Although a trend towards reduction of the NAD+/NADH ratio was observed in A2780R cells, there was an overall rise of both the metabolites (**Figure 24E**). The expansion of the overall NAD pool and the increased TCA flux suggest increased activity in catabolic pathways and enhanced mitochondrial function.

In summary, the metabolomic characterisation of A2780R cells indicated increased metabolic activity and enhanced antioxidant response under genotoxic stress adaptation.

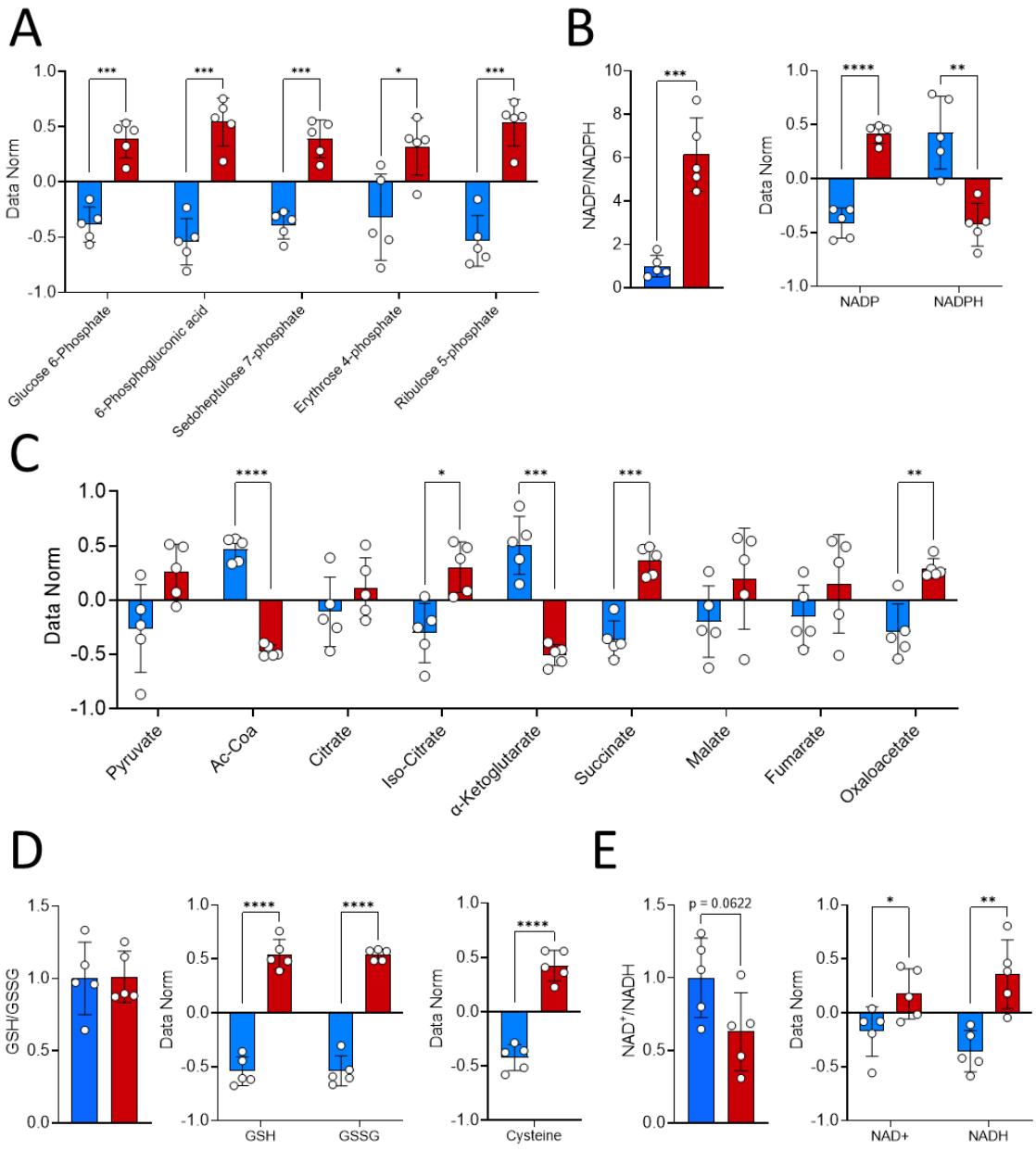

Figure 24: Metabolomic profiling indicates higher antioxidant response and mitochondrial activity in A2780R (red) than in A2780S (blue) cell line

The relative abundance of metabolites (values normalised over median) involved in **(A)** pentose phosphate pathway and **(B)** metabolite ratios (normalised over A2780S) indicating higher production but subsequent utilisation of NADPH **(C)** Relative abundance of TCA cycle metabolites showing a rising trend in A2780R cells. **(D)** Relative quantification of GSH, GSSH and cysteine reflecting an increased flux of antioxidant response in A2780R cells **(E)**. Increased NAD+ and NADH indicate higher metabolic activity/mitochondrial function. Bar graphs represent mean ± SD, with individual biological replicates shown as dots (n=5). Statistical analysis was performed using Student's *t*-test, where ****=p<0.0001, ***=p<0.001, **=p<0.01 and *=p<0.05

5.3.4 Inhibition of Type I PRMTs impacts redox balance and potentially induces mitochondrial dysfunction in A2780R

Next, we examined how inhibiting Type-I PRMTs could affect the metabolic profiles of A2780R. Similar to the proteomic analysis, we found that samples treated with MS023 clustered separately from vehicle and MS094-treated samples in A2780R (**Figure 25A**) cells. A volcano plot depicting differently regulated metabolites in MS023-treated samples compared to MS094-treated samples highlighted 10 metabolites upregulated and 22 downregulated (**Figure 25B**). In MS023-treated A2780R cells, targeted metabolomics indicated a substantial reduction in amino-acid catabolism, accompanied by a rising trend in serine and a decreasing trend in IMP levels in response to the inhibition of type-I PRMTs. Interestingly, bulk ribonucleotide remained unchanged (**Figure 25C**), suggesting that nucleotide homeostasis was largely maintained—potentially through buffering by salvage pathways. Even though an increasing trend was observed in CPT1 activity, overall β-oxidation remained unchanged (**Figure 25D**). Redox-related amino acids were also affected: cysteine displayed a decreasing trend, while both glycine and glutamate—key precursors for glutathione biosynthesis—were significantly reduced. Concordantly, total glutathione pools declined, with significant decreases in both reduced (GSH) and oxidised (GSSG) species following MS023 treatment (**Figure 25E**). The increase of serine alongside a substantial drop of glycine is possibly due to altered flux in the serine–glycine conversion belonging to the one-carbon pathway and/or reduced conversion of serine to glycine, without impacting the overall ribonucleotide levels. These coordinated changes suggest that MS023 disrupts the glutathione system at the levels of precursor supply and overall pool size, indicating impaired antioxidant capacity that hampers both GSH production and its utilisation within detoxification processes. Finally, MS023 treatment significantly decreased NADH while NAD^+ remained stable (**Figure 25F**), resulting in a lower NAD^+/NADH ratio. This change suggests lower mitochondrial function, possibly at the level of the electron transport chain or reduced production of reducing equivalents from the TCA cycle. However, no marked difference was observed in the $NADP^+$/NADPH ratio as well as their individual levels (**Figure 25G**).

Together, these data support a model whereby MS023 alters amino acid and nucleotide metabolism, while simultaneously weakening glutathione-mediated redox buffering. Inhibition of type-1 PRMTs reduces the mitochondrial redox balance, creating a metabolic environment less capable of withstanding the oxidative stress and maintaining bioenergetic stability, which were found to be key in the metabolic adaptations of A2780R cells. Given that MS023 treatment also reduced OCR levels (**Figure 15A**), these data suggest that inhibition of type-1 PRMTs shifts the mitochondrial phenotype of resistant cells closer to that of sensitive cells.

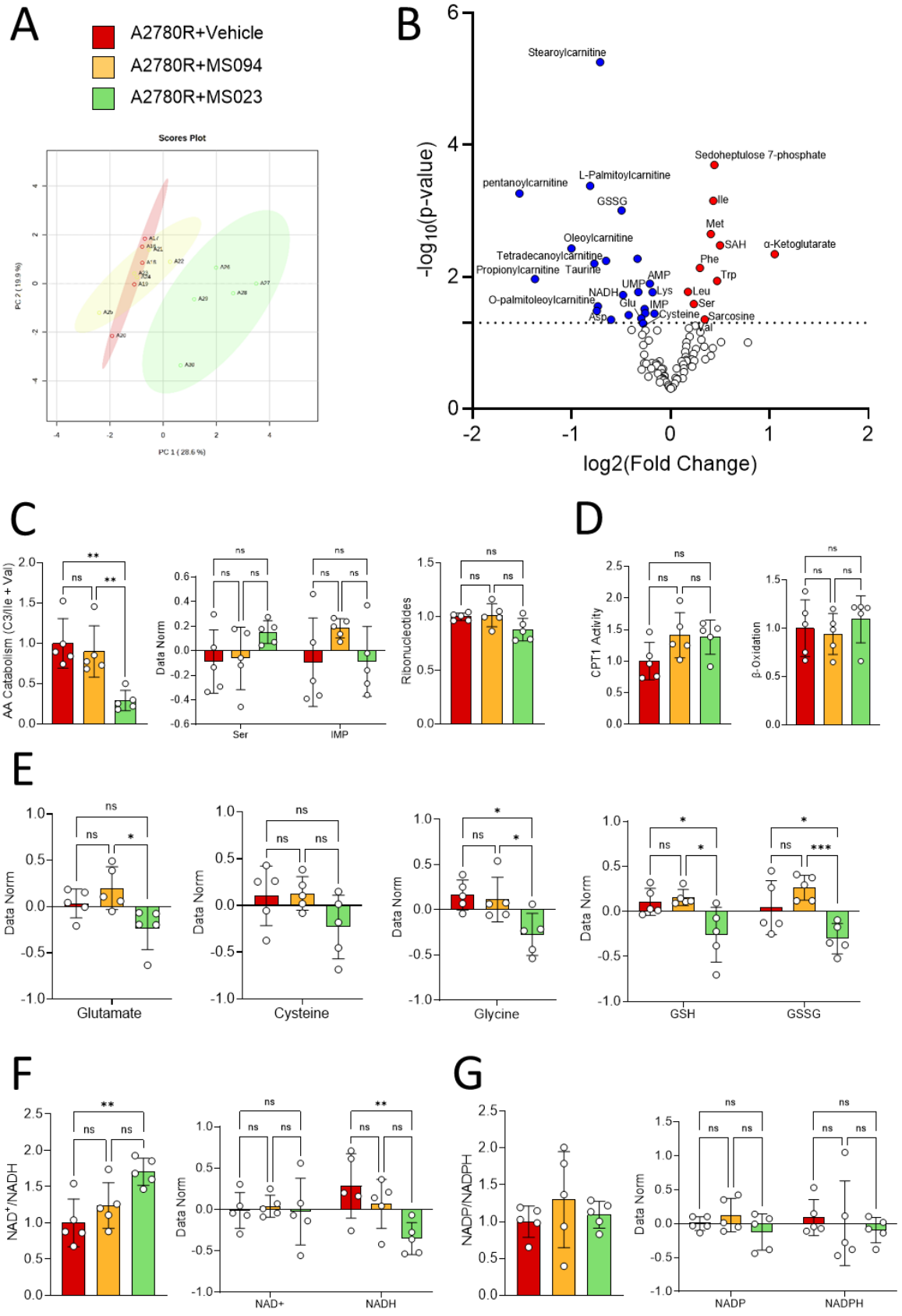

Figure 25: Metabolomic profiling reveals that MS023 dampens antioxidant response and catabolism in A2780R cells

(A) Principal Component Analysis (PCA) of metabolite profiles shows clear separation between MS023-treated (green) and Vehicle (red) and/or MS094 (yellow)-treated A2780R cells, indicating

their distinct metabolic states. **(B)** Volcano plot depicting differentially abundant metabolites between MS023-treated A2780R over MS094-treated A2780R cells (FDR < 0.05). The relative abundance of metabolites (values normalised over median) or metabolite ratios (normalised over vehicle-treated A2780R) shows **(C)** reduced amino acid utilisation in A2780R, where AA = Amino acids, Ser = Serine, IMP = Inosine monophosphate. (**D**) increasing trend in CPT1 activity but no difference in β-oxidation levels **(E)** reduced GSH and GSSG levels along with its three precursor amino acids glutamate, cysteine and glycine and **(F)** a reduction in NADH levels resulting in a higher NAD^+/NADH ratio. **(G)** No observable differences are found in the $NADP^+$/NADPH ratio and their individual levels. Bar graphs represent mean ± SD, with individual biological replicates shown as dots (n=5). Statistical analysis was performed using one-way ANOVA test, where ****=p<0.0001, ***=p<0.001, **=p<0.01 and *=p<0.05.

5.3.5 Integrative analysis of proteomics and metabolomics dataset highlights that central carbon metabolism is affected by Type-I PRMT inhibition

Next, we integrated the proteomics and metabolomics datasets of MS023-treated A2780R to identify the key pathways regulated by Type-I PRMTs in modulating protein expression, which affect cellular metabolic processes.

In A2780R cells, pathway enrichment analysis revealed a pronounced shift in amino acid metabolism, with arginine biosynthesis emerging as the most significantly altered process by Type-I PRMT inhibition. This possibly indicates MS023 alters nitrogen handling and polyamine synthesis, which have been linked to vulnerabilities in handling chemoresistance (Casero, Murray Stewart and Pegg, 2018; Chen, Chen and Yu, 2020; G. Ji *et al.*, 2024). The simultaneous enrichment of alanine, aspartate, and glutamate metabolism and the TCA cycle suggested that MS023 impacts the anaplerotic flux, possibly impinging on energy production and supply for biosynthetic precursors, consistent with the metabolomics results discussed (**see results 5.3.3**). Glutathione metabolism pointed towards altering redox buffering capacity, consistent with reduced oxidative stress defence in A2780R cells upon MS023 treatment. MS023 also impacted purine and pyrimidine metabolism, although we did not observe any difference in the purine-to-pyrimidine ratio, suggesting heightened nucleotide turnover or repair activity. Changes in one-carbon metabolism (cysteine/methionine metabolism and folate pool) relate to the impact on both redox balance and nucleotide synthesis demands (**Figure 26**).

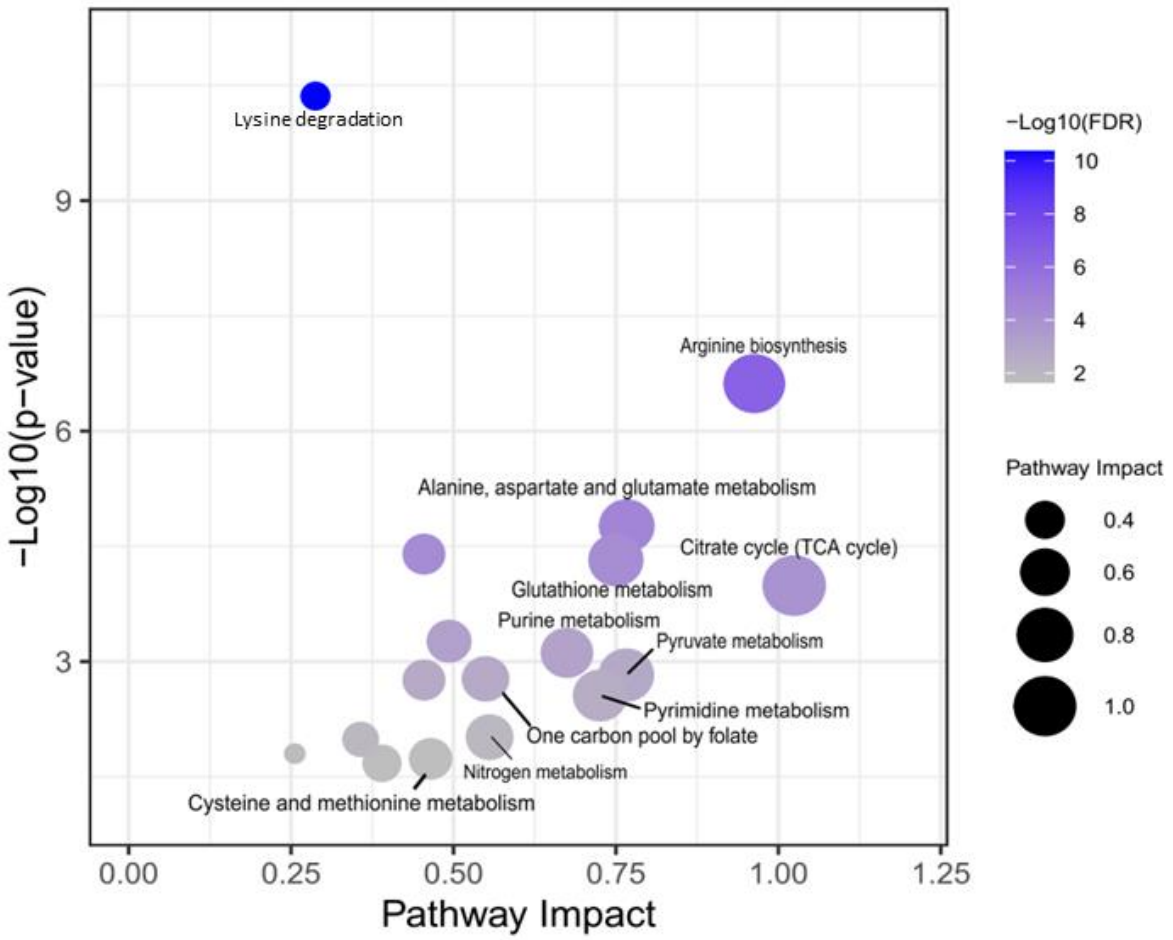

Figure 26: Integrated proteomic and metabolomic pathway enrichment analysis of MS023-treated A2780R cells
Significantly enriched metabolic pathways identified in A2780R cells following Type-I PRMT inhibition with MS023, based on proteomic and metabolomic datasets. Circle size indicates pathway impact; colour gradient shows –log10(FDR).

5.4 Analysis of the redox rewiring and nutrient utilisation of resistant ovarian cancer cells

Stable isotope tracing with ^{13}C-labelled substrates is a standard method to investigate metabolic pathway activities and carbon flows in biological systems. In this method, cells or organisms are given a metabolite precursor (such as glucose or glutamine) with the stable, non-radioactive isotope ^{13}C. As the labelled substrate is processed by enzymes, ^{13}C atoms are integrated into downstream metabolites based on the structure and activity of the associated metabolic network. The resulting labelling patterns are measured using high-resolution mass spectrometry, allowing for the analysis of isotopologue distributions (M0, M2, M3, etc.). Interpreting these data within the framework of known biochemical pathways offers insights into pathway engagement, flux direction, and metabolic rewiring under the specific experimental conditions.

Therefore, to investigate how Type-I PRMTs influence metabolic adaptations in driving chemoresistance, we closely examined the redox balance and nutrient utilisation in A2780R cells, previously identified as the primary adaptation in these cells. We hypothesised that these cells actively route glutamine or serine carbon into GSH production. To strengthen the link between Type-I PRMT-mediated metabolic rewiring and drug resistance, we performed targeted glutamine and serine isotope tracing experiments in A2780R cells with and without Type-I PRMT inhibition with MS023. Glutamine is taken up by cells and converted to glutamate, which directly feeds into glutathione synthesis. Conversely, serine can be directly taken up or synthesised *de novo* from glycolytic intermediate 3-phosphoglycerate. Regardless of its origin, serine can be converted to glycine by serine hydroxymethyltransferases (SHMT1/2). Glycine is a precursor of glutathione synthesis in the transsulfuration pathway. Additionally, serine can also be converted to cysteine, another precursor of glutathione. Hence, tracing the ^{13}C isotope of serine and glutamine enabled us to map the contribution of these precursor amino acids to GSH generation and, therefore, antioxidant defence, which was crucial for A2780R cells to oppose CBP.

5.3.1 A2780R cells rely on serine-derived carbon for GSH synthesis, and MS023 significantly reduces both serine and glutamine uptake

In A2780S cells, glutamine tracing revealed a reduction in the unlabelled GSH fraction (M0) and an increased incorporation of tracer-derived carbons into GSH, suggesting that these cells actively synthesise GSH from glutamine. In contrast, resistant cells showed reduced abundances of multiple GSH isotopologues (M2, M3, and M5), consistent with an altered pattern of glutamine-derived GSH synthesis (**Figure 27A**). This shift may reflect the rerouting of glutamine carbons into alternative metabolic pools (TCA anaplerosis, nucleotide synthesis) or a preferential utilisation of other precursors. Following MS023 treatment, no differences were observed in the glutamine-derived carbon labelled GSH pool in A2780R cells (**Figure 27A**). Interestingly, in resistant cells, intracellular M5 glutamine abundance was reduced with MS023 treatment, reaching levels comparable to A2780S cells. This finding suggests that MS023 suppresses the enhanced glutamine uptake characteristic of untreated A2780R cells (**Figure 27B**).

$^{13}C_3$-Serine tracing experiments uncovered additional differences in GSH biosynthesis. In A2780R cells, the M3 isotopologue of serine was slightly, though not significantly, lower than in A2780S, and became significantly decreased after MS023 (**Figure 27C**). Concomitantly, the unlabelled serine pool (M0) increased with MS023, consistent with enhanced endogenous serine synthesis rather than uptake (**Figure 27C**). Downstream, resistant cells, particularly under MS023, showed higher incorporation of serine-derived carbon into GSH M2, consistent with the glycine

moiety carrying the label (**Figure 27D**). While intracellular glycine M2 enrichment was elevated in resistant versus sensitive cells, MS023 reduced glycine M2 to A2780S-like levels (**Figure 27E**). This reduction is consistent with either suppressed serine-to-glycine conversion and/or increased incorporation of labelled glycine into GSH; the concomitant rise in GSH M2 suggests the latter likely contributes. However, this aspect needs to be further validated.

Nucleotide labelling revealed further metabolic rewiring: resistant cells exhibited a pronounced loss of serine-derived carbons in AMP (M2) with a concomitant increase in the unlabelled fraction (M0), and this shift was accentuated by MS023 treatment (**Figure 27F**). These data indicate that PRMT inhibition strengthens the diversion of serine away from purine synthesis.

The reduced serine contribution to nucleotide synthesis and restored glutamine handling (normalisation of glutamine labelling and reduction of intracellular M5 glutamine) are likely to constrain nucleotide availability and biosynthetic capacity in A2780R cells. This metabolic limitation undermined their proliferative and repair advantage, providing a plausible explanation for the restored CBP sensitivity observed upon MS023 treatment.

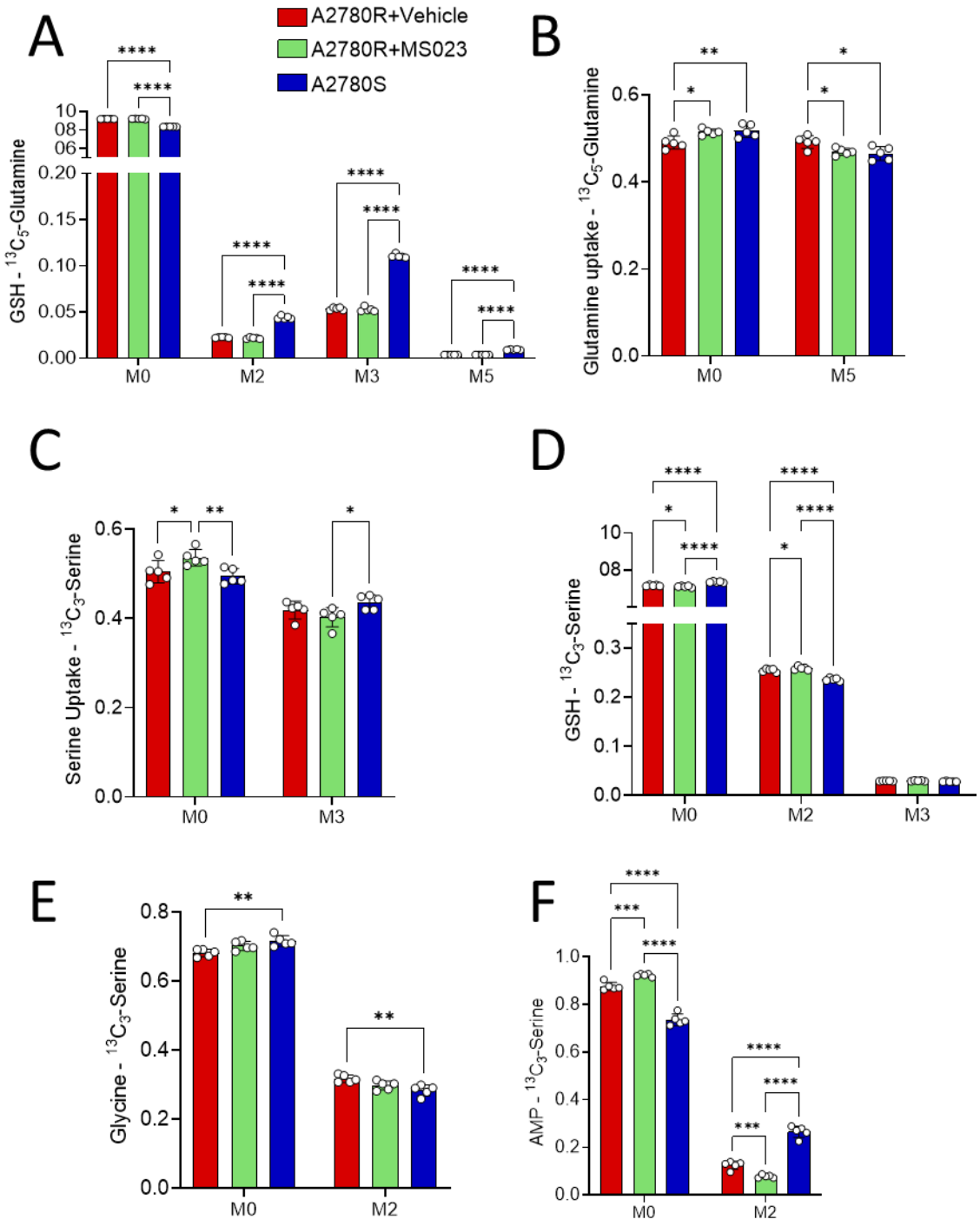

Figure 27: U-$^{13}C_5$-glutamine or U-$^{13}C_3$-serine contribution to central carbon metabolism in A2780R cells (Vehicle and MS023-treated) and A2780S cells

Cells were incubated with either U-$^{13}C_5$-glutamine or U-$^{13}C_3$-serine, and isotopic enrichment of downstream metabolites was quantified by LC-MS. Fractional contribution of labelled glutamine to GSH (A) and uptake of labelled glutamine (measured from media; **B**) expressed as the percentage of ^{13}C-labeled isotopologues. Fractional contribution of labelled serine to GSH (**C**), serine uptake (**D**), conversion to glycine (**E**) and incorporation into AMP (**F**). Data are presented as mean ± SD from $n = 5$ biological replicates. Statistical significance was determined by two-way ANOVA with Tukey's post hoc test; $p < 0.05$, $p < 0.01$, $p < 0.001$.

5.5 Analysis of the effect of inhibition of Type-I PRMTs on SkOV3 cell line

In *Musiani et. al., 2020*, our group demonstrated that inhibition of type-I PRMTs can sensitise SkOV3 cells under an acute response to platinum ions. Precisely, 48h of treatment with MS023 prior to cisplatin treatment (24h) showed a significant reduction in colony formation. In this study, they also elucidate that the sensitisation occurs due to the dampening of NF-ϰB signalling pathway, as PRMT1 (the major Type-I PRMT) is known to regulate NF-ϰB by modulating ADMA on its RelA subunit (Hassa *et al.*, 2008; Reintjes *et al.*, 2016). NF-ϰB is a known physiological regulator of mitochondrial respiration. As a stress response mechanism, it maintains energy homeostasis and contributes to metabolic adaptation by upregulating mitochondrial respiration levels (Mauro *et al.*, 2011). Additionally, when we integrated proteomic and transcriptomic data from cisplatin-treated SkOV3 cells, we observed post-transcriptional regulation of several electron transport chain subunits (**Figure 9**).

Based on these pieces of data, we also set out to test our hypothesis on SkOV3 cells to understand if there is a direct mechanistic link between Type-I PRMTs and mitochondrial function and/or metabolism, beyond the regulatory aspect by NF-ϰB. We measured mitochondrial oxygen consumption rate, mtDNA content, membrane potential and mitophagy flux with previously described methods (**see result 5.2**) using MS023 with the optimised doses (10μM) and timing (48h) described by Musiani et. al., 2020. We also performed steady-state targeted metabolomic and untargeted proteomic analysis with MS023 treatment and integrated the datasets to identify nodes of impact. Finally, we assessed mitochondrial fuel utilisation (dependency, capacity and flexibility) by using the Seahorse fuel flexibility test to comprehensively understand the metabolic status of SkOV3 cells both at the basal level and upon MS023 treatment.

5.5.1 Inhibition of Type-I PRMTs reduces mitochondrial OCR in SkOV3 cells

First, we performed the Mitostress test again to understand if the mitochondrial OCR is modulated with pharmacological inhibition of Type-I PRMT by MS023. We observed a similar reduction pattern on mitochondrial OCR upon MS023, while MS094 had the same phenotype as the vehicle. Interestingly, from the energy map we deciphered that SkOV3 cells relied almost entirely on mitochondrial oxidative phosphorylation (**Figure 28A**). We further evaluated mitochondrial DNA copy number. Similar to A2780R cells, we observed no differences with MS023 treatment (**Figure 28B**). The membrane potential was analysed by JC1 staining. Here, we observed a slight yet significant increase in membrane potential upon MS023 treatment (**Figure 28C**). Altogether, these results show that MS023 reduces mitochondrial OCR in SkOV3 cells.

However, the mode of action to elicit this phenotype seems to be different from that of A2780R cells.

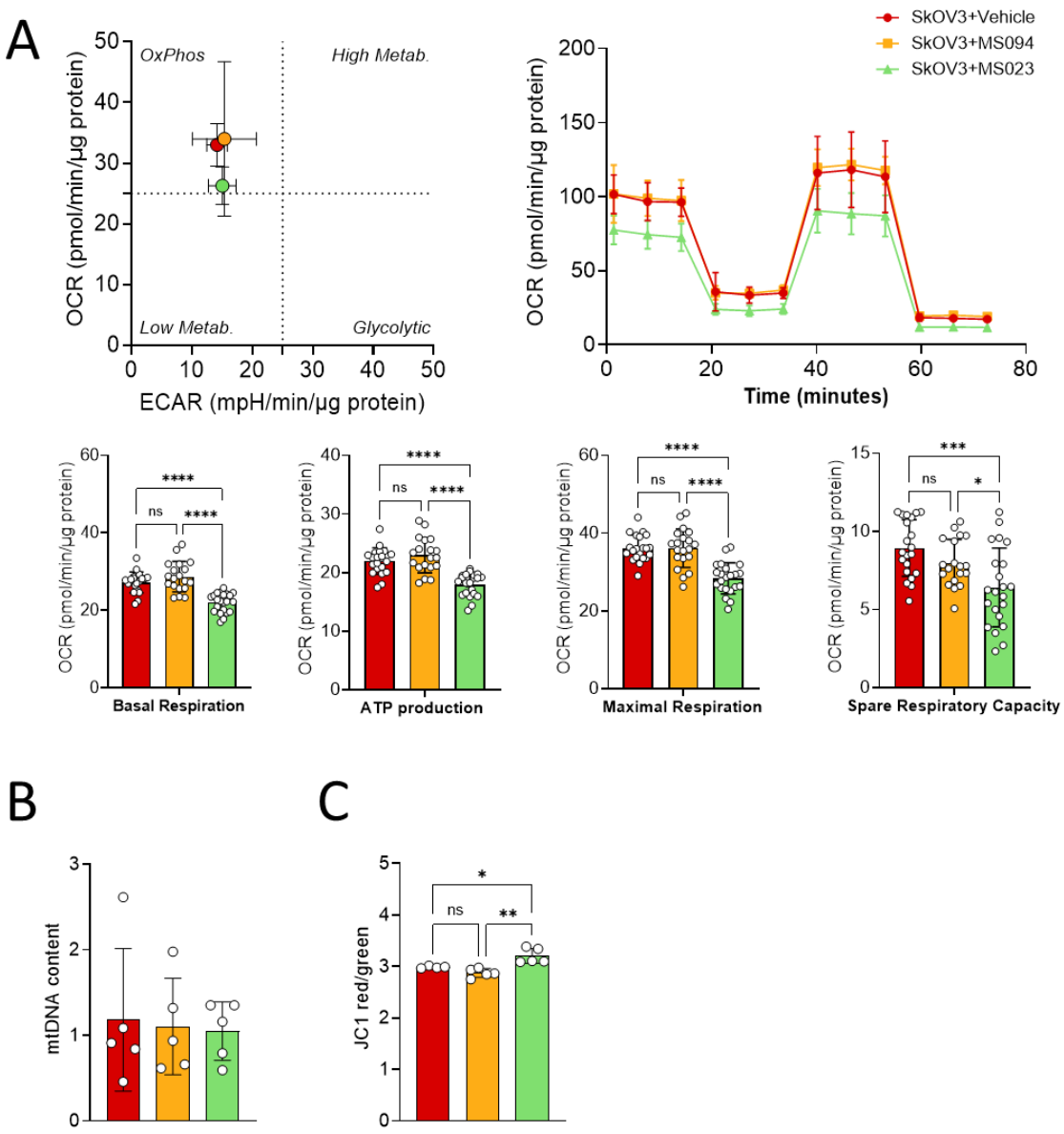

Figure 28: Evaluation of mitochondrial function at the basal state and upon MS023 in SkOV3 cells

(**A**) Seahorse Mitostress test performed using oligomycin, FCCP and rotenone/antimycin A, respectively, in injection ports and the raw OCR levels were normalised over the total protein amount estimated (n=3). (**B**) 10ng DNA per sample was amplified by qPCR using Taqman probes and primer pairs for COXII (mtDNA) and normalised over 36B4 (nuclear) genes. The expression level was calculated using the following formula: expression = $2^{(-\Delta\Delta Ct}$. (**C**) The ratio of JC-1 aggregates to monomers (red/green) indicates mitochondrial polarisation. Bar graphs represent mean ± SD and one-way ANOVA was used to perform statistics where ****=<0.0001, ***=<0.001, **=<0.01 and *=<0.05.

Thereafter, we checked the mitophagy flux to assess whether the reduction of OCR is due to the degradation of mitochondria. We tagged mt-mKEIMA to the mitochondrial membrane similar to A2780R cells (see result 5.2.4) and treated them with MS023 48h before flow cytometry analysis. CCCP was used as a positive control, and bafilomycin A was used as an autophagosome inhibitor. We detected a significant Stokes shift in MS023-treated samples, testifying to an induction of mitophagy in SkOV3 cells and with bafilomycin A, this shift was reversed (**Figure 29A**). Unlike A2780R cells, in the SkOV3 cell line, we also detected cytosolic LC3BI at a basal level, and a clear conversion to lipidated LC3BII appeared upon both CCCP-treated positive control and MS023 treatment, suggesting autophagosome formation. Bafilomycin A treatment further intensified the LC3BII band, indicating that induction of mitophagy by MS023 is upstream of autophagosome formation (**Figure 29B**). The autophagy receptor p62 was found to be depleted in both CCCP and MS023-treated cells, indicating a proper fusion of the autophagosome with the lysosome and thereby a mitophagic clearance. As expected, bafilomycin A treatment increased the levels of p62 in MS023-treated samples (**Figure 29B**). To corroborate these data, we also measured the mitochondrial status of SkOV3 cells following MS023 treatment using live-cell imaging with mitotracker staining. We further assessed mitochondrial protein levels through western blots targeting Heat Shock Protein 60 (HSP60; matrix marker) and Transporter of Outer Membrane 20 (TOM20; membrane marker). After MS023 treatment, the mitochondria were significantly reduced compared to MS094 and the vehicle, but interestingly, they exhibited increased motility and length (**Figure 29C**). Additionally, we detected a depletion of HSP60 and TOM20, which further supports the reduction in mitochondrial matrix and membrane, respectively, in SkOV3 cells (**Figure 29D**). Together, these results confirm that MS023 induces mitophagy in SkOV3 cells, reducing mitochondrial content and subsequently dropping the oxygen consumption rate.

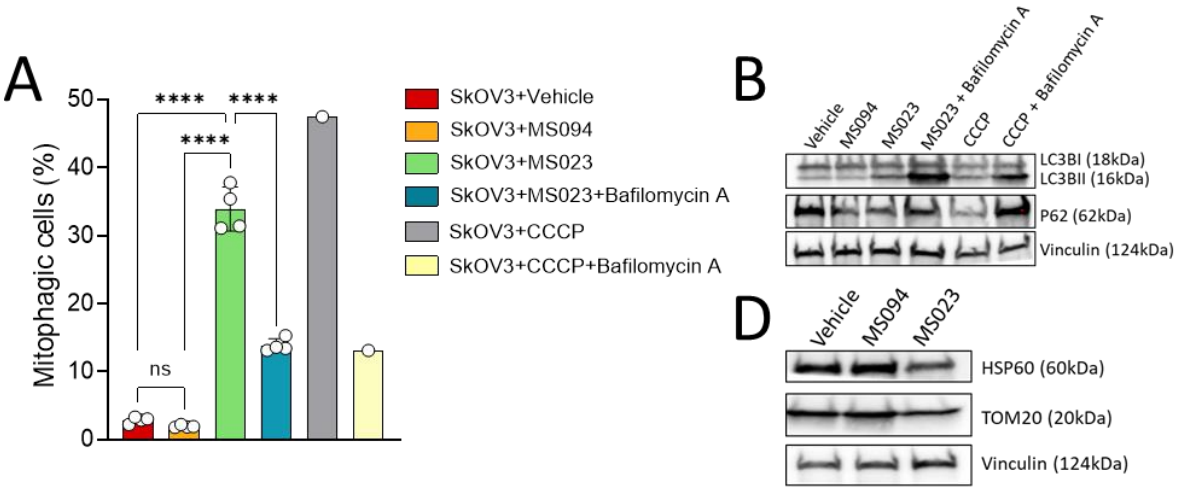

Figure 29: Quantification of mitophagy with MS023 treatment in SkOV3 cells
(**A**)**:** Flow cytometry analysis of mitophagic cell population. The red-to-green fluorescence ratio of mt-mKEIMA depicting the mitophagic cell population in vehicle, MS094 and MS023-treated SkOV3 cells, respectively (n=4), with CCCP (n=1) used as a positive control. As an autophagosome inhibitor, the Bafilomycin A treatment was applied in MS023 (n=4) and CCCP-treated (n=1) cells. Data are presented as mean ± SD. One-way ANOVA was used for statistical analysis, where **** <0.0001. (**B**)**:** Western blot analysis of autophagy markers LC3BI (18kDa), LCBII (16kDa), and p62 (62kDa) in SkOV3 cells. Vinculin (124kDa) served as a housekeeping protein (n=1). (**D**): Western blot analysis of mitochondrial matrix marker HSP60 (60kDa) and membrane marker TOM20 (20kDa) in SkOV3 cells. Vinculin (124kDa) served as a housekeeping protein (n=1).

5.5.2 Integrative analysis of proteomic and metabolomic datasets identifies mitochondrial metabolism to be impacted by Type-I PRMT inhibition

With the untargeted proteomic profiling, we gained a depth of 7800 proteins on average in the whole proteome of SkOV3 cells on average across all treatment conditions (**Figure 30**). Similar to A2780R cells, we observed 430 differentially expressed proteins upon MS023 treatment, out of which 168 were upregulated and 262 were found to be downregulated.

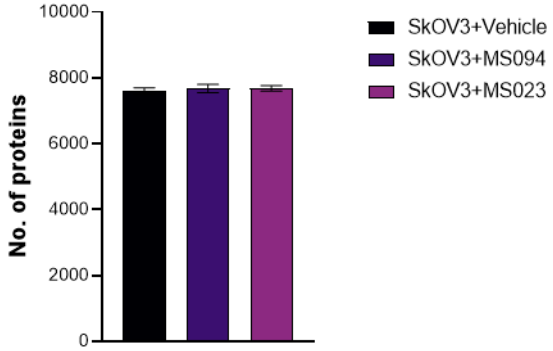

Figure 30: Number of proteins identified in vehicle/MS094/MS023-treated SkOV3 cells
The error bars (n=3) represent the standard deviation between replicates.

The gene ontology analysis highlighted that lipoprotein particles were upregulated among the cellular components, endosome formation, and the mitotic spindle and DNA polymerase complex were downregulated. This analysis possibly indicates downregulation of cell division and induction of autophagy (**Figure 31A**). Simultaneously, among the biological processes, we observed an upregulation of cholesterol biosynthesis and downregulation of terms related to cell division (**Figure 31B**). The proteomics data and subsequent functional analysis through gene ontology were similar among SkOV3 and A2780R cells, which broadly points towards a downregulation of processes in the nucleus and upregulation of processes in the cytoplasm.

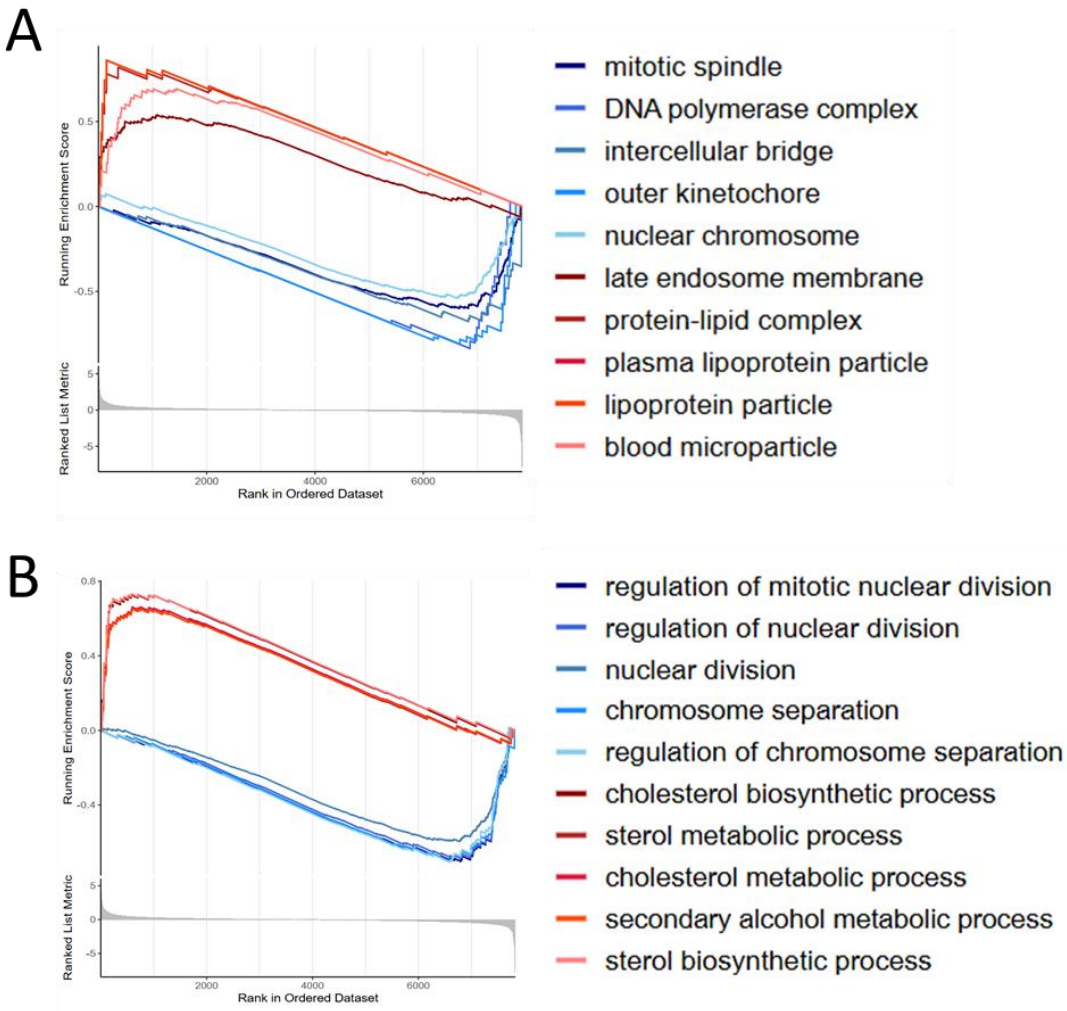

Figure 31: Gene set enrichment analysis of MS023-treated versus MS094-treated SkOV3 cells

Plots representing the significant terms (FDR<0.05) obtained through gene set enrichment analysis (GSEA), ranked by the normalised enrichment score (NES) for **(A)** cellular components and **(B)** biological processes in SkOV3. The fold change (MS023-treated over MS094-treated SkOV3) was used to rank the list of genes corresponding to the terms from the Gene Ontology (GO) database.

Next, we performed a steady-state metabolomics experiment and similar to A2780R cells, the PCA analysis showed MS023-treated SkOV3 cells clustered apart from vehicle and MS094-treated cells (**Figure 32A**). Differentially regulated metabolites between MS023 versus MS094, when plotted in a volcano plot, showed 11 downregulated and 10 upregulated metabolites. Among the downregulated metabolites, we saw an apparent reduction of different acyl-carnitines (**Figure 32B**). Similar to A2780R cells, the MS023 treatment in SkOV3 cells also displayed a broad reduction in amino acid catabolism, implying that Type-I PRMT inhibition reduces amino acid utilisation in both cell types (**Figure 32C**). We detected an increasing trend in IMP levels, but overall ribonucleotide pool remains unchanged (**Figure 32C**). In SkOV3 cells, MS023 seemed to introduce an increasing trend in CPT1 activity and β-oxidation level (**Figure 32D**).

Next, we looked into the individual levels of glutathione and reduced glutathione, as well as the amino acids contributing to glutathione synthesis – glutamate, serine and glycine. We could not detect cysteine in this experiment. GSH and GSSG show a reducing trend upon MS023 treatment, similar to A2780R cells. Concomitantly, we see a downward trend in glutamate and glycine levels, while serine level was found to be increased (**Figure 32E**). Furthermore, we observed an increase in the NAD pool – both in the levels of NAD and NADH (**Figure 32F**). We also detected an upward shift in NADP levels, whereas the NADPH levels remained almost undetectable (**Figure 32G**). This pattern of perturbation was not significant in this cell line, but imitated the observations earlier made on A2780R cells (**Figure 25**).

The metabolomics data indicate that inhibition of type I PRMTs in SkOV3 cells leads to a metabolic downshift, characterised by impaired TCA cycle turnover and perturbations in central carbon metabolism. These effects suggest a reprogramming of mitochondrial energy production rather than a complete switch toward glycolysis, underscoring a role for PRMT activity in maintaining oxidative metabolic capacity in this cell line.

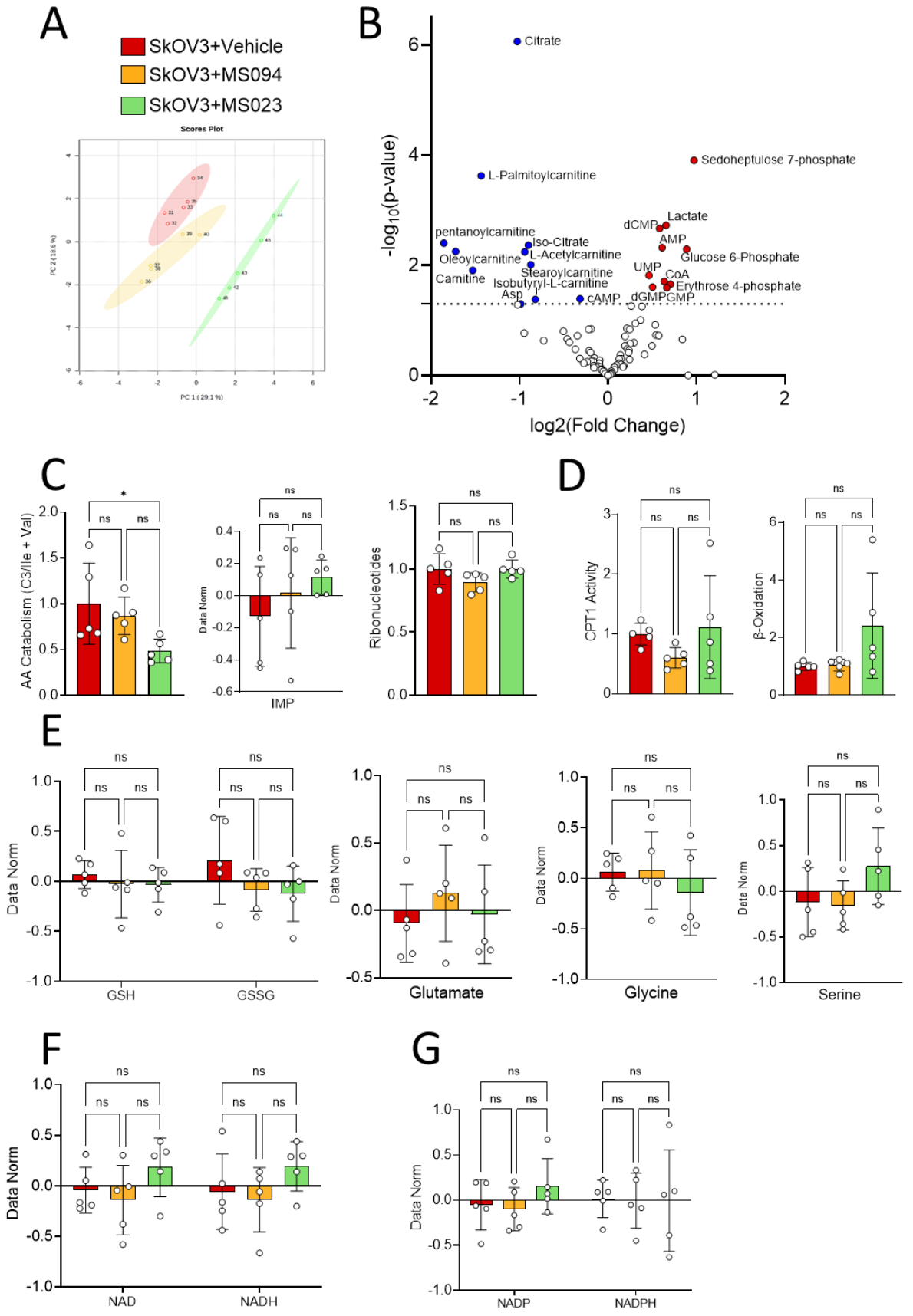

Figure 32: Metabolomic profiling of MS023-treated SkOV3 cells

(A) Principal Component Analysis (PCA) of metabolite profiles shows clear separation between MS023-treated (green) and Vehicle (red) and/or MS094 (yellow)-treated SkOV3 cells, indicating

their distinct metabolic states. **(B)** Volcano plot depicting differentially abundant metabolites between MS023-treated SkOV3 over MS094-treated SkOV3 cells (FDR < 0.05). The relative abundance of metabolites (values normalised over median) or metabolite ratios (normalised over vehicle-treated SkOV3) shows **(C)** a significant reduction in amino acid catabolism, increasing trend in IMP levels, but no difference in ribonucleotide production. (**D**) CPT1 activity and β-oxidation shows an increasing trend **(E) a** reducing trend in GSH, GSSG, glutamate, glycine and increasing trend in serine levels, and **(F-G)** increasing trend in NAD^+, NADH and NADP levels in MS023-treated SkOV3 cell line. Bar graphs represent mean ± SD, with individual biological replicates shown as dots (n=5). Statistical analysis was performed using Student's *t*-test, where ***=p<0.001, **=p<0.01 and *=p<0.05

Afterwards, we performed an integrative analysis of the proteome and metabolome of MS023-treated SkOV3 samples to nail down the central impact nodes of Type-I PRMT inhibition in metabolic pathways. The TCA cycle was prominently enriched in SkOV3 cells upon MS023 treatment, indicating mitochondrial metabolic reprogramming. However, the most significant change was in lysine degradation, a pathway tied to acetyl-CoA production and epigenetic regulation through histone modification. This could reflect a regulation of Type-I PRMTs in metabolic–epigenetic coupling in drug resistance (Fan *et al.*, 2015; Cao *et al.*, 2025). Notably, terpenoid backbone biosynthesis and steroid biosynthesis were altered, implying shifts in isoprenoid and lipid-derived signalling molecules that can influence membrane dynamics, receptor function, and cell signalling in sustaining the resistant phenotype. The enrichment of pyrimidine metabolism aligns with increased demand for nucleotides, while butanoate metabolism and glycerolipid metabolism point toward changes in short-chain fatty acid and membrane lipid metabolism, potentially affecting cell growth and survival (**Figure 33**).

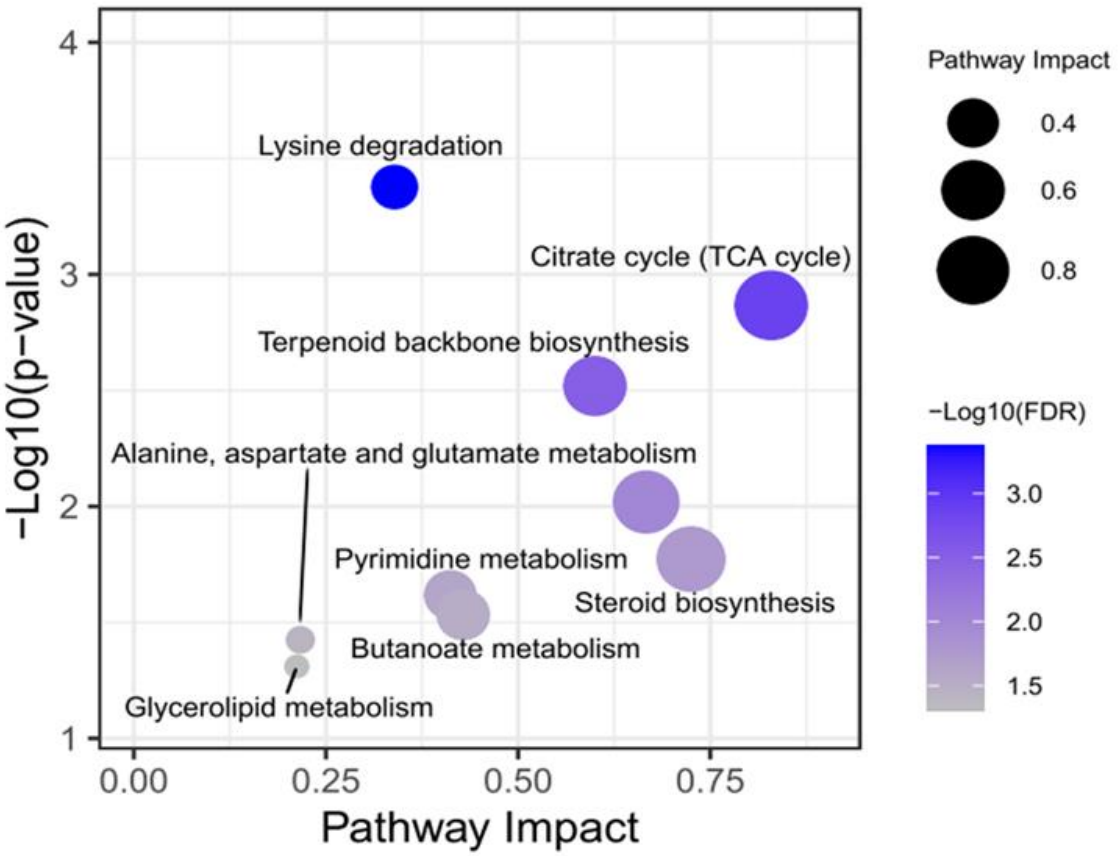

Figure 33: Integrated proteomic and metabolomic pathway enrichment analysis of MS023-treated SkOV3 cells
Significantly enriched metabolic pathways identified in SkOV3 cells following Type-I PRMT inhibition with MS023, based on proteomic and metabolomic datasets. Circle size indicates pathway impact; colour gradient shows –log10(FDR).

5.5.3 Inhibition of Type-I PRMTs reduces fuel flexibility in SkOV3 mitochondria

From integrating proteomics and metabolomics datasets, we identified the TCA cycle as one of the top pathways that is impacted by Type-I PRMT inhibition. To understand the differential fuel utilisation (glucose, glutamine and fatty acid) and flexibility, we carried out a seahorse fuel flexibility test at the basal level and upon MS023 treatment. The Seahorse XF Fuel Flexibility test measures a cell's reliance on and capacity to use the three main mitochondrial fuel pathways—glucose oxidation, glutamine oxidation, and fatty acid oxidation—by sequentially blocking each pathway with specific small-molecule inhibitors. (UK5099 for glucose oxidation, BPTES for glutamine oxidation, and etomoxir for fatty acid oxidation). Fuel dependency is determined by decreased oxygen consumption rate (OCR) after acute inhibition of a particular pathway.

In contrast, fuel capacity is evaluated by the potential increase in OCR when alternative pathways are blocked, showing the cell's ability to adapt its substrate use. In chemoresistant cells, the flexibility (=capacity-dependency) or rigidity of fuel use can reveal metabolic rewiring strategies that support survival under stress. Since SkOV3 cells lacked a sensitive comparator, we utilised the Seahorse fuel flexibility test to investigate whether inhibition of protein arginine methylation—by blocking type I protein arginine methyltransferases (PRMTs)—affects mitochondrial fuel utilisation.

At baseline, SkOV3 cells demonstrated the most significant reliance on glucose (Glc) as an energy source, followed by glutamine (Gln) and, to a lesser extent, fatty acids (FA) (**Figure 34A**). Their mitochondrial fuel-burning capacity exhibited the same hierarchy, with glucose utilisation being the most robust, followed by glutamine and fatty acids (**Figure 34B**). Treatment with MS023 did not substantially alter glucose dependency; however, it increased the reliance on glutamine and fatty acids for supporting mitochondrial respiration (**Figure 34A**). Notably, MS023 markedly reduced the capacity of these cells to oxidise glucose and fatty acids, while leaving their capacity to utilise glutamine largely unaffected (**Figure 34B**). Furthermore, MS023 treatment diminished the metabolic flexibility of SkOV3 cells for all three substrates tested, indicating a reduced ability to switch between fuel sources when the preferred substrate is limited or unavailable (**Figure 34C**).

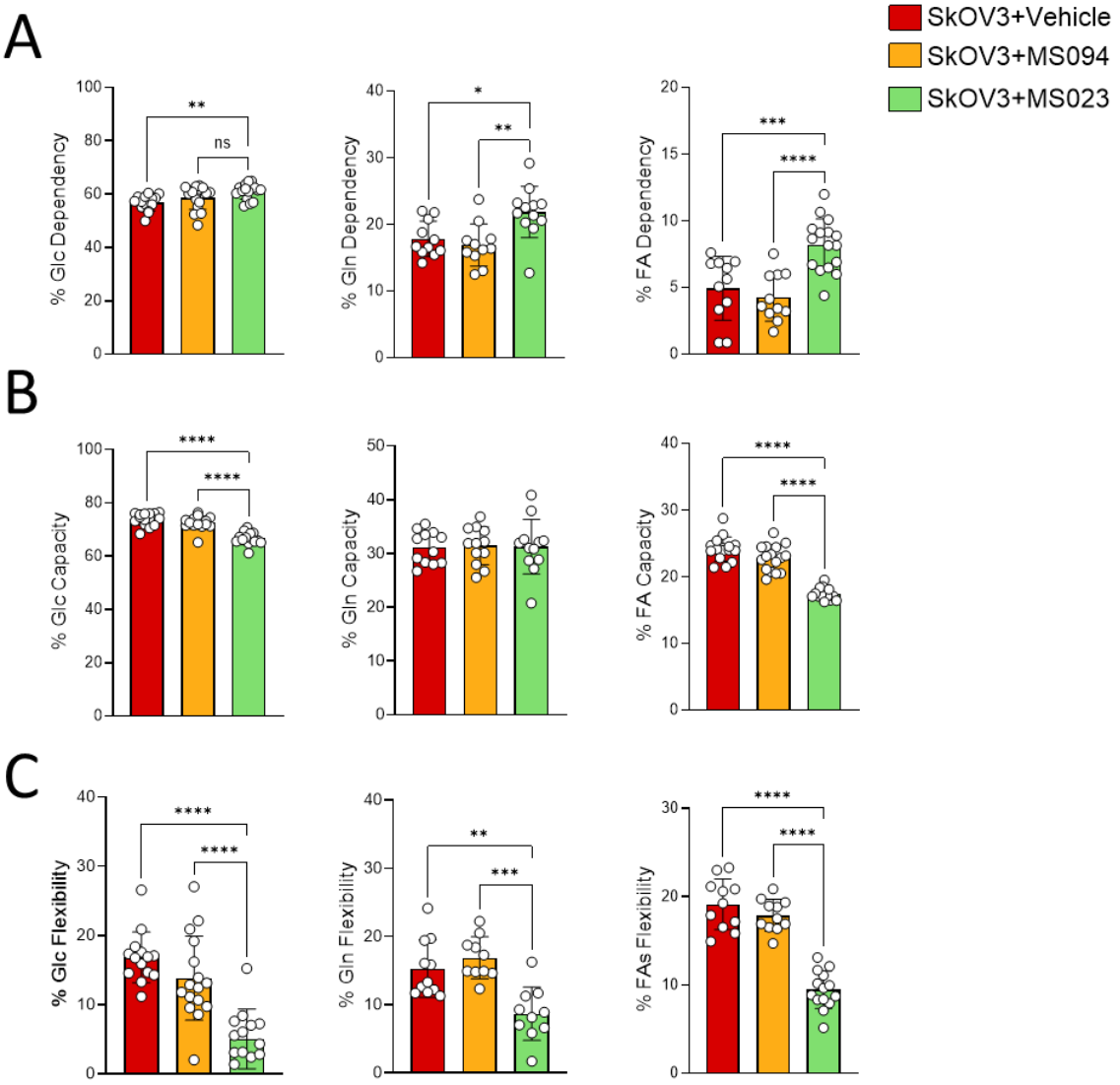

Figure 34: Mitochondrial fuel dependency, capacity, and flexibility in SkOV3 cells following MS023 treatment

The Seahorse XF Mito Fuel Flex Test was performed to assess the reliance of mitochondrial respiration on glucose (Glc), glutamine (Gln), and fatty acids (FA) in control and MS023-treated SkOV3 cells. (**A**) Fuel dependency, defined as the decrease in oxygen consumption rate (OCR) upon inhibition of the pathway-specific entry point for each fuel, indicates the extent to which cells rely on that substrate under basal conditions. (**B**) Fuel capacity is defined as the maximum potential utilisation of each substrate when alternative pathways are blocked. (**C**) Fuel flexibility, calculated as the difference between capacity and dependency, reflects the ability of the cells to adapt to changes in fuel availability. Data represent mean ± SD from one representative experiment (n=2). Statistical significance was determined by one-way ANOVA with Tukey's post-hoc test, $p < 0.05$, $p < 0.01$, $p < 0.001$.

5.6 R-methyl-proteomics profiling of mitochondria identifies candidates linking R-methylation and mitochondrial metabolism and function

The phenotypic assays and quantitative molecular analyses conducted suggested that dynamic R-methylation of proteins linked to mitochondrial dynamics and function could be responsible for the increased mitochondrial respiration, membrane potential, reprogrammed redox state, and energy production observed in chemoresistant EOC cells. Therefore, we aimed to investigate the presence and extent of protein R-methylation within the mitochondrial compartment, an aspect that has not been systematically examined at single-site resolution in human cells (Małecki, Davydova and Falnes, 2022).

5.6.1 Setup of the workflow for mitochondrial R-methyl-proteomics analysis

To characterise R-methylation of mitochondrial proteins, we optimised a biochemical and analytical mass spectrometry (MS)-based workflow, initially on HeLa S3 cells and then on SkOV3 cells. This workflow allowed us to identify high-confidence methylation from crude mitochondrial fractions. Specifically, we used the heavy-methyl SILAC (hmSILAC) metabolic labelling strategy (Ong, Mittler and Mann, 2004) (**Figure 35A-B**), which enables high-confidence identification of *in vivo*, enzymatically incorporated methylation sites on proteins. The hm-SILAC is a metabolic labelling strategy where cells are grown in either heavy or light methionine since methionine is the precursor of the methyl-donor SAM. Therefore, heavy cells produce isotopically heavy labelled SAM and then protein methyltransferases transfer the heavy methyl groups to protein substrates. When a mixture of proteins from cells fully incorporated hmSILAC labelled cells is analysed by MS, the peptides bearing an enzymatically incorporated methylation will present a peak doublet in the full spectrum (MS1). Whereas, the false positives, which are derived by chemical artefact or amino acid substitutions producing delta masses (Δm) isobaric with methylations, do not contain the doublet. Thus, this approach allows for the identification of true methylations, which can be distinguished from isobaric artefacts with high confidence (Ong, Mittler and Mann, 2004). Our group has already implemented this strategy in several previous projects (Bremang *et al.*, 2013; Fong *et al.*, 2019; Musiani *et al.*, 2019; Maniaci *et al.*, 2021; Massignani, Maniaci and Bonaldi, 2023) that led to the identification of novel R-methylation sites and to the release of PrometheusDB, the largest database of high-confidence, orthogonally validated methyl-sites in human cells (Massignani *et al.*, 2022). We combined this approach with biochemical enrichment of mitochondria to overcome the lower representation of less abundant mitochondrial proteins in our datasets compared to highly abundant histones and cytosolic proteins. Light (Met0) and heavy (Met4) labelled cells were mixed

1:1, and mitochondria were enriched with a differential centrifugation method using buffers composed of sucrose and mannitol (Clayton and Shadel, 2014; Alberio *et al.*, 2017; Afanasyeva *et al.*, 2018). The mitochondria-enriched cellular fraction was desalted using C18 raisins after trypsin digestion. Next, we added a step of affinity enrichment of the methylated peptides using a panel of anti-pan-methyl antibodies prior to MS analysis to overcome the sub-stoichiometric nature of PTMs (R-methylation in this context). Overall, this workflow allowed us to overcome the low abundance of mitochondrial proteins and the sub-stoichiometric nature of R-methylated peptides (**Figure 35C**).

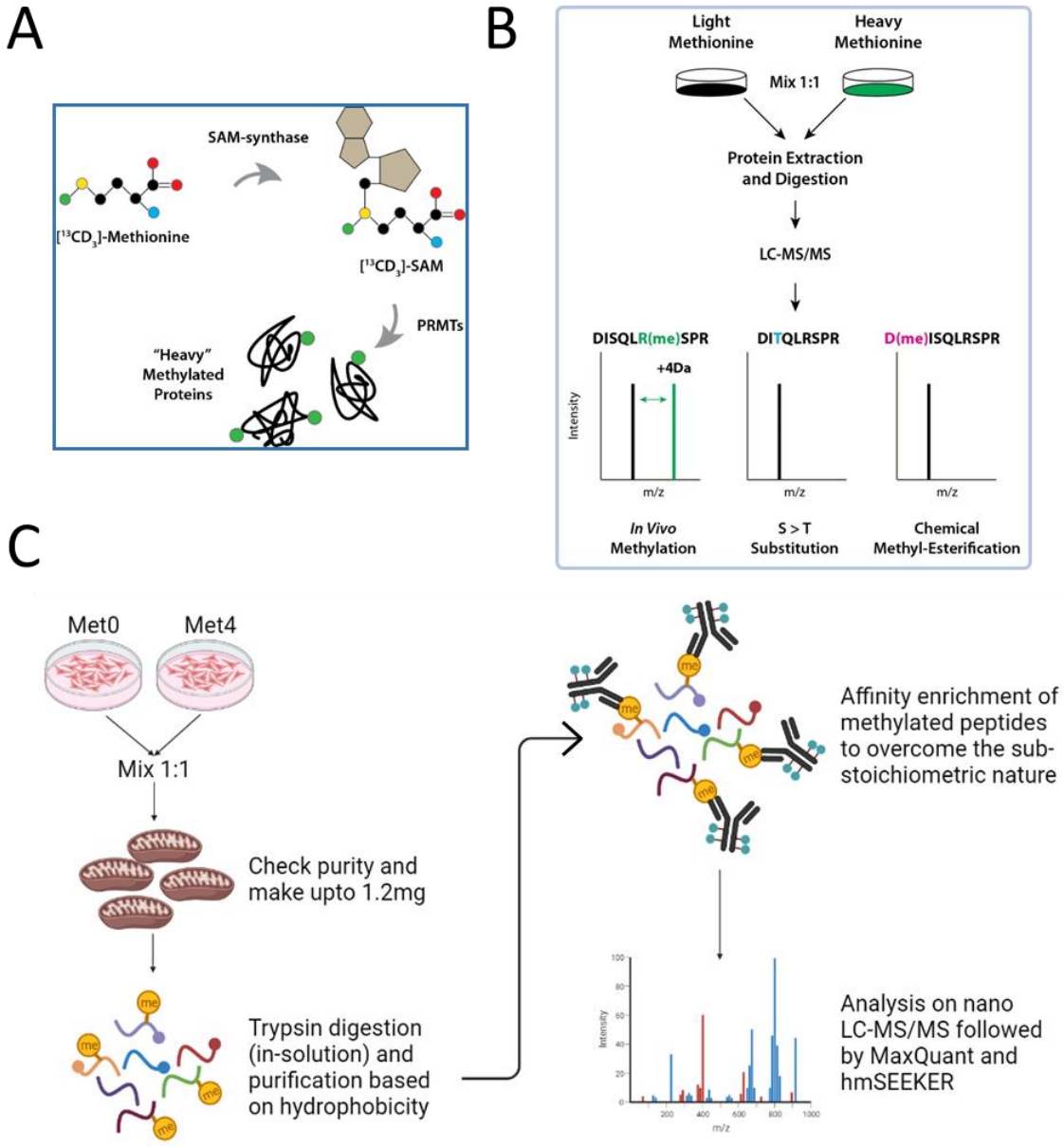

Figure 35: Principle and final workflow of mitochondrial methylproteomics
(**A**) hm-SILAC is a metabolic labelling strategy where cells are grown in the presence of either heavy or light methionine. Because methionine is the precursor of the methyl-donor SAM. Therefore, heavy cells produce heavy SAM and then methyltransferases transfer the heavy methyl groups to proteins.

(**B**) When a mixture of heavy and light is analysed by MS, methyl-peptides form doublets while false positives do not, so that true methylations can be distinguished from isobaric artefacts. (**C**) light (Met0) and heavy (Met4) labelled cells were mixed 1:1, and mitochondria were enriched biochemically from fresh cell pellets.

Heavy methionine-labelled SkOV3 cells were trypsin-digested, purified, and analysed by LC-MS/MS to evaluate the incorporation of heavy methionine at the peptide level. We achieved 95% full incorporation (**Figure 36A**), and among the partially incorporated peptides, an incorporation of 97.8% was observed (**Figure 36B**). This test demonstrated a near-complete labelling, with a global mean approaching to 1.0. The high incorporation efficiency ensured an accurate isotope-based quantification by minimising mixed isotope envelopes (overlapping peaks resulted from incomplete labelling, giving rise to inaccurate quantification of delta masses) and incomplete labelling artefacts (incorrect ratios produced from heavy and light peptide pairs).

To verify subcellular fractionation of mitochondria, we assessed the quality and reproducibility of mitochondrial enrichment across independent preparations by immunoblotting and compared these fractions with whole-cell extracts (**Figure 36C**). Mitochondrial ETC subunits (mitochondrial marker) were enriched, whereas H3 and H4 (nuclear marker) and vinculin (cytosol marker) were depleted in the mitochondrial fraction compared to the whole-cell extract. The blots confirmed consistent enrichment of mitochondrial material relative to the total lysate, even on a large-scale preparation of 1.2mg, validating the fractions used for proteomic analysis.

The same mitochondrial fractions and whole cell extracts were trypsin-digested, analysed by LC–MS/MS acquired through data-dependent analysis (DDA, see introduction) and processed by MaxQuant software. Intensity-based absolute quantification (IBAQ) measures the absolute abundance of proteins in a sample. When mitochondrial proteins (low-abundance) and histones (high-abundance) were ranked based on their IBAQ values, a clear upward shift of mitochondrial proteins was observed in the mitochondrial fraction, indicating a relative enrichment compared to the whole-cell extract (**Figure 36D**). The label-free quantification (LFQ) intensities measured from precursor ions in MS1, which indicate relative peptide/protein abundance, were compared between fractions to assess enrichment and coverage depth. In the mitochondrial fraction, there was a rightward shift of mitochondrial proteins and a depletion of non-mitochondrial proteins compared to the whole-cell extract (**Figure 36E**). Overall, these results confirmed the setup with an optimal labelling of the cells for the identification of high-confidence methylation sites on low-abundant mitochondrial proteins.

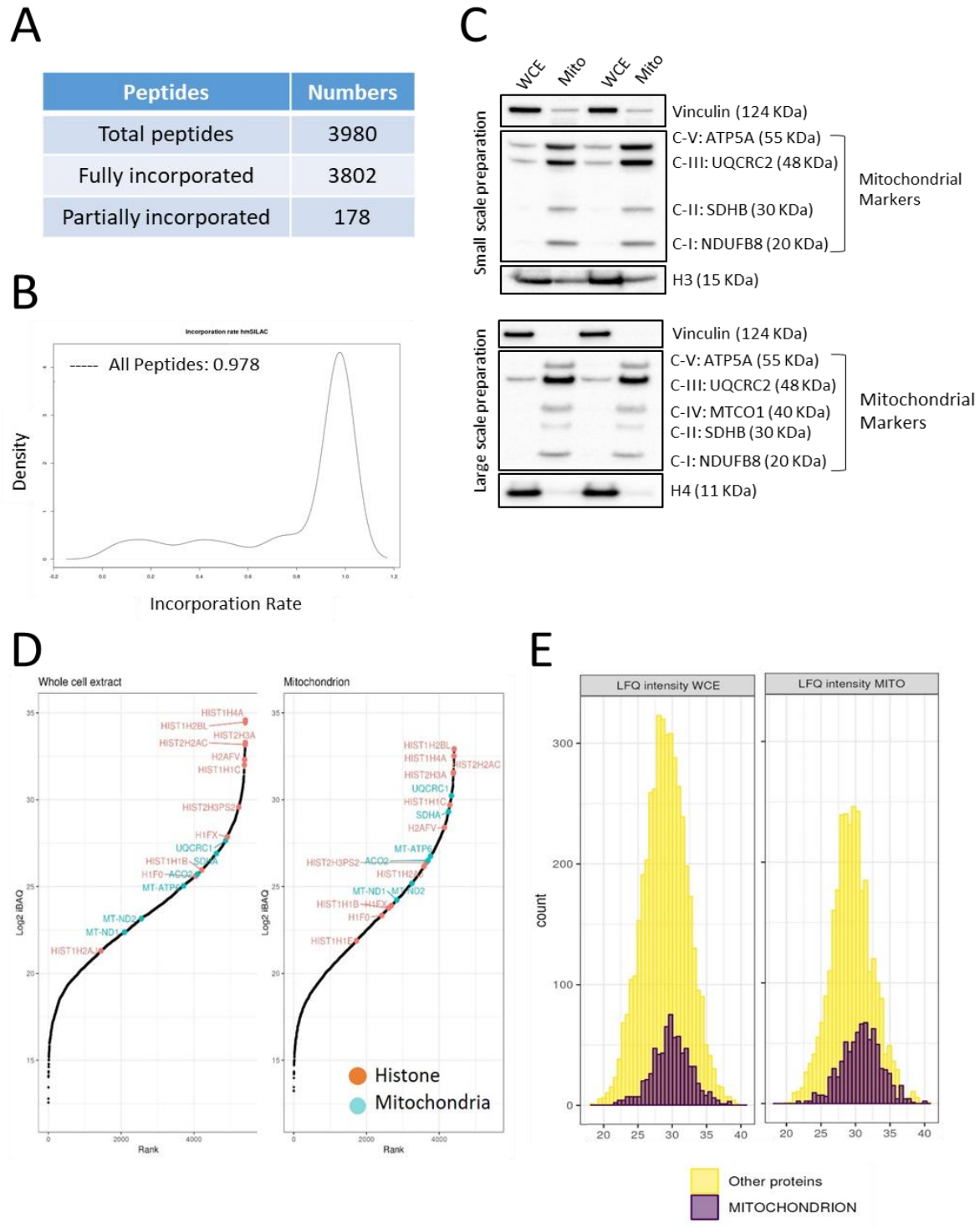

Figure 36: Proteomic analysis of hm-SILAC incorporation and label-free whole-cell and mitochondrial fractions of SkOV3 cells

(**A**) The peptide identification and labelling efficiency summary shows the total, fully incorporated, and partially incorporated peptides detected by LC-MS/MS analysis. (**B**) Distribution of peptide incorporation within partially-incorporated hm-SILAC-labelled samples, with a mean incorporation rate of 0.978, indicating near-complete labelling. (**C**) Representative immunoblot of different batches of small-scale and large-scale mitochondrial preparation. Fraction quality was assessed by comparing ETC proteins (mitochondrial marker), H3 and H4 (nuclear marker) and vinculin (cytosol marker). (**D**) Ranked abundance plots of proteins identified in whole-cell extracts

(WCE) and mitochondria-enriched fraction, highlighting the relative abundance of histone (orange) and mitochondrial (cyan) proteins. (**E**) LFQ intensity distributions for WCE and mitochondrial fractions, showing distinct abundance profiles of mitochondrial proteins (purple) compared to all other proteins (yellow).

5.5.2 R-methylated mitochondrial proteins are involved in protein synthesis, metabolism and apoptosis

The MS raw data from the acquisition of putative mitochondrial methyl peptide samples were analysed with MaxQuant-hmSEEKER and FragPipe-MethylQuant. Search engines, such as Andromeda (for Maxquant) or MSFragger (for FragPipe), carried out heavy and light peptide identification. Then, hmSEEKER (Massignani *et al.*, 2019) was used for peptide pair matching from MaxQuant output, whereas MethylQuant (Tay *et al.*, 2018) was used for FragPipe output. For both software, the minimum criteria were matched for high-confidence methyl sites and mitochondrial proteins were identified by intersecting the list of proteins with Mitocarta 3.0 (*MitoCarta3.0: An Inventory of Mammalian Mitochondrial Proteins and Pathways | Broad Institute*; Calvo, Clauser and Mootha, 2016).

Overall, this mitochondrial-focused methyl-proteomics analysis led to the identification of 17 high-confidence sites on 15 mitochondrial proteins involved in mitochondrial transcription, translation, oxidative phosphorylation, metabolism, and apoptosis, listed in **Table 5**, which describes R-methylation sites derived from both SkOV3 and HeLa S3 cell lines at the steady state.

Table 5: R-methylated mitochondrial proteins

Protein	Gene	Mod.	Cell Line	Analysis set
Putative GTP-binding protein 7	GTPBP7	242me1	HeLaS3	MaxQ_ hmSEEKER
Malonyl-CoA-acyl carrier protein transacylase, mitochondrial	MCAT	340me1	HeLaS3	MaxQ_ hmSEEKER
Acyl-CoA dehydrogenase family member 11	ACAD11	619me1	HeLaS3	MaxQ_ hmSEEKER
Dimethyladenosine transferase 2, mitochondrial	TFB2M	198me2	HeLaS3	MaxQ_ hmSEEKER
Putative GTP-binding protein 6	GTPBP6	55me1	HeLaS3	Both
MAPK-regulated corepressor-interacting protein 2	MCRIP2	65me1	HeLaS3 SkOV3	Both

L-xylulose reductase	DCXR	21me1	HeLaS3	Both
ATP synthase subunit alpha, mitochondrial	ATP5F1A	204me1	HeLaS3 SkOV3	Both
Bcl2-associated agonist of cell death	BAD	161me1	HeLaS3 SkOV3	Both
NADH dehydrogenase [ubiquinone] iron-sulfur protein 2, mitochondrial	NDUFS2	118me2	HeLaS3 SkOV3	Both
Dehydrogenase/reductase SDR family member 1	DHRS1	21me1	HeLaS3	Both
MAPK-regulated corepressor-interacting protein 2	MCRIP2	35me1	HeLaS3	FP_MethylQ
Mitochondrial import receptor subunit TOM70	TOMM70	71me1	HeLaS3 SkOV3	FP_MethylQ
Putative GTP-binding protein 6	GTPBP6	242me1	HeLaS3	FP_MethylQ
Pitrilysin Metallopeptidase 1	PITRM1	12me1	SkOV3	MaxQ_ hmSEEKER
NADH dehydrogenase [ubiquinone] iron-sulfur protein 2, mitochondrial	NDUFV3	182me1	SkOV3	FP_MethylQ
SRA Stem-Loop Interacting RNA Binding Protein	SLIRP	7me1	SkOV3	FP_MethylQ
Peroxiredoxin-6	PRDX6	9me1	HeLaS3	MaxQ_MethlQ
MAPK-regulated corepressor-interacting protein 2	MCRIP2	19me1	HeLaS3	MaxQ_MethlQ
MAPK-regulated corepressor-interacting protein 2	MCRIP2	24me1	HeLaS3	MaxQ_MethlQ
Protein angel homolog 2	ANGEL2	11me1	HeLaS3	MaxQ_MethlQ
Carbamoyl-phosphate synthase [ammonia], mitochondrial	CPS1	4me1	HeLaS3	MaxQ_MethlQ

MAPK-regulated corepressor-interacting protein 2	MCRIP2	2me1	HeLaS3	MaxQ_MethlQ
Ribose-5-phosphate isomerase	RPIA	42me1	HeLaS3	Both

Interestingly, several of the identified methylated proteins are central to maintaining mitochondrial gene expression and respiratory capacity. GTPBP7 (MTG2), a GTP-binding protein essential for mitoribosome assembly and translation, may influence the efficiency of mitochondrial protein synthesis, thereby modulating oxidative phosphorylation (OXPHOS) output in chemoresistant cells (Chandrasekaran *et al.*, 2021; Maiti *et al.*, 2021). TFB2M, a transcription factor required for mtDNA transcription initiation (Falkenberg *et al.*, 2002; Ramachandran *et al.*, 2016), represents a key node where methylation could alter mitochondrial transcript abundance, consistent with observations in SkOV3 cells where mitochondrial transcripts were post-transcriptionally regulated after cisplatin exposure. GTPBP6, involved in ribosome recycling, could impact translation fidelity and mitoribosome turnover (Lavdovskaia *et al.*, 2020), ultimately affecting mitochondrial ETC levels.

Remarkably, R-methylation was also detected on enzymes directly involved in mitochondrial metabolic output: MCAT catalyses a key step in mitochondrial fatty acid biosynthesis, necessary for lipoic acid production and pyruvate dehydrogenase function, linking PRMT activity to metabolic rewiring and NAD^+/NADH shifts observed in resistant cells. ACAD11, a very-long-chain acyl-CoA dehydrogenase, contributes to β-oxidation and lipid catabolism, potentially enhancing fuel flexibility. NDUFS2, a core subunit of Complex I, is central to NADH oxidation and electron transport; R-methylation could influence respiratory efficiency and reactive oxygen species (ROS) handling, aligning with the observed low NAD^+/NADH ratio. ATPF1A, the catalytic α-subunit of ATP synthase (Complex V), may serve as a methylation-sensitive regulator of mitochondrial ATP output and bioenergetic adaptation.

Proteins with roles in mitochondrial apoptosis and stress sensing were also identified as methylated: BAD, a pro-apoptotic Bcl-2 family member, regulates mitochondrial outer membrane permeabilisation; methylation could alter its interaction with anti-apoptotic proteins, modulating the balance between cell death and survival in chemoresistance. TOMM70, a mitochondrial outer membrane import receptor, also functions as a stress sensor and can interface with mitophagy/autophagy pathways, consistent with prior observations of altered p62 and LC3 dynamics.

Lastly, a subset of the R-methylated proteins identified connects cytosolic metabolism with mitochondrial function. DCXR, a dicarbonyl/L-xylulose reductase, participates in carbohydrate and lipid redox metabolism, potentially influencing oxidative stress management. RPIA, a ribose-5-phosphate isomerase of the pentose phosphate pathway, is essential for NADPH generation and fits with the high $NADP^+$/NADPH ratio detected in resistant cells. DHRS1, a dehydrogenase/reductase, may contribute to lipid redox homeostasis. MCRIP2, a modulator of transcriptional repression, could integrate stress responses with mitochondrial metabolic adaptation.

Overall, this analysis led to the annotation of a small number of R-methyl sites on mitochondrial proteins, and the pipeline needs to be further improved to increase the depth of this dataset. The results achieved so far are, *per se*, very interesting and allowed us to infer that Type-I PRMT–mediated ADMA seems to be a possible regulator of processes such as mitochondrial biogenesis, metabolic flexibility, and oxidative stress buffering. Whether this is directly and/or mechanistically linked to the onset and sustain of chemoresistance in these cells must be validated with *ad hoc* experiment.

6. Discussion

In epithelial ovarian cancer (EOC), the onset of resistance to platinum-based drugs remains a major clinical hurdle, often resulting in tumour relapse and reduced survival rates. On one hand, mitochondrial role in driving chemoresistance is a well-established fact (**introduction 2.3.1**), while on the other, protein R-methylation dynamics – even though a relatively new area in cell biology and signalling – has been shown to underpin chemoresistance in several cancer types, including EOC (**introduction 2.4.2**). However, the direct and mechanistic link between these two cellular processes has not been investigated in depth and fully resolved. Existing literature presents scattered evidence of PRMTs, mainly CARM1/PRMT4 and PRMT3, reprogramming glycolysis and pentose phosphate pathway, thus contributing to cancer development and progression (**introduction 2.5**). Interestingly, the lack of studies elucidating PRMTs' role in chemoresistance by modulating mitochondrial function prompted us to fill this gap in the knowledge in this PhD project, in which we aimed to discover a novel molecular mechanism functionally linking protein R-methylation and mitochondrial metabolic reprogramming in their contribution to the onset of chemoresistance in EOC. As discussed in the hypothesis (**hypothesis 3.2**), we postulated that platinum-mediated genotoxic stress influences PRMT-mediated R-methylation of key mitochondrial proteins, thereby regulating mitochondrial metabolism.

As outlined in the preliminary results, integration of proteomic and transcriptomic datasets from SkOV3 cells exposed to 20μM cisplatin for 24h revealed the upregulation of multiple mitochondrial genes (**Figure 9**). Although in Musiani et al. 2020 we described a mechanism of chemoresistance in SkOV3 cells under acute treatment conditions, this approach was insufficient to capture the adaptive processes underlying relapse and acquired drug resistance. To address this limitation, we established *in-house* a resistant A2780R model derived from the parental A2780S line (**Figure 11**). This model enabled us to evaluate the capacity of type I PRMT inhibition to restore platinum sensitivity in resistance-induced cells while directly comparing them with their sensitive counterpart. Increased mitochondrial OCR (**Figure 12B-D**) and a hyperfused mitochondrial network (**Figure 13**) in A2780R cells confirmed the validity of this model system to investigate our working model. SkOV3 cells, an established chemoresistant EOC model used in Bonaldi's group, were also included to benchmark the findings observed in A2780R.

Since no specific PRMT isoform has been exclusively implicated in regulating the mitochondrial R-methyl proteome (Małecki, Davydova and Falnes, 2022), we selected the pan–type I PRMT inhibitor MS023, given the predominance of ADMA relative to SDMA/MMA in the global R-methyl proteome. A 48h pretreatment with 10μM MS023 significantly sensitised

A2780R cells, resulting in a 56% reduction in their IC_{50} (**Figure 14A**). Concomitantly, MS023 treatment reduced the OCR of A2780R cells, restoring it to levels comparable to A2780S (**Figure 15A**). A similar mitostress test profile in SkOV3 cells confirmed their strong dependence on mitochondrial OXPHOS, which was likewise attenuated by MS023 treatment (**Figure 28A**). Furthermore, MS023 decreased mitochondrial membrane potential and disrupted the hyperfused mitochondrial network in A2780R cells (**Figures 18 and 19A**). The combined reduction in IC_{50} and mitochondrial functionality in A2780R cells provided strong support for our hypothesis and justified a deeper mechanistic investigation.

To investigate the major biological processes regulated and the cellular components affected by the inhibition of type I PRMTs, we measured global protein-level alterations induced by the inhibitor MS023 using MS-based untargeted proteomics. In both MS023-treated A2780R and SkOV3 cell lines, gene ontology analysis of dysregulated proteins revealed a coordinated downregulation of nuclear processes and upregulation of cytosolic processes (**Figures 22 and 31**). Among the downregulated categories were terms related to DNA replication and cell cycle regulation, suggesting an impaired capacity for DNA repair and proliferation. Conversely, the upregulated categories included pathways associated with lipid and cholesterol biosynthesis, as well as autophagosome formation. These observations support the notion that inhibition of type I PRMT enzymatic activity promotes protein misfolding/unfolding and organelle dysfunction, thereby necessitating enhanced autophagic clearance. Collectively, the data indicate that pretreatment with MS023 compromises cellular defence against platinum-induced damage, thereby sensitising EOC cells to chemotherapy. Consistent with this, we detected induction of mitophagy in both A2780R and SkOV3 cells, which provides a mechanistic explanation for the reduction in mitochondrial OCR observed upon MS023 exposure (**Figures 20 and 29**). However, no significant decrease in mtDNA copy number was detected (**Figures 16 and 28B**), despite overall noisy results due to high variability across biological replicates. In this perspective, future studies should employ more precise methodologies, such as, digital droplet PCR for robust quantification of mtDNA content.

Next, the targeted metabolomic analysis carried out allowed us to gain a deeper understanding of the metabolic adaptations in A2780R cells and highlighted enhanced amino acid utilisation, nucleotide synthesis (**Figure 23**), TCA cycle, and antioxidant response (**Figure 24**). These principal adaptation axes in A2780R cells were blunted by MS023, as it seemed to topple the redox balance and induce mitochondrial dysfunctionality (**Figure 25**). In SkOV3 cells, however, MS023 only reduced the amino acid catabolism significantly and showed a similar downward trend in antioxidant response (**Figure 32**). However, these results emerged out of a

steady-state metabolomics experiment, which did not provide us information about metabolic fluxes in these cells. Future experiments focusing on consumption of amino acids and release of metabolites as well as tracing experiments over time will be crucial to derive kinetic information.

Notably, in A2780R cells, we observed an increase in all TCA cycle metabolites, except for α-ketoglutarate and acetyl CoA (**Figure 24C**). On the one hand, Acetyl CoA acts as an epigenetic regulator among many other biological processes that provides acetyl groups for histone acetylation; on the other hand, α-ketoglutarate is a well-known co-factor for JMJ-domain containing histone and DNA demethylases. Together, a significant reduction of these two metabolites indicates potential acetylation and demethylation events on histone residues, contributing to chromatin remodelling and accessibility that have played a part as A2780S cells acquired platinum-resistance. Interestingly, MS023 treatment significantly restores the levels of α-ketoglutarate in A2780R cells (**Figure 37**).

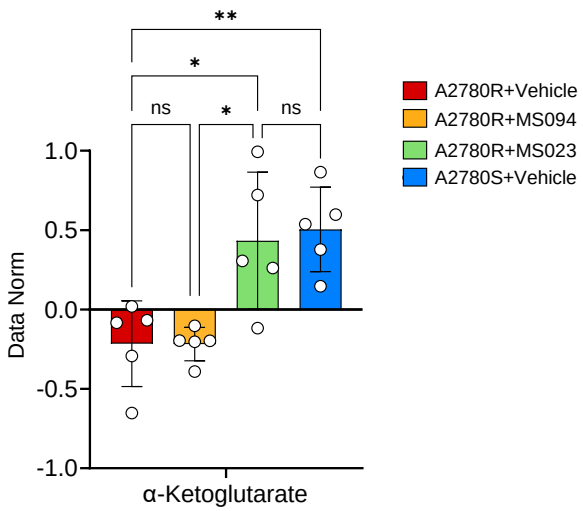

Figure 37: MS023 restores α-ketoglutarate levels in A2780R cells
The relative abundance of α-ketoglutarate (values normalised over median) shows that MS023 restores the level of this metabolite in A2780R cells, making it comparable to the levels of A2780S. Bar graphs represent mean ± SD, with individual biological replicates shown as dots (n=5). Statistical analysis *was performed using one-way ANOVA* test, where **=p<0.01 and *=p<0.05

The integration of proteomics and metabolomic datasets showed that MS023, A2780R cells, impacts redox and nitrogen metabolism (glutathione metabolism, arginine biosynthesis) (**Figure 26**), while in SkOV3 cells, it demonstrates a stronger lipid/isoprenoid biosynthetic signature (steroid biosynthesis, terpenoid backbone biosynthesis) (**Figure 33**). The differences observed may reflect distinct cell line–specific strategies to adapt to chemotherapy-induced stress. However, in both resistant cell lines, the pharmacological inhibition of Type-I PRMTs was found to regulate the reprogramming of central carbon metabolism (TCA cycle,

alanine/aspartate/glutamate metabolism) and nucleotide metabolism (pyrimidine metabolism), which reflects shared requirements for energy, biosynthesis, and DNA repair in inherent and adaptive chemoresistance.

Steady-state metabolomics analysis in A2780R cells prompted isotope-tracing experiments using ^{13}C-labelled glutamine and ^{13}C-labelled serine to determine their relative contributions to glutathione synthesis. These analyses revealed that A2780R cells preferentially utilise *de novo* synthesised serine, rather than glutamine, for glutathione production (**Figures 27A and 27D**). Treatment with MS023 decreased the incorporation of unlabelled serine (M0, representing de novo synthesis) into glutathione, while increasing the incorporation of M2-labelled serine (via glycine) into glutathione (**Figure 27C**). Notably, MS023 treatment also reduced M2-labelled glycine abundance in A2780R cells to levels comparable with those in A2780S (**Figure 27E**). Together, inhibition of type-I PRMTs results in either a reduced conversion of serine to glycine and/or increased glycine incorporation into glutathione. Mechanistically, this phenotype could arise from decreased activity of serine hydroxymethyltransferase (SHMT, which converts serine to glycine) or enhanced activity of glutathione synthetase (GSS, which catalyses glutathione synthesis from γ-glutamylcysteine and glycine) (**Figure 38**). Therefore, it is plausible that SHMT and/or GSS may represent a potential direct target of type-I PRMTs. Although the R-methyl-proteome of mitochondria from A2780S and A2780R cells remains to be acquired, future studies will escalate the mechanistic investigation by immunoprecipitation of SHMT and GSS, followed by MS-based mapping of potential R-methylation sites. However, it should be noted that the percentage of $^{13}C_5$-labelled glutamine was about 10% among the total glutamine pool, which requires further consideration. This finding was somewhat unexpected; especially since serine was more utilised than glutamine. This aspect should be further validated by ad hoc experiments such as $^{13}C_6$-glucose tracing experiment.

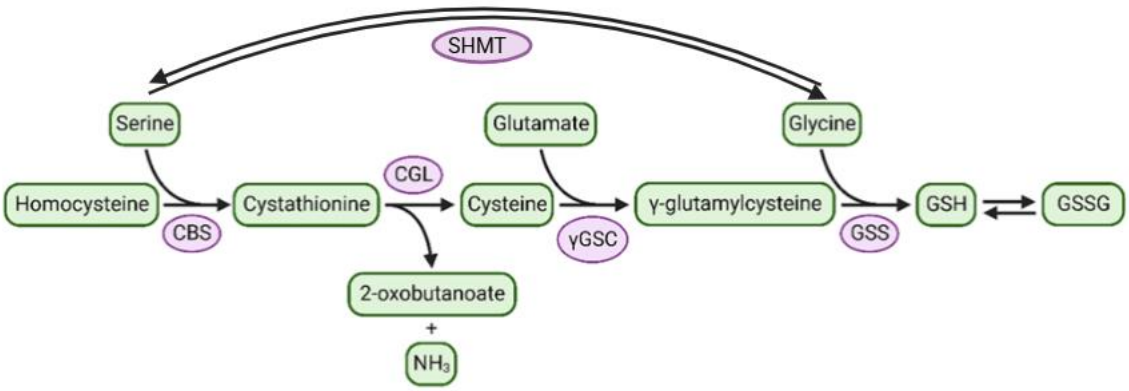

Figure 38: Glutathione synthesis pathway

Serine contributes to glutathione (GSH) synthesis either directly via serine hydroxymethyltransferase (SHMT)–mediated conversion to glycine or indirectly through the transsulfuration pathway. In the latter, serine combines with homocysteine to form cystathionine via cystathionine β-synthase (CBS), which is subsequently cleaved by cystathionine γ-lyase (CGL) to generate cysteine. Cysteine and glutamate are ligated by γ-glutamylcysteine synthetase (γGCS) to form γ-glutamylcysteine, which is then conjugated with glycine by glutathione synthetase (GSS) to produce reduced glutathione (GSH). Oxidised glutathione (GSSG) is formed upon oxidation of GSH. Enzymes are shown in purple and metabolites in green. Figure adapted from (Safrhansova, Hlozkova and Starkova, 2022)

In SkOV3 cells, MS023 reduced fuel flexibility across all three major substrates—glucose, glutamine, and fatty acids—feeding into the TCA cycle, which emerged as the central metabolic node affected in the integrative analysis (**Figure 33**). These results demonstrate that MS023 exerts both shared and cell line–specific metabolic effects in A2780R and SkOV3 cells. In both models, type-I PRMT inhibition suppressed amino acid catabolism and disrupted mitochondrial metabolism. However, the downstream consequences seem to diverge: while in A2780R cells the inhibition impaired redox buffering capacity and depleted glutathione through perturbation of serine catabolism, in SkOV3 cells the same treatment/perturbation induced TCA cycle stalling and reduced metabolic plasticity across fuel sources. These findings underscore both conserved and context-dependent functions of type-I PRMT activity in sustaining metabolic pathways across distinct EOC chemoresistance models.

The acquisition of the R-methyl-proteome of mitochondria was a crucial point of this study, holding the potential to mechanistically link the metabolic reprogramming to the R-methylation state of important mitochondrial proteins, which could ultimately sustain chemoresistance. Theoretically, as a proof of concept, R-to-K mutation of a candidate methyl-site of potential target proteins would maintain the positive charge of the residue but would mimic a lack of R-methylation. Conversely, R-to-A mutation would mimic a methylated site. This mutational analysis of specific sites on target proteins could be useful in understanding the impact of R-methylation on the orchestration of metabolic rewiring. With this idea in mind, we set up the mitochondrial methyl-proteomics workflow first in HeLaS3 cells and then in SkOV3 cells. This workflow posed several challenges: since the affinity enrichment of R-methylated peptides required more than 1mg starting material, we had to optimise the mitochondria enrichment protocol trying to find the best compromise between yields versus purity of this organelle fraction. However, even though mitochondrial proteins were enriched in the fraction, our methylproteome was masked mainly by more abundant and/or heavily R-modified proteins, such as histones and RNA-binding proteins.

Additionally, the antibody used for enrichment by cell signalling technologies is developed to recognise the classical RG/RGG motif on peptides, where R-methylation usually occurs. However, we cannot exclude the possibility that mitochondrial proteins might have their own unique motif for R-methylation. Currently, we are trying to optimise alternative workflows to gain greater depth. We are currently trying to develop a negative-enrichment strategy to enrich for R-methylated peptides based on a previously described strategy (Sun *et al.*, 2025) and purify intact mitochondria by rapid immunopurification by leveraging the stable cell lines with an HA-tag fused with mitochondrial outer membrane protein 25 (3xHA-OMP25) (Chen *et al.*, 2016).

Even though we could not achieve a desirable depth into the R-methylproteome of mitochondria, the protocol setup to date allowed us to uncover a list of very interesting candidate proteins that will be further investigated. For instance, we discovered a novel R-methyl site on TFB2M at R198 residue. To the best of our knowledge, this site has not been annotated in any PTM repositories. Methylation of R198 is particularly interesting to follow up on due to its possible functional impact since this site is known to interact with non-template DNA during mitochondrial DNA transcription (Hillen *et al.*, 2017).

In this project, so far, we have tested our hypothesis from only one perspective, e.g. that the activity of PRMTs might regulate mitochondrial metabolic activity and function. However, as discussed in **paragraph 4.2** and illustrated in **Figure 10**, we could not rule out the possibility that the directionality of this hypothesis may be inverted. In other words, instead of PRMTs regulating mitochondrial metabolism, it is also possible that the availability of S-adenosyl methionine (SAM) influences PRMT activity. SAM is the primary methyl group donor in all cellular methylation events, and its levels are controlled by the methionine cycle. Thus, fluctuations in SAM abundance could directly modulate PRMT function.

Even though we have not yet carried out *ad hoc* experiments to address this aspect, in the steady-state metabolomics dataset, we have observed that the SAM/SAH ratio was significantly lower in A2780R cells (**Figure 39B**), indicating an increased utilisation of SAM in the resistant cells. This utilisation of SAM is due to DNA, RNA and protein methylation, and does not necessarily imply an increased R-methylation. Interestingly, MS023 treatment increased the SAM and SAH levels in the A2780R cell line (**Figure 39B**). Upstream of SAM, we observed an accumulation of methionine (**Figure 39B**) upon MS023 treatment. Platinum resistance-induced ovarian cancer cells are known to have reduced S-methyl-5'-thioadenosine phosphorylase (MTAP) deficiency (Ding *et al.*, 2017) that regenerates methionine from the polyamine pathway (**Figure 39A**). In the proteomics data, we noticed that A2780R cells also suffer a loss of MTAP, which was

not rescued by MS023 treatment (**Figure 39C**). These indications compel us to hypothesise that the accumulation of methionine in A2780R cells upon MS023 treatment is possibly due to the loss of function in MAT2A. Previously, Enrico Massignani in the Bonaldi's group had identified R264 on MAT2A as a potential R-methyl site, which resides at the interface between the subunits that make up the enzyme's active dimer. The fact that the enzyme responsible for synthesising SAM can be itself methylated at a site important for its catalytic function suggests MAT2A as a potential SAM sensor maintaining a feedback mechanism.

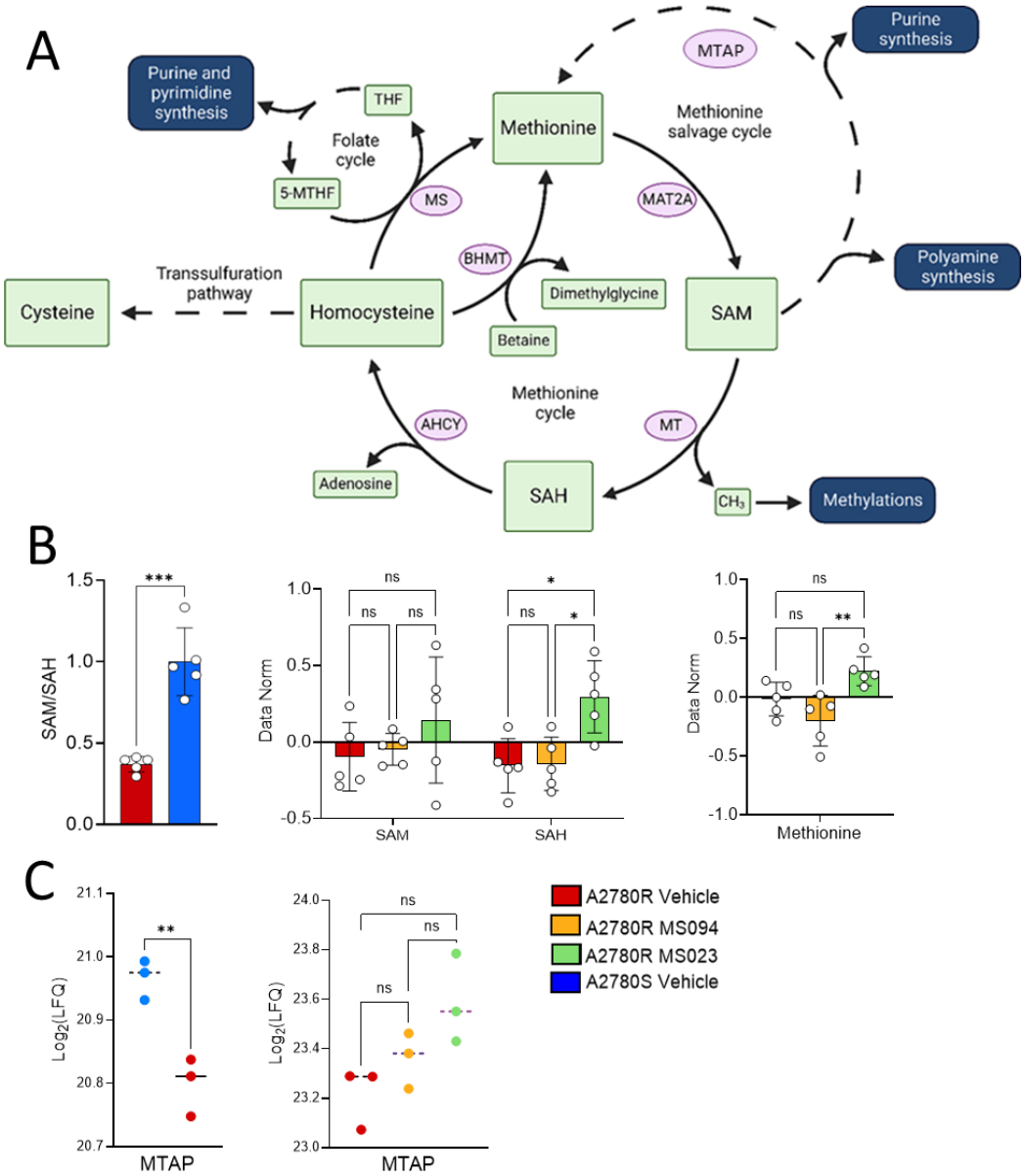

Figure 39: Methionine cycle, impact of MS023 on SAM and status of MTAP
(**A**) Methionine enters the methionine cycle, where methionine adenosyltransferase (MAT2A) catalyses its conversion to S-adenosylmethionine (SAM). SAM is a universal methyl donor in transmethylation reactions, generating S-adenosylhomocysteine (SAH) via methyltransferases (MT). SAH is subsequently hydrolysed to homocysteine by adenosylhomocysteinase (AHCY). Homocysteine can be remethylated to methionine by the enzyme methionine synthase (MS) using

5-methyltetrahydrofolate (5-MTHF) from the folate cycle. Alternatively, homocysteine enters the transsulfuration pathway to generate cysteine. The methionine salvage pathway involving methylthioadenosine phosphorylase (MTAP) recycles methionine. Enzymes are shown in purple, metabolites in green and key biosynthetic outputs in blue. Figure adapted from (Safrhansova, Hlozkova and Starkova, 2022). (**B**) SAM/SAH ratio (normalised over A2780S) and relative abundance (values normalised over median) of SAM, SAH and methionine (n=5). Statistical analysis was performed using Student's *t*-test, or one-way ANOVA test, where ***=$p<0.001$, **=$p<0.01$ and *=$p<0.05$ (**C**) log-transformed label-free quantification (LFQ) values of MTAP (n=3). Bar graphs represent mean ± SD, with individual biological replicates as circles. Statistical analysis was performed using multiple t-test and p-values were corrected with the Benjamini-Hochberg method, where **=$p<0.01$

In conclusion, this study has provided novel insights into the role of type I PRMTs in regulating mitochondrial metabolism and chemoresistance in epithelial ovarian cancer, highlighting how pharmacological inhibition of type I PRMTs can restore platinum sensitivity by impairing mitochondrial function and central carbon metabolism. We uncovered both shared and cell line–specific adaptations in two different cell models of chemoresistant EOC, including perturbations in glutathione synthesis, TCA cycle activity, and methionine/SAM metabolism, which collectively support a model where R-methylation contributes to metabolic reprogramming underlying chemoresistance.

7. Future perspective

The study is still limited by the incomplete characterisation of the mitochondrial R-methylproteome, primarily due to technical challenges, as well as by the lack of direct validation of candidate methylation sites on mitochondrial proteins. Furthermore, the precise contribution of individual PRMT isoforms and the mechanistic feedback between SAM metabolism and PRMT activity remain to be fully dissected. It is crucial to understand the differently methylated proteins between A2780S and A2780R cells, as well as how many of the sites in A2780R cells are dynamically modulated upon MS023. To establish a direct causal relationship between PRMTs and mitochondrial activity, it will be fundamental to overexpress different type-I PRMTs and check if the resistant phenotype as well as mitochondrial function is induced A2780S cells. Future work employing deeper proteomic coverage and site-directed mutagenesis of selected candidate proteins will be critical to systematically dissect the causal relationship between R-methylation, mitochondrial metabolism, and platinum resistance.

7. References

Abeywardana, T. *et al.* (2018) 'CARM1 suppresses de novo serine synthesis by promoting PKM2 activity', *Journal of Biological Chemistry*, 293(39), pp. 15290–15303. doi: 10.1074/JBC.RA118.004512/ATTACHMENT/2B98B2DD-A0F1-42F1-A095-9ECF2758E45A/MMC1.PDF.

Afanasyeva, M. A. *et al.* (2018) 'Isolation of Large Amounts of Highly Pure Mitochondria for "Omics" Studies', *Biochemistry. Biokhimiia*, 83(1), pp. 76–85. doi: 10.1134/S0006297918010108.

Alberio, T. *et al.* (2017) 'Toward the Standardization of Mitochondrial Proteomics: The Italian Mitochondrial Human Proteome Project Initiative', *Journal of proteome research*, 16(12), pp. 4319–4329. doi: 10.1021/ACS.JPROTEOME.7B00350.

Amano, T. *et al.* (2019) 'Abundance of mitochondrial superoxide dismutase is a negative predictive biomarker for endometriosis-associated ovarian cancers', *World Journal of Surgical Oncology*, 17(1), p. 24. doi: 10.1186/S12957-019-1565-0.

Archer, S. L. (2013) 'Mitochondrial Dynamics — Mitochondrial Fission and Fusion in Human Diseases', *New England Journal of Medicine*, 369(23), pp. 2236–2251. doi: 10.1056/NEJMRA1215233,.

Arora, T. *et al.* (2024) 'Epithelial Ovarian Cancer'. Available at: https://www.ncbi.nlm.nih.gov/books/NBK567760/ (Accessed: 20 May 2025).

Bahar, E. *et al.* (2020) 'Establishment of Acquired Cisplatin Resistance in Ovarian Cancer Cell Lines Characterized by Enriched Metastatic Properties with Increased Twist Expression', *International Journal of Molecular Sciences 2020, Vol. 21, Page 7613*, 21(20), p. 7613. doi: 10.3390/IJMS21207613.

Bao, X. *et al.* (2013) 'Overexpression of PRMT5 Promotes Tumor Cell Growth and Is Associated with Poor Disease Prognosis in Epithelial Ovarian Cancer', *Journal of Histochemistry and Cytochemistry*, 61(3), p. 206. doi: 10.1369/0022155413475452.

Bedford, M. T. and Clarke, S. G. (2009) 'Protein Arginine Methylation in Mammals: Who, What, and Why', *Molecular Cell*, 33(1), p. 1. doi: 10.1016/J.MOLCEL.2008.12.013.

Belisario, D. C. *et al.* (2020) 'Hypoxia Dictates Metabolic Rewiring of Tumors: Implications for Chemoresistance', *Cells 2020, Vol. 9, Page 2598*, 9(12), p. 2598. doi: 10.3390/CELLS9122598.

Bell, D. *et al.* (2011) 'Integrated genomic analyses of ovarian carcinoma', *Nature 2011 474:7353*, 474(7353), pp. 609–615. doi: 10.1038/nature10166.

Biswas, S. and Rao, C. M. (2018) 'Epigenetic tools (The Writers, The Readers and The Erasers) and their implications in cancer therapy', *European Journal of Pharmacology*, 837, pp. 8–24. doi: 10.1016/j.ejphar.2018.08.021.

Blanc, R. S. and Richard, S. (2017) 'Arginine Methylation: The Coming of Age', *Molecular Cell*, 65(1), pp. 8–24. doi: 10.1016/J.MOLCEL.2016.11.003/ASSET/3ABE801A-7BFD-415E-ABF4-6D52A8458520/MAIN.ASSETS/GR5.JPG.

Bokil, A. and Sancho, P. (2019a) 'Mitochondrial determinants of chemoresistance', *Cancer drug resistance (Alhambra, Calif.)*, 2(3), pp. 634–646. doi: 10.20517/CDR.2019.46.

Bokil, A. and Sancho, P. (2019b) 'Mitochondrial determinants of chemoresistance', *Cancer Drug Resistance*, 2(3), p. 634. doi: 10.20517/CDR.2019.46.

Bremang, M. *et al.* (2013) 'Mass spectrometry-based identification and characterisation of lysine and arginine methylation in the human proteome', *Molecular bioSystems*, 9(9), pp. 2231–2247. doi: 10.1039/C3MB00009E.

Brobbey, C. *et al.* (2022) 'The Role of Protein Arginine Methyltransferases in DNA Damage Response', *International Journal of Molecular Sciences 2022, Vol. 23, Page 9780*, 23(17), p. 9780. doi: 10.3390/IJMS23179780.

Calvo, S. E., Clauser, K. R. and Mootha, V. K. (2016) 'MitoCarta2.0: An updated inventory of mammalian mitochondrial proteins', *Nucleic Acids Research*, 44(D1), pp. D1251–D1257. doi: 10.1093/NAR/GKV1003.

Cao, M. *et al.* (2025) 'Biomedical effects of protein arginine methyltransferase inhibitors', *The Journal of Biological Chemistry*, 301(3), p. 108201. doi: 10.1016/J.JBC.2025.108201.

Carter, J. *et al.* (2023) 'PRMT5 Inhibitors Regulate DNA Damage Repair Pathways in Cancer Cells and Improve Response to PARP Inhibition and Chemotherapies', *Cancer Research Communications*, 3(11), pp. 2233–2243. doi: 10.1158/2767-9764.CRC-23-0070,.

Casero, R. A., Murray Stewart, T. and Pegg, A. E. (2018) 'Polyamine metabolism and cancer: treatments, challenges and opportunities', *Nature Reviews Cancer*, 18(11), pp. 681–695. doi: 10.1038/S41568-018-0050-3;SUBJMETA.

Catanzaro, D. *et al.* (2015) 'Inhibition of glucose-6-phosphate dehydrogenase sensitizes cisplatin-resistant cells to death', *Oncotarget*, 6(30), pp. 30102–30114. doi: 10.18632/ONCOTARGET.4945.

Chandrasekaran, V. *et al.* (2021) 'Visualizing formation of the active site in the mitochondrial ribosome', *eLife*, 10, p. e68806. doi: 10.7554/ELIFE.68806.

Chang, B. *et al.* (2007) 'JMJD6 is a histone arginine demethylase', *Science*, 318(5849), pp. 444–447. doi: 10.1126/SCIENCE.1145801,.

Chen, W. *et al.* (2019) 'Decreased expression of mitochondrial miR-5787 contributes to chemoresistance by reprogramming glucose metabolism and inhibiting MT-CO3 translation', *Theranostics*, 9(20), pp. 5739–5754. doi: 10.7150/THNO.37556.

Chen, W. W. *et al.* (2016) 'Absolute quantification of matrix metabolites reveals the dynamics of mitochondrial metabolism', *Cell*, 166(5), p. 1324. doi: 10.1016/J.CELL.2016.07.040.

Chen, X., Chen, S. and Yu, D. (2020) 'Metabolic Reprogramming of Chemoresistant Cancer Cells and the Potential Significance of Metabolic Regulation in the Reversal of Cancer Chemoresistance', *Metabolites*, 10(7), pp. 1–15. doi: 10.3390/METABO10070289.

Choi, Y. M. *et al.* (2015) 'Mechanism of Cisplatin-Induced Cytotoxicity Is Correlated to Impaired Metabolism Due to Mitochondrial ROS Generation', *PLOS ONE*, 10(8), p. e0135083. doi: 10.1371/JOURNAL.PONE.0135083.

Chong, J. and Xia, J. (2018) 'MetaboAnalystR: an R package for flexible and reproducible analysis of metabolomics data', *Bioinformatics*, 34(24), pp. 4313–4314. doi: 10.1093/BIOINFORMATICS/BTY528.

Clayton, D. A. and Shadel, G. S. (2014) 'Isolation of mitochondria from tissue culture cells', *Cold Spring Harbor protocols*, 2014(10), pp. 1109–1111. doi: 10.1101/PDB.PROT080002.

Cocetta, V., Ragazzi, E. and Montopoli, M. (2019) 'Mitochondrial Involvement in Cisplatin Resistance', *International Journal of Molecular Sciences*, 20(14), p. 3384. doi: 10.3390/IJMS20143384.

Dai, W. *et al.* (2022) 'Protein Arginine Methylation: An Emerging Modification in Cancer Immunity and Immunotherapy', *Frontiers in Immunology*, 13, p. 865964. doi: 10.3389/FIMMU.2022.865964/XML.

Dai, Y. *et al.* (2016) 'The involvement of Bcl-2 family proteins in AKT-regulated cell survival in cisplatin resistant epithelial ovarian cancer', *Oncotarget*, 8(1), pp. 1354–1368. doi: 10.18632/ONCOTARGET.13817.

Dar, S. *et al.* (2017) 'Bioenergetic Adaptations in Chemoresistant Ovarian Cancer Cells', *Scientific Reports 2017 7:1*, 7(1), pp. 1–17. doi: 10.1038/s41598-017-09206-0.

Demichev, V. *et al.* (2020) 'DIA-NN: neural networks and interference correction enable deep proteome coverage in high throughput', *Nature Methods*, 17(1), pp. 41–44. doi: 10.1038/S41592-019-0638-X;SUBJMETA.

Desbats, M. A. *et al.* (2020) 'Metabolic Plasticity in Chemotherapy Resistance', *Frontiers in Oncology*, 10, p. 281. doi: 10.3389/FONC.2020.00281/BIBTEX.

Ding, N. *et al.* (2017) 'MTAP deficiency is associated with an unfavourable prognosis and platinum resistance in ovarian cancer'.

Dong, Y. and Zhang, X. (2024) 'Targeting cellular mitophagy as a strategy for human cancers', *Frontiers in Cell and Developmental Biology*, 12, p. 1431968. doi: 10.3389/FCELL.2024.1431968/BIBTEX.

Duong, V. A. and Lee, H. (2023) 'Bottom-Up Proteomics: Advancements in Sample Preparation', *International Journal of Molecular Sciences*, 24(6). doi: 10.3390/IJMS24065350,.

Eram, M. S. *et al.* (2015) 'A Potent, Selective and Cell-active Inhibitor of Human Type I Protein Arginine Methyltransferases', *ACS chemical biology*, 11(3), p. 772. doi: 10.1021/ACSCHEMBIO.5B00839.

Falkenberg, M. *et al.* (2002) 'Mitochondrial transcription factors B1 and B2 activate transcription of human mtDNA', *Nature Genetics*, 31(3), pp. 289–294. doi: 10.1038/NG909;KWRD.

Fan, J. *et al.* (2015) 'Metabolic regulation of histone post-translational modifications', *ACS chemical biology*, 10(1), p. 95. doi: 10.1021/CB500846U.

Fang, C. H. *et al.* (2020) 'A novel c-Kit/phospho-prohibitin axis enhances ovarian cancer stemness and chemoresistance via Notch3 - PBX1 and β-catenin - ABCG2 signaling', *Journal of Biomedical Science*, 27(1), pp. 1–18. doi: 10.1186/S12929-020-00638-X/FIGURES/8.

Farrand, L. *et al.* (2013) 'Piceatannol Enhances Cisplatin Sensitivity in Ovarian Cancer via Modulation of p53, X-linked Inhibitor of Apoptosis Protein (XIAP), and Mitochondrial Fission', *Journal of Biological Chemistry*, 288(33), pp. 23740–23750. doi: 10.1074/JBC.M113.487686.

Fedoriw, A. *et al.* (2022) 'Inhibiting Type I Arginine Methyltransferase Activity Promotes T Cell-Mediated Antitumor Immune Responses', *Cancer Immunology Research*, 10(4), pp. 420–436. doi: 10.1158/2326-6066.CIR-21-0614,.

Feng, Q. *et al.* (2020) 'Targeting G6PD reverses paclitaxel resistance in ovarian cancer by suppressing GSTP1', *Biochemical Pharmacology*, 178, p. 114092. doi: 10.1016/J.BCP.2020.114092.

Fiscutean, A. (2021) 'Clarifying the burden of ovarian cancer', *Nature*, 600(7889), pp. S48–S49. doi: 10.1038/D41586-021-03719-5;SUBJMETA.

Fong, J. Y. *et al.* (2019) 'Therapeutic Targeting of RNA Splicing Catalysis through Inhibition of Protein Arginine Methylation', *Cancer Cell*, 36(2), pp. 194-209.e9. doi: 10.1016/J.CCELL.2019.07.003.

Galluzzi, L. *et al.* (2011) 'Molecular mechanisms of cisplatin resistance', *Oncogene 2012 31:15*, 31(15), pp. 1869–1883. doi: 10.1038/onc.2011.384.

Ganesan, M. *et al.* (2018) 'Demethylase JMJD6 as a New Regulator of Interferon Signaling: Effects of HCV and Ethanol Metabolism', *CMGH*, 5(2), pp. 101–112. doi: 10.1016/j.jcmgh.2017.10.004.

Godel, M. *et al.* (2021) 'Targeting Mitochondrial Oncometabolites: A New Approach to Overcome Drug Resistance in Cancer', *Pharmaceutics 2021, Vol. 13, Page 762*, 13(5), p. 762. doi: 10.3390/PHARMACEUTICS13050762.

Gong, T. T. *et al.* (2023) 'Proteomic characterization of epithelial ovarian cancer delineates molecular signatures and therapeutic targets in distinct histological subtypes', *Nature Communications 2023 14:1*, 14(1), pp. 1–15. doi: 10.1038/s41467-023-43282-3.

Grzeczka, A. *et al.* (2025) 'Sirtuins and their role in ovarian aging-related fibrosis predisposing to ovarian cancer', *npj Aging*, 11(1), pp. 1–11. doi: 10.1038/S41514-025-00256-7;SUBJMETA.

Guccione, E. and Richard, S. (2019) 'The regulation, functions and clinical relevance of arginine methylation', *Nature Reviews Molecular Cell Biology 2019 20:10*, 20(10), pp. 642–657. doi: 10.1038/s41580-019-0155-x.

Guerra, F., Arbini, A. A. and Moro, L. (2017) 'Mitochondria and cancer chemoresistance', *Biochimica et Biophysica Acta (BBA) - Bioenergetics*, 1858(8), pp. 686–699. doi: 10.1016/J.BBABIO.2017.01.012.

Guijas, C. *et al.* (2018) 'METLIN: A Technology Platform for Identifying Knowns and Unknowns', *Analytical chemistry*, 90(5), pp. 3156–3164. doi: 10.1021/ACS.ANALCHEM.7B04424.

Guo, J. *et al.* (2020) 'Arginine methylation of ribose-5-phosphate isomerase A senses glucose to promote human colorectal cancer cell survival', *Science China. Life sciences*, 63(9). doi: 10.1007/S11427-019-1562-Y.

Hajnajafi, K. and Iqbal, M. A. (2025) 'Mass-spectrometry based metabolomics: an overview of workflows, strategies, data analysis and applications', *Proteome Science*, 23(1), p. 5. doi: 10.1186/S12953-025-00241-8.

Hassa, P. O. *et al.* (2008) 'Protein Arginine Methyltransferase 1 Coactivates NF-κB-Dependent Gene Expression Synergistically with CARM1 and PARP1', *Journal of Molecular Biology*, 377(3), pp. 668–678. doi: 10.1016/J.JMB.2008.01.044.

Hayashi, Y. *et al.* (2019) 'Hypoxia/pseudohypoxia-mediated activation of hypoxia-inducible factor-1α in cancer', *Cancer Science*, 110(5), pp. 1510–1517. doi: 10.1111/CAS.13990.

Hillen, H. S. *et al.* (2017) 'Structural Basis of Mitochondrial Transcription Initiation In Brief A structural view of human mitochondrial transcription initiation gives new insights into its unique mechanism and regulation', *Cell*, 171. doi: 10.1016/j.cell.2017.10.036.

Hsu, M. C. *et al.* (2019) 'Protein arginine methyltransferase 3-induced metabolic reprogramming is a vulnerable target of pancreatic cancer', *Journal of Hematology & Oncology*, 12(1), p. 79. doi: 10.1186/S13045-019-0769-7.

Hsu, S. H. and Hung, W. C. (2023) 'Protein arginine methyltransferase 3: A crucial regulator in metabolic reprogramming and gene expression in cancers', *Cancer Letters*, 554, p. 216008. doi: 10.1016/J.CANLET.2022.216008.

Hsu, W. J. *et al.* (2024) 'Arginine Methylation of DDX3 by PRMT1 Mediates Mitochondrial Homeostasis to Promote Breast Cancer Metastasis', *Cancer Research*, 84(18), pp. 3023–3043. doi: 10.1158/0008-5472.CAN-23-3829/746653/AM/ARGININE-METHYLATION-OF-DDX3-BY-PRMT1-MEDIATES.

Hu, Y. *et al.* (2021) 'Arginine methyltransferase PRMT3 promote tumorigenesis through regulating c-MYC stabilization in colorectal cancer', *Gene*, 791, p. 145718. doi: 10.1016/J.GENE.2021.145718.

Huang, B., Lang, X. and Li, X. (2022) 'The role of IL-6/JAK2/STAT3 signaling pathway in cancers', *Frontiers in Oncology*, 12, p. 1023177. doi: 10.3389/FONC.2022.1023177.

Huang, J. *et al.* (2025) 'Mitophagy's impacts on cancer and neurodegenerative diseases: implications for future therapies', *Journal of Hematology & Oncology*, 18(1), p. 78. doi: 10.1186/S13045-025-01727-W.

Hwang, J. W. *et al.* (2021a) 'Protein arginine methyltransferases: promising targets for cancer therapy', *Experimental & Molecular Medicine 2021 53:5*, 53(5), pp. 788–808. doi: 10.1038/s12276-021-00613-y.

Hwang, J. W. *et al.* (2021b) 'Protein arginine methyltransferases: promising targets for cancer therapy', *Experimental and Molecular Medicine*, 53(5), pp. 788–808. doi: 10.1038/S12276-021-00613-Y;SUBJMETA.

Hwang, J. W. *et al.* (2021c) 'Protein arginine methyltransferases: promising targets for cancer therapy', *Experimental & Molecular Medicine 2021 53:5*, 53(5), pp. 788–808. doi: 10.1038/s12276-021-00613-y.

Izar, B. *et al.* (2020) 'A single-cell landscape of high-grade serous ovarian cancer', *Nature Medicine 2020 26:8*, 26(8), pp. 1271–1279. doi: 10.1038/s41591-020-0926-0.

Ji, G. *et al.* (2024) 'Polyamine Anabolism Promotes Chemotherapy-Induced Breast Cancer Stem Cell Enrichment', *Advanced science (Weinheim, Baden-Wurttemberg, Germany)*, 11(40). doi: 10.1002/ADVS.202404853.

Ji, J. X. *et al.* (2024) 'The unique metabolome of clear cell ovarian carcinoma', *The Journal of Pathology*, 264(2), pp. 160–173. doi: 10.1002/PATH.6329.

Jones, J. E. *et al.* (2009) 'Protein arginine deiminase 4 (PAD4): current understanding and future therapeutic potential', *Current opinion in drug discovery & development*, 12(5), p. 616. Available at: https://pmc.ncbi.nlm.nih.gov/articles/PMC3771078/ (Accessed: 5 September 2025).

Kaganovski, A. *et al.* (2025) 'Current and Emerging Therapies for Targeting Protein Arginine Methyltransferases (PRMTs) in Cancer', *International Journal of Molecular Sciences 2025, Vol. 26, Page 7907*, 26(16), p. 7907. doi: 10.3390/IJMS26167907.

Karakashev, S. *et al.* (2018) 'CARM1-expressing ovarian cancer depends on the histone methyltransferase EZH2 activity', *Nature Communications*, 9(1). doi: 10.1038/S41467-018-03031-3,.

Karakashev, S. and Zhang, R. (2020) 'Targeting CARM1 in ovarian cancer with EZH2 and PARP inhibitors', *Molecular & Cellular Oncology*, 7(4). doi: 10.1080/23723556.2020.1760675.

Karnezis, A. N. *et al.* (2016) 'The disparate origins of ovarian cancers: pathogenesis and prevention strategies', *Nature Reviews Cancer 2016 17:1*, 17(1), pp. 65–74. doi: 10.1038/nrc.2016.113.

Kim, E. J. *et al.* (2021) 'BAF155 methylation drives metastasis by hijacking super-enhancers and subverting anti-tumor immunity', *Nucleic Acids Research*, 49(21), pp. 12211–12233. doi: 10.1093/NAR/GKAB1122.

Kingnate, C. *et al.* (2018) 'Possible Roles of Mitochondrial Dynamics and the Effects of Pharmacological Interventions in Chemoresistant Ovarian Cancer', *EBioMedicine*, 34, p. 256. doi: 10.1016/J.EBIOM.2018.07.026.

Kitamura, S. *et al.* (2021) 'PDK2 leads to cisplatin resistance through suppression of mitochondrial function in ovarian clear cell carcinoma', *Cancer Science*, 112(11), pp. 4627–4640. doi: 10.1111/CAS.15125.

Kleih, M. *et al.* (2019) 'Direct impact of cisplatin on mitochondria induces ROS production that dictates cell fate of ovarian cancer cells', *Cell Death & Disease*, 10(11), p. 851. doi: 10.1038/S41419-019-2081-4.

Kleinschmidt, M. A. *et al.* (2008) 'The protein arginine methyltransferases CARM1 and PRMT1 cooperate in gene regulation', *Nucleic Acids Research*, 36(10), p. 3202. doi: 10.1093/NAR/GKN166.

Kleinschmidt, M. A. *et al.* (2012) 'Cell Cycle Regulation by the PRMT6 Arginine Methyltransferase through Repression of Cyclin-Dependent Kinase Inhibitors', *PLoS ONE*, 7(8), p. e41446. doi:

10.1371/JOURNAL.PONE.0041446.

Kong, B. *et al.* (2014) 'P53 is required for cisplatin-induced processing of the mitochondrial fusion protein L-Opa1 that is mediated by the mitochondrial metallopeptidase Oma1 in gynecologic cancers', *Journal of Biological Chemistry*, 289(39), pp. 27134–27145. doi: 10.1074/jbc.M114.594812.

Kong, B. *et al.* (2022) 'Prohibitin 1 interacts with p53 in the regulation of mitochondrial dynamics and chemoresistance in gynecologic cancers', *Journal of Ovarian Research*, 15(1), pp. 1–19. doi: 10.1186/S13048-022-00999-X/FIGURES/8.

Kralj, J. *et al.* (2023) 'Transcriptome analysis of newly established carboplatin-resistant ovarian cancer cell model reveals genes shared by drug resistance and drug-induced EMT', *British Journal of Cancer*, 128(7), pp. 1344–1359. doi: 10.1038/S41416-023-02140-1;SUBJMETA.

Larsen, S. C. *et al.* (2016) 'Proteome-wide analysis of arginine monomethylation reveals widespread occurrence in human cells', *Science Signaling*, 9(443). doi: 10.1126/SCISIGNAL.AAF7329/SUPPL_FILE/9_RS9_TABLES_S1_TO_S5.ZIP.

Laukka, T. *et al.* (2016) 'Fumarate and Succinate Regulate Expression of Hypoxia-inducible Genes via TET Enzymes', *The Journal of biological chemistry*, 291(8), pp. 4256–4265. doi: 10.1074/JBC.M115.688762.

Lavdovskaia, E. *et al.* (2020) 'Dual function of GTPBP6 in biogenesis and recycling of human mitochondrial ribosomes', *Nucleic acids research*, 48(22), pp. 12929–12942. doi: 10.1093/NAR/GKAA1132.

Lei, Y. *et al.* (2022) 'Protein arginine methyltransferase 3 promotes glycolysis and hepatocellular carcinoma growth by enhancing arginine methylation of lactate dehydrogenase A', *Clinical and translational medicine*, 12(1). doi: 10.1002/CTM2.686.

Li, X. *et al.* (2024) 'Dysregulation of arginine methylation in tumorigenesis', *Frontiers in Molecular Biosciences*, 11, p. 1420365. doi: 10.3389/FMOLB.2024.1420365/BIBTEX.

Li, Y. *et al.* (2023) 'PRMT blockade induces defective DNA replication stress response and synergizes with PARP inhibition', *Cell Reports Medicine*, 4(12), p. 101326. doi: 10.1016/J.XCRM.2023.101326/ATTACHMENT/2AEA1AA7-175E-4915-B386-FE6D77A8C872/MMC5.PDF.

Liao, Y. *et al.* (2022) 'PRMT3 drives glioblastoma progression by enhancing HIF1A and glycolytic metabolism', *Cell death & disease*, 13(11). doi: 10.1038/S41419-022-05389-1.

Lin, L. *et al.* (2024) 'CARM1-mediated OGT arginine methylation promotes non-small cell lung cancer glycolysis by stabilizing OGT', *Cell Death and Disease*, 15(12), pp. 1–12. doi: 10.1038/S41419-024-07313-1;TECHMETA.

Liu, F. *et al.* (2017) 'PKM2 methylation by CARM1 activates aerobic glycolysis to promote tumorigenesis', *Nature cell biology*, 19(11), p. 1358. doi: 10.1038/NCB3630.

Liu, Y. *et al.* (2023) 'Methylation of BRD4 by PRMT1 regulates BRD4 phosphorylation and promotes ovarian cancer invasion', *Cell Death & Disease*, 14(9), p. 624. doi: 10.1038/S41419-023-06149-5.

Lothrop, A. P., Torres, M. P. and Fuchs, S. M. (2013) 'Deciphering Post-translational Modification Codes', *FEBS letters*, 587(8), p. 1247. doi: 10.1016/J.FEBSLET.2013.01.047.

Lu, W., Bennett, B. D. and Rabinowitz, J. D. (2008) 'Analytical strategies for LC-MS-based targeted metabolomics', *Journal of chromatography. B, Analytical technologies in the biomedical and life sciences*, 871(2), p. 236. doi: 10.1016/J.JCHROMB.2008.04.031.

Maiti, P. *et al.* (2021) 'Role of GTPases in driving mitoribosome assembly', *Trends in cell biology*,

31(4), p. 284. doi: 10.1016/J.TCB.2020.12.008.

Małecki, J. M., Davydova, E. and Falnes, P. (2022) 'Protein methylation in mitochondria', *The Journal of biological chemistry*, 298(4). doi: 10.1016/J.JBC.2022.101791.

Maniaci, M. *et al.* (2021) 'Systematic Analysis of the Impact of R-Methylation on RBPs-RNA Interactions: A Proteomic Approach', *Frontiers in Molecular Biosciences*, 8, p. 818. doi: 10.3389/FMOLB.2021.688973/BIBTEX.

Maniaci, M. *et al.* (2022) 'A Mass Spectrometry-Based Proteomics Approach for Global and High-Confidence Protein R-Methylation Analysis', *Journal of visualized experiments : JoVE*, 2022(182). doi: 10.3791/62409.

Mansoor, M. *et al.* (2023) 'Comparison of the Efficacy of Cisplatin/Paclitaxel Versus Carboplatin/Paclitaxel in Improving Survival and Quality of Life in the Advanced Ovarian Cancer Patient Population: A Systematic Review and Meta-Analysis of Randomized Control Trials', *Cureus*, 15(12). doi: 10.7759/CUREUS.51011.

Marrache, S., Pathak, R. K. and Dhar, S. (2014) 'Detouring of cisplatin to access mitochondrial genome for overcoming resistance', *Proceedings of the National Academy of Sciences of the United States of America*, 111(29), pp. 10444–10449. doi: 10.1073/PNAS.1405244111/SUPPL_FILE/PNAS.1405244111.SAPP.PDF.

Marsh, D. J., Shah, J. S. and Cole, A. J. (2014) 'Histones and Their Modifications in Ovarian Cancer – Drivers of Disease and Therapeutic Targets', *Frontiers in Oncology*, 4, p. 144. doi: 10.3389/FONC.2014.00144.

Massignani, E. *et al.* (2019) 'hmSEEKER: Identification of hmSILAC Doublets in MaxQuant Output Data', *Proteomics*, 19(5). doi: 10.1002/PMIC.201800300.

Massignani, E. *et al.* (2022) 'ProMetheusDB: An In-Depth Analysis of the High-Quality Human Methyl-proteome', *Molecular & cellular proteomics : MCP*, 21(7). doi: 10.1016/J.MCPRO.2022.100243.

Massignani, E., Maniaci, M. and Bonaldi, T. (2023) 'Heavy Methyl SILAC Metabolic Labeling of Human Cell Lines for High-Confidence Identification of R/K-Methylated Peptides by High-Resolution Mass Spectrometry', *Methods in Molecular Biology*, 2603, pp. 173–186. doi: 10.1007/978-1-0716-2863-8_14.

MATSUBARA, H. *et al.* (2021) 'PRMT1 expression predicts sensitivity to platinum-based chemotherapy in patients with ovarian serous carcinoma', *Oncology Letters*, 21(2), pp. 1–1. doi: 10.3892/OL.2020.12423/HTML.

Matulonis, U. A. *et al.* (2016) 'Ovarian cancer', *Nature Reviews Disease Primers 2016 2:1*, 2(1), pp. 1–22. doi: 10.1038/nrdp.2016.61.

Mauro, C. *et al.* (2011) 'NF-κB controls energy homeostasis and metabolic adaptation by upregulating mitochondrial respiration', *Nature cell biology*, 13(10), pp. 1272–1279. doi: 10.1038/NCB2324.

Mei, H. *et al.* (2015) 'Reduced mtDNA copy number increases the sensitivity of tumor cells to chemotherapeutic drugs', *Cell Death & Disease 2015 6:4*, 6(4), pp. e1710–e1710. doi: 10.1038/cddis.2015.78.

Méndez-García, A. *et al.* (2025) 'Mitochondrial microRNAs (mitomiRs) as emerging biomarkers and therapeutic targets for chronic human diseases', *Frontiers in Genetics*, 16, p. 1555563. doi: 10.3389/FGENE.2025.1555563/XML.

Meng, Y. *et al.* (2022) 'Targeting CRL4 suppresses chemoresistant ovarian cancer growth by

inducing mitophagy', *Signal Transduction and Targeted Therapy*, 7(1), pp. 1–16. doi: 10.1038/S41392-022-01253-Y;SUBJMETA=1059,1517,4028,631,67,692,80;KWRD=CANCER+THERAPY,CELL+BIOLOGY,GYNAECOLOGICAL+CANCER.

MitoCarta3.0: An Inventory of Mammalian Mitochondrial Proteins and Pathways | Broad Institute (no date). Available at: https://www.broadinstitute.org/mitocarta/mitocarta30-inventory-mammalian-mitochondrial-proteins-and-pathways (Accessed: 2 September 2025).

Mu¨, M. M. (2017) 'Post-Translational Modifications of Protein Backbones: Unique Functions, Mechanisms, and Challenges'. doi: 10.1021/acs.biochem.7b00861.

Musiani, D. *et al.* (2019) 'Proteomics profiling of arginine methylation defines PRMT5 substrate specificity', *Science signaling*, 12(575), p. 8388. doi: 10.1126/SCISIGNAL.AAT8388.

Musiani, D. *et al.* (2020) 'PRMT1 Is Recruited via DNA-PK to Chromatin Where It Sustains the Senescence-Associated Secretory Phenotype in Response to Cisplatin', *Cell Reports*, 30(4), pp. 1208-1222.e9. doi: 10.1016/J.CELREP.2019.12.061/ATTACHMENT/17FA0EA5-8E2C-4786-AFA1-3008203E27DB/MMC5.XLSX.

Natanzon, Y., Goode, E. L. and Cunningham, J. M. (2017) 'Epigenetics in ovarian cancer', *Seminars in cancer biology*, 51, p. 160. doi: 10.1016/J.SEMCANCER.2017.08.003.

Nunes, S. C. and Serpa, J. (2018) 'Glutathione in Ovarian Cancer: A Double-Edged Sword', *International Journal of Molecular Sciences*, 19(7), p. 1882. doi: 10.3390/IJMS19071882.

Ong, S. E., Mittler, G. and Mann, M. (2004) 'Identifying and quantifying in vivo methylation sites by heavy methyl SILAC', *Nature methods*, 1(2), pp. 119–126. doi: 10.1038/NMETH715.

Ozturk, H. *et al.* (2025) 'High PRMT5 levels, maintained by KEAP1 inhibition, drive chemoresistance in high-grade serous ovarian cancer', *Journal of Clinical Investigation*, 135(6). doi: 10.1172/JCI184283,.

Pan, Y. *et al.* (2017) 'Metabolic Regulation in Mitochondria and Drug Resistance', *Advances in Experimental Medicine and Biology*, 1038, pp. 149–171. doi: 10.1007/978-981-10-6674-0_11.

Pathak, T. *et al.* (2020) 'Dichotomous role of the human mitochondrial na+ /ca2+ /li+ exchanger nclx in colorectal cancer growth and metastasis', *eLife*, 9, pp. 1–41. doi: 10.7554/ELIFE.59686.

Patti, G. J., Yanes, O. and Siuzdak, G. (2012) 'Innovation: Metabolomics: the apogee of the omics trilogy', *Nature Reviews Molecular Cell Biology*, 13(4), pp. 263–269. doi: 10.1038/NRM3314;SUBJMETA.

Penta, J. S. *et al.* (2001) 'Mitochondrial DNA in human malignancy', *Mutation Research/Reviews in Mutation Research*, 488(2), pp. 119–133. doi: 10.1016/S1383-5742(01)00053-9.

Pluskal, T. *et al.* (2010) 'MZmine 2: Modular framework for processing, visualizing, and analyzing mass spectrometry-based molecular profile data', *BMC Bioinformatics*, 11(1), pp. 1–11. doi: 10.1186/1471-2105-11-395/TABLES/3.

Porporato, P. E. *et al.* (2017) 'Mitochondrial metabolism and cancer', *Cell Research 2017 28:3*, 28(3), pp. 265–280. doi: 10.1038/cr.2017.155.

Poulard, C., Corbo, L. and Le Romancer, M. (2016) 'Protein arginine methylation/demethylation and cancer', *Oncotarget*, 7(41), pp. 67532–67550. doi: 10.18632/ONCOTARGET.11376,.

Qaddoura, S. F. *et al.* (2025) 'Emerging roles of protein arginine methyltransferase in multiple myeloma', *Molecular Therapy Oncology*, 33(2), p. 201003. doi: 10.1016/J.OMTON.2025.201003.

Qian, L. *et al.* (2024) 'Proteomic landscape of epithelial ovarian cancer', *Nature Communications 2024 15:1*, 15(1), pp. 1–20. doi: 10.1038/s41467-024-50786-z.

Qin, J. *et al.* (2017) 'Hypoxia-inducible factor 1 alpha promotes cancer stem cells-like properties in human ovarian cancer cells by upregulating SIRT1 expression', *Scientific reports*, 7(1). doi: 10.1038/S41598-017-09244-8.

Raaphorst, G. P., Li, L. F. and Yang, D. P. (2006) 'Evaluation of Adaptive Responses to Cisplatin in Normal and Mutant Cell Lines with Mutations in Recombination Repair Pathways', *Anticancer Research*, 26(2A), pp. 1183–1187. Available at: https://ar.iiarjournals.org/content/26/2A/1183 (Accessed: 20 September 2025).

Ramachandran, A. *et al.* (2016) 'Human mitochondrial transcription factors TFAM and TFB2M work synergistically in promoter melting during transcription initiation', *Nucleic Acids Research*, 45(2), p. 861. doi: 10.1093/NAR/GKW1157.

Raposo, A. E. and Piller, S. C. (2018) 'Protein arginine methylation: an emerging regulator of the cell cycle', *Cell Division*, 13(1), p. 3. doi: 10.1186/S13008-018-0036-2.

De Rasmo, D. *et al.* (2023) 'Ovarian Cancer: A Landscape of Mitochondria with Emphasis on Mitochondrial Dynamics', *International Journal of Molecular Sciences 2023, Vol. 24, Page 1224*, 24(2), p. 1224. doi: 10.3390/IJMS24021224.

Reintjes, A. *et al.* (2016) 'Asymmetric arginine dimethylation of RelA provides a repressive mark to modulate TNFα/NF-κB response', *Proceedings of the National Academy of Sciences*, 113(16), pp. 4326–4331. doi: 10.1073/PNAS.1522372113.

Ren, F. *et al.* (2025) 'Integration of scRNA-seq and bulk RNA-seq to reveal the association and potential molecular mechanisms of metabolic reprogramming regulated by lactylation and chemotherapy resistance in ovarian cancer', *Frontiers in Immunology*, 16, p. 1513806. doi: 10.3389/FIMMU.2025.1513806/BIBTEX.

Roberts, L. D. *et al.* (2012) 'Targeted Metabolomics', *Current Protocols in Molecular Biology*, CHAPTER(SUPPL.98), p. Unit30.2. doi: 10.1002/0471142727.MB3002S98.

Rojas, V. *et al.* (2016) 'Molecular Characterization of Epithelial Ovarian Cancer: Implications for Diagnosis and Treatment', *International Journal of Molecular Sciences 2016, Vol. 17, Page 2113*, 17(12), p. 2113. doi: 10.3390/IJMS17122113.

Safrhansova, L., Hlozkova, K. and Starkova, J. (2022) 'Targeting amino acid metabolism in cancer', *International Review of Cell and Molecular Biology*, 373, pp. 37–79. doi: 10.1016/BS.IRCMB.2022.08.001.

Sales Amaral, M. V. *et al.* (2019) 'Establishment of Drug-resistant Cell Lines as a Model in Experimental Oncology: A Review', *Anticancer Research*, 39(12), pp. 6443–6455. doi: 10.21873/ANTICANRES.13858.

Schrimpe-Rutledge, A. C. *et al.* (2016) 'Untargeted metabolomics strategies – Challenges and Emerging Directions', *Journal of the American Society for Mass Spectrometry*, 27(12), p. 1897. doi: 10.1007/S13361-016-1469-Y.

Shishkova, E. *et al.* (2017) 'Global mapping of CARM1 substrates defines enzyme specificity and substrate recognition', *Nature communications*, 8. doi: 10.1038/NCOMMS15571.

Shuken, S. R. (2023) 'An Introduction to Mass Spectrometry-Based Proteomics', *Journal of Proteome Research*, 22(7), pp. 2151–2171. doi: 10.1021/ACS.JPROTEOME.2C00838,.

Siddik, Z. H. (2003) 'Cisplatin: Mode of cytotoxic action and molecular basis of resistance', *Oncogene*, 22(47 REV. ISS. 6), pp. 7265–7279. doi: 10.1038/SJ.ONC.1206933;KWRD=MEDICINE.

Signorile, A. *et al.* (2019) 'Human ovarian cancer tissue exhibits increase of mitochondrial biogenesis and cristae remodeling', *Cancers*, 11(9). doi: 10.3390/CANCERS11091350,.

Sonego, M. *et al.* (2017) 'Common biological phenotypes characterize the acquisition of platinum-resistance in epithelial ovarian cancer cells', *Scientific Reports*, 7(1), pp. 1–12. doi: 10.1038/S41598-017-07005-1;TECHMETA.

Spadotto, V. *et al.* (2020) 'PRMT1-mediated methylation of the microprocessor-associated proteins regulates microRNA biogenesis', *Nucleic Acids Research*, 48(1), pp. 96–115. doi: 10.1093/NAR/GKZ1051.

Subbannayya, Y. *et al.* (2021) 'The Role of Omics Approaches to Characterize Molecular Mechanisms of Rare Ovarian Cancers: Recent Advances and Future Perspectives', *Biomedicines*, 9(10), p. 1481. doi: 10.3390/BIOMEDICINES9101481.

Suen, D. F., Norris, K. L. and Youle, R. J. (2008) 'Mitochondrial dynamics and apoptosis', *Genes & Development*, 22(12), p. 1577. doi: 10.1101/GAD.1658508.

Sun, M. *et al.* (2023) 'PRMT6 promotes tumorigenicity and cisplatin response of lung cancer through triggering 6PGD/ENO1 mediated cell metabolism', *Acta pharmaceutica Sinica. B*, 13(1), pp. 157–173. doi: 10.1016/J.APSB.2022.05.019.

Sun, M. *et al.* (2025) 'Utilizing a Negative Enrichment Strategy to Profile Protein Methylation, Leveraging the Orthogonality of LysargiNase and Trypsin', *Molecular & Cellular Proteomics*, 24(7), p. 100970. doi: 10.1016/J.MCPRO.2025.100970.

Sun, X. *et al.* (2019) 'SIRT5 promotes cisplatin resistance in ovarian cancer by suppressing dna damage in a ROS-dependent manner via regulation of the Nrf2/HO-1 pathway', *Frontiers in Oncology*, 9(AUG), p. 470235. doi: 10.3389/FONC.2019.00754/BIBTEX.

Suresh, S., Huard, S. and Dubois, T. (2021) 'CARM1/PRMT4: Making Its Mark beyond Its Function as a Transcriptional Coactivator', *Trends in Cell Biology*, 31(5), pp. 402–417. doi: 10.1016/J.TCB.2020.12.010/ATTACHMENT/56D0AF87-69E3-4FD6-B93E-0842387E22EA/MMC1.DOCX.

Tan, R. *et al.* (2024) 'Integrated proteomics and scRNA-seq analyses of ovarian cancer reveal molecular subtype-associated cell landscapes and immunotherapy targets', *British Journal of Cancer 2024 132:1*, 132(1), pp. 111–125. doi: 10.1038/s41416-024-02894-2.

Tangeda, V. *et al.* (2022) 'Lon upregulation contributes to cisplatin resistance by triggering NCLX-mediated mitochondrial Ca2+ release in cancer cells', *Cell Death & Disease*, 13(3), p. 241. doi: 10.1038/S41419-022-04668-1.

Tautenhahn, R. *et al.* (2012) 'XCMS Online: a web-based platform to process untargeted metabolomic data', *Analytical chemistry*, 84(11), p. 5035. doi: 10.1021/AC300698C.

Tay, A. P. *et al.* (2018) 'MethylQuant: A Tool for Sensitive Validation of Enzyme-Mediated Protein Methylation Sites from Heavy-Methyl SILAC Data', *Journal of Proteome Research*, 17(1), pp. 359–373. doi: 10.1021/ACS.JPROTEOME.7B00601,.

Tewary, S. K., Zheng, Y. G. and Ho, M. C. (2019) 'Protein arginine methyltransferases: insights into the enzyme structure and mechanism at the atomic level', *Cellular and molecular life sciences : CMLS*, 76(15), p. 2917. doi: 10.1007/S00018-019-03145-X.

Thompson, P. R. and Fast, W. (2006) 'Histone citrullination by protein arginine deiminase: is arginine methylation a green light or a roadblock?', *ACS chemical biology*, 1(7), pp. 433–441. doi: 10.1021/CB6002306,.

Veneziani, A. C. *et al.* (2023) 'Heterogeneity and treatment landscape of ovarian carcinoma', *Nature Reviews Clinical Oncology 2023 20:12*, 20(12), pp. 820–842. doi: 10.1038/s41571-023-00819-1.

Vianello, C. *et al.* (2022) 'Cisplatin resistance can be curtailed by blunting Bnip3-mediated

mitochondrial autophagy', *Cell Death & Disease 2022 13:4*, 13(4), pp. 1–14. doi: 10.1038/s41419-022-04741-9.

Virág, D. *et al.* (2020) 'Current Trends in the Analysis of Post-translational Modifications', *Chromatographia*, 83(1), pp. 1–10. doi: 10.1007/S10337-019-03796-9/TABLES/2.

Wai, T. and Langer, T. (2016) 'Mitochondrial Dynamics and Metabolic Regulation', *Trends in Endocrinology and Metabolism*, 27(2), pp. 105–117. doi: 10.1016/j.tem.2015.12.001.

Wang, J. and Wu, G. S. (2014) 'Role of Autophagy in Cisplatin Resistance in Ovarian Cancer Cells', *The Journal of Biological Chemistry*, 289(24), p. 17163. doi: 10.1074/JBC.M114.558288.

Wang, L. *et al.* (2014) 'CARM1 Methylates Chromatin Remodeling Factor BAF155 to Enhance Tumor Progression and Metastasis', *Cancer cell*, 25(1), p. 21. doi: 10.1016/J.CCR.2013.12.007.

Wang, L. *et al.* (2021) 'The Role of Tumour Metabolism in Cisplatin Resistance', *Frontiers in Molecular Biosciences*, 8, p. 691795. doi: 10.3389/FMOLB.2021.691795/FULL.

Wang, M. *et al.* (2016) 'Sharing and community curation of mass spectrometry data with Global Natural Products Social Molecular Networking', *Nature Biotechnology*, 34(8), pp. 828–837. doi: 10.1038/NBT.3597;TECHMETA.

Wang, Y. *et al.* (2020) 'Pharmacological Inhibition of BAD Ser99 Phosphorylation Enhances the Efficacy of Cisplatin in Ovarian Cancer by Inhibition of Cancer Stem Cell-like Behavior', *ACS Pharmacology & Translational Science*, 3(6), p. 1083. doi: 10.1021/ACSPTSCI.0C00064.

Wang, Y. P. *et al.* (2016) 'Arginine Methylation of MDH1 by CARM1 Inhibits Glutamine Metabolism and Suppresses Pancreatic Cancer', *Molecular Cell*, 64(4), pp. 673–687. doi: 10.1016/j.molcel.2016.09.028.

Webb, P. M. and Jordan, S. J. (2024) 'Global epidemiology of epithelial ovarian cancer', *Nature Reviews Clinical Oncology*, 21(5), pp. 389–400. doi: 10.1038/S41571-024-00881-3;SUBJMETA.

Wei, H. H. *et al.* (2021) 'A systematic survey of PRMT interactomes reveals the key roles of arginine methylation in the global control of RNA splicing and translation', *Science Bulletin*, 66(13), pp. 1342–1357. doi: 10.1016/J.SCIB.2021.01.004.

Wise, D. R. *et al.* (2008) 'Myc regulates a transcriptional program that stimulates mitochondrial glutaminolysis and leads to glutamine addiction', *Proceedings of the National Academy of Sciences*, 105(48), pp. 18782–18787. doi: 10.1073/PNAS.0810199105.

Wise, D. R. and Thompson, C. B. (2010) 'Glutamine Addiction: A New Therapeutic Target in Cancer', *Trends in biochemical sciences*, 35(8), p. 427. doi: 10.1016/J.TIBS.2010.05.003.

Wishart, D. S. *et al.* (2022) 'HMDB 5.0: the Human Metabolome Database for 2022', *Nucleic acids research*, 50(D1), pp. D622–D631. doi: 10.1093/NAR/GKAB1062.

Wu, Q. *et al.* (2021) 'Protein arginine methylation: from enigmatic functions to therapeutic targeting', *Nature Reviews Drug Discovery*, 20. doi: 10.1038/s41573-021-00159-8.

Wu, Y. *et al.* (2022) 'Targeting oxidative phosphorylation as an approach for the treatment of ovarian cancer', *Frontiers in Oncology*, 12, p. 971479. doi: 10.3389/FONC.2022.971479/BIBTEX.

Xia, J. and Wishart, D. S. (2016) 'Using MetaboAnalyst 3.0 for Comprehensive Metabolomics Data Analysis', *Current protocols in bioinformatics*, 55, pp. 14.10.1-14.10.91. doi: 10.1002/CPBI.11.

Xia, J., Wishart, D. S. and Valencia, A. (2010) 'MetPA: a web-based metabolomics tool for pathway analysis and visualization', *Bioinformatics (Oxford, England)*, 26(18), pp. 2342–2344. doi: 10.1093/BIOINFORMATICS/BTQ418.

Xia, Q. *et al.* (2025) 'PRMT5-mediated methylation of METTL3 promotes cisplatin resistance in

ovarian cancer by facilitating DNA repair mechanisms', *Cell Reports*, 44(4). doi: 10.1016/j.celrep.2025.115484.

Xie, F. *et al.* (2023) 'PRMT5 promotes ovarian cancer growth through enhancing Warburg effect by methylating ENO1', *MedComm*, 4(2). doi: 10.1002/MCO2.245,.

Xie, L. *et al.* (2021) 'Mitochondria-Shaping Proteins and Chemotherapy', *Frontiers in Oncology*, 11, p. 769036. doi: 10.3389/FONC.2021.769036/XML.

Xu, J. *et al.* (2022) 'Single-Cell RNA Sequencing Reveals the Tissue Architecture in Human High-Grade Serous Ovarian Cancer', *Clinical Cancer Research*, 28(16), pp. 3590–3602. doi: 10.1158/1078-0432.CCR-22-0296/704811/AM/SINGLE-CELL-RNA-SEQUENCING-REVEALS-THE-TISSUE.

Yamamoto, T. *et al.* (2014) 'Reduced methylation of PFKFB3 in cancer cells shunts glucose towards the pentose phosphate pathway', *Nature Communications*, 5(1), pp. 1–16. doi: 10.1038/NCOMMS4480;TECHMETA.

Yan, X. *et al.* (2025) 'Mitophagy in the mechanisms of treatment resistance in solid tumors', *Oncology Reviews*, 19, p. 1607983. doi: 10.3389/OR.2025.1607983.

Yang, Y. *et al.* (2024) 'Autophagy-driven regulation of cisplatin response in human cancers: Exploring molecular and cell death dynamics', *Cancer Letters*, 587, p. 216659. doi: 10.1016/J.CANLET.2024.216659.

Yang, Y. and Bedford, M. T. (2012) 'Protein arginine methyltransferases and cancer', *Nature Reviews Cancer 2012 13:1*, 13(1), pp. 37–50. doi: 10.1038/nrc3409.

Yates, J. R. (1998) 'Mass spectrometry and the age of the proteome', *Journal of Mass Spectrometry*, 33(1), pp. 1–19. doi: 10.1002/(SICI)1096-9888(199801)33:1<1::AID-JMS624>3.0.CO;2-9.

Yi, D. *et al.* (2025) 'The lactylation modification of proteins plays a critical role in tumor progression', *Frontiers in Oncology*, 15, p. 1530567. doi: 10.3389/FONC.2025.1530567.

Yuan, J. *et al.* (2020) 'Bcl-2 family: Novel insight into individualized therapy for ovarian cancer (Review)', *International Journal of Molecular Medicine*, 46(4), p. 1255. doi: 10.3892/IJMM.2020.4689.

Zecha, J. *et al.* (2022) 'Linking post-translational modifications and protein turnover by site-resolved protein turnover profiling', *Nature Communications 2022 13:1*, 13(1), pp. 1–14. doi: 10.1038/s41467-021-27639-0.

Zeki, Ö. C. *et al.* (2020) 'Integration of GC–MS and LC–MS for untargeted metabolomics profiling', *Journal of Pharmaceutical and Biomedical Analysis*, 190. doi: 10.1016/j.jpba.2020.113509.

Zhang, H. *et al.* (2016) 'Integrated Proteogenomic Characterization of Human High-Grade Serous Ovarian Cancer', *Cell*, 166(3), pp. 755–765. doi: 10.1016/J.CELL.2016.05.069.

Zhang, H. *et al.* (2025) 'Revealing the landscape of targeting mitochondrial functions and behaviors to overcome cancer chemoresistance', *Journal of the National Cancer Center*. doi: 10.1016/J.JNCC.2025.02.007.

Zhang, L. *et al.* (2024) 'A Comprehensive LC–MS Metabolomics Assay for Quantitative Analysis of Serum and Plasma', *Metabolites*, 14(11), p. 622. doi: 10.3390/METABO14110622/S1.

Zhang, W. *et al.* (2025) 'Warburg effect and lactylation in cancer: mechanisms for chemoresistance', *Molecular Medicine*, 31(1), pp. 1–24. doi: 10.1186/S10020-025-01205-6/TABLES/5.

Zhang, X. *et al.* (2019) 'Matrine inhibits the development and progression of ovarian cancer by repressing cancer associated phosphorylation signaling pathways', *Cell Death and Disease*, 10(10), pp. 1–17. doi: 10.1038/S41419-019-2013-3;TECHMETA.

Zhang, X. *et al.* (2021) 'PRMT3 promotes tumorigenesis by methylating and stabilizing HIF1α in colorectal cancer', *Cell Death and Disease*, 12(11), pp. 1–13. doi: 10.1038/S41419-021-04352-W;TECHMETA.

Zhong, Q. *et al.* (2023a) 'Protein posttranslational modifications in health and diseases: Functions, regulatory mechanisms, and therapeutic implications', *MedComm*, 4(3), p. e261. doi: 10.1002/MCO2.261.

Zhong, Q. *et al.* (2023b) 'Protein posttranslational modifications in health and diseases: Functions, regulatory mechanisms, and therapeutic implications', *MedComm*, 4(3). doi: 10.1002/MCO2.261.

Zhong, X. Y. *et al.* (2018) 'CARM1 Methylates GAPDH to Regulate Glucose Metabolism and Is Suppressed in Liver Cancer', *Cell Reports*, 24(12), pp. 3207–3223. doi: 10.1016/j.celrep.2018.08.066.

Zhou, L. *et al.* (2024) 'Mina53 demethylates histone H4 arginine 3 asymmetric dimethylation to regulate neural stem/progenitor cell identity', *Nature Communications 2024 15:1*, 15(1), pp. 1–14. doi: 10.1038/s41467-024-54680-6.

Zhou, W. M. *et al.* (2021) 'Methylation Landscape: Targeting Writer or Eraser to Discover Anti-Cancer Drug', *Frontiers in Pharmacology*, 12, p. 690057. doi: 10.3389/FPHAR.2021.690057/EPUB.

8. Acknowledgements

As the four years of this PhD are ending soon, I look back and cordially want to thank everyone who has been a part of this challenging yet incredible journey, directly or indirectly. This work reflects not only my efforts but also the constant support, patience and encouragement from many amazing people along the way.

First of all, I would like to express my heartfelt gratitude to my supervisor, Prof. Tiziana Bonaldi, who gave me the fantastic opportunity to write my own project, work on it with maximum freedom and present it at international platforms that a PhD student can only dream of. Without her constant motivation, feedback and support, I would not have reached the point where I am today. I would like to thank Prof. Nico Mitro, who helped me build my understanding of the fascinating world of metabolism and mitochondria and build the structure of this project. I am grateful to Prof. Rosella Visintin, my internal advisor during these years, who not only taught me how to pose scientific questions and think but also spent considerable time and effort supporting me psychologically in difficult moments. I express my gratitude to my external advisor, Prof. Eyal Gottlieb, for giving me essential direction, feedback and 'food-for-thought' at every thesis committee meeting for at least the next six months.

During this time, I had the privilege of learning from brilliant colleagues at the bench, who not only taught me, listened to me intently and invested their time and energy in optimising new protocols, but also made the work truly enjoyable. I am deeply grateful to Dr Silvia Pedretti for her guidance with metabolomics sample preparation, acquisition, and data analysis—the error bars of my mitostress test are proof that I learnt from the very best. My heartfelt thanks also go to Dr Simona Rodighiero, coordinator of the imaging unit, who trained me on microscopes and data analysis and constantly went the extra mile to support me. From arranging the right Mitotracker dye from Switzerland to staying until 9 pm, capturing videos of mitochondria after a failed experiment just to make me smile, her kindness and dedication left a lasting impact on me. I would also like to thank Simona Ronzoni, coordinator of the flow cytometry unit, who not only trained me on the instruments but also stood by my side to optimise methods, sort cells, and even tracked down articles online to help me improve my experimental designs.

I want to thank my fantastic group; you are really the best. Thanks for keeping on organising aperitivos, dinners, hikes, barbecues, picnics, cracking jokes, board games, cooking nights, mountain retreats, dreaming and planning of opening a bakery or a yoga retreat and most importantly, keeping me light under pressure. These memories will be treasured forever. Especially, I want to thank Michele, my first friend in this country and best friend on campus, for

generating the resistant cell lines, which, today, are the very heart of my project, and for changing my mind every time I wanted to give up. A big shout-out to Alessandro for nurturing the love and curiosity alive in me for science, keeping up with all my last-minute requests and brainstorming about proteomics pipelines. I want to thank Giulia for the transfection trick; I would never figure out the 'bubbling' part on my own. I found passionate scientists in this group, who taught me something every day about science, became friends, and slowly my little family far away from home.

This PhD was a professional journey and indeed the most important lap in my academic career so far, but at the same time, it was a personal journey. I want to thank my best friend, Boris, for his unwavering love, support and faith in me. Although not physically present with me, he was always just a phone call away at any time of the day in any given time zone. Thanks to my best friend Poorva for keeping up with my moods, my phases, my insecurities, my rants and for sticking through thick and thin. I want to thank Adrita and Poulami. They not only shared friendship and sisterhood, but also understood the very personal struggles that academia offers. Thanks to Luca, whom I met at the very end of this journey, but who kept me happy, light, and motivated while I was putting all the pieces together and writing this thesis. Last, but not least, I truly owe this chapter of my life to Maa and Baba for being the strongest pillars of support in my life. Thank you for making me believe in my dreams, not once but twice. Without you, it would not be possible.